MÜHENDİS VE MAKİNA

ENGINEER AND MACHINERY

ISSN 1300-3402 E-ISSN 2667-7520

tmmob makina mühendisleri odası yayın organı

www.mmo.org.tr/muhendismakina

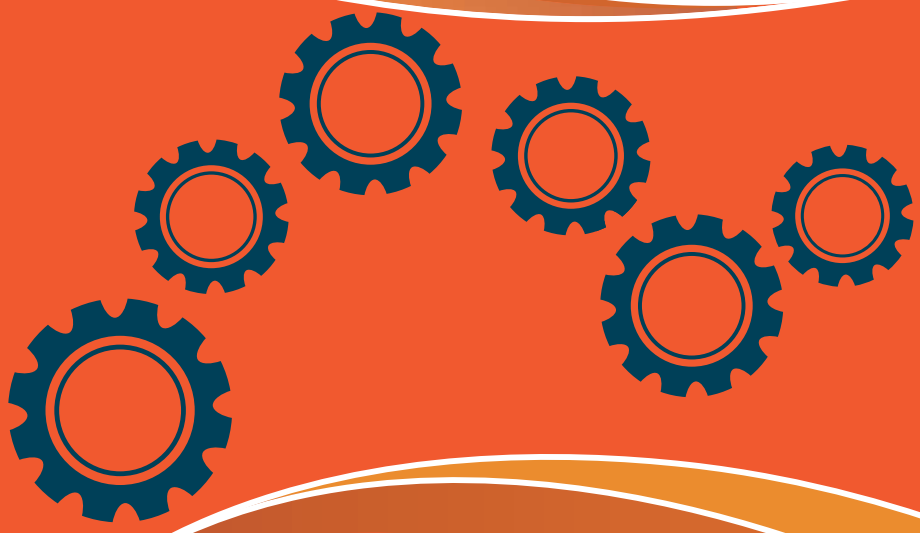

Cilt/Vol 65 Sayı/No 715

Nisan-Haziran/April-June 2024

MMO YAYIN

TMMOB MAKİNA MÜHENDİSLERİ ODASI MÜHENDİS VE MAKİNA DERGİSİ
UCTEA CHAMBER OF MECHANICAL ENGINEERS JOURNAL OF ENGINEER AND MACHINERY
ISSN:1300-3402, E-ISSN:2667-7520

Mühendis ve Makina

Engineer and Machinery

YIL/YEAR : 2024 **CİLT/VOLUME :** 65 **SAYI/ ISSUE :** 715

TMMOB Makina Mühendisleri Odası, Meşrutiyet Cad. 19/6. Kat Kızılay-ANKARA, Tel : (+90 312) 425 21 41
e-posta: yayin@mmo.org.tr https://dergipark.org.tr/tr/pub/muhendismakina https://www.mmo.org.tr/yayin-turu/muhendis-ve-makina-dergisi

TMMOB MAKİNA MÜHENDİSLERİ ODASI MÜHENDİS VE MAKİNA DERGİSİ
UCTEA CHAMBER OF MECHANICAL ENGINEERS JOURNAL OF ENGINEER AND MACHINERY
ISSN:1300-3402, E-ISSN:2667-7520

BASKI/PRINTED BY
Ankamat Matbaacılık Sanayi Ltd. Şti.
30. Cadde 538. Sokak No: 60 İvedik Organize Sanayi- Ankara
Tel: (0312) 394 54 94

BASKI SAYISI / CIRCULATION
1000

BASKI TARİHİ / PUBLISHING DATE
29 Haziran 2024

TMMOB MAKİNA MÜHENDİSLERİ ODASI MÜHENDİS VE MAKİNA DERGİSİ
UCTEA CHAMBER OF MECHANICAL ENGINEERS JOURNAL OF ENGINEER AND MACHINERY
ISSN:1300-3402, E-ISSN:2667-7520

TMMOB MAKİNA MÜHENDİSLERİ ODASI MÜHENDİS VE MAKİNA DERGİSİ
UCTEA CHAMBER OF MECHANICAL ENGINEERS JOURNAL OF ENGINEER AND MACHINERY
ISSN:1300-3402, E-ISSN:2667-7520

*TMMOB Makina Mühendisleri Odası Yayın Organı olan Mühendis ve Makina dergisi TMMOB Makina Mühendisleri Odası üyelerine ücretsiz olarak gönderilir. 1957 yılından beri yayımlanan dergimiz, **hakemli** bir dergidir. Dergimizle ilgili detaylı bilgi almak için www.mmo.org.tr genel ağ adresinden yararlanabilirsiniz. Telefon, faks veya e-posta aracılığıyla da bize ulaşabilirsiniz.*

Dergimizin yer aldığı veritabanları

TMMOB Makina Mühendisleri Odası, Meşrutiyet Cad. 19/6. Kat Kızılay-ANKARA, Tel : (+90 312) 425 21 41
e-posta: yayin@mmo.org.tr https://dergipark.org.tr/tr/pub/muhendismakina https://www.mmo.org.tr/yayin-turu/muhendis-ve-makina-dergisi

TMMOB MAKİNA MÜHENDİSLERİ ODASI MÜHENDİS VE MAKİNA DERGİSİ
UCTEA CHAMBER OF MECHANICAL ENGINEERS JOURNAL OF ENGINEER AND MACHINERY
ISSN:1300-3402, E-ISSN:2667-7520

İÇİNDEKİLER/ CONTENTS

Araştırma Makaleleri / Research Articles

Mühendis ve Makina / Engineer and Machinery
https://dergipark.org.tr/tr/pub/muhendismakina

CRACK GROWTH SIMULATIONS IN ADHESIVELY BONDED JOINTS

Ahmet Can YILDIZ [1*], Tezcan ŞEKERCİOĞLU[2]

[1] Pamukkale Üniversitesi, Mühendislik Fakültesi, Makine Mühendisliği, Denizli,
ORCID No : https://orcid.org/0000-0001-6631-414X

[2] Pamukkale Üniversitesi, Mühendislik Fakültesi, Makine Mühendisliği, Denizli
ORCID No : http://orcid.org/0000-0002-9359-8843

Keywords

Fatigue crack growth, fracture toughness, adaptive meshing

Abstract

Due to the important advantages of adhesive joints, such as their suitability for multi-material designs, their use has been increasing in the last decade. Determining the fracture behavior of structural adhesive bondings is essential for structural durability. In crack propagation analyses, adaptive meshing has drawn considerable attention because of its improvements in terms of complex preprocessing and time management. This paper presents a recently introduced separating morphing and adaptive remeshing technology (SMART) innovative crack growth simulation for adhesively bonded joints, considering static and cyclic cases. For the static case, an R-curve was obtained for the bonding joints of carbon steel and Araldite 2015. For the cyclic case, the Carbon Fiber Reinforced Polymer (CFRP) bonding joints were analyzed under constant-amplitude loading conditions. The crack-propagation rate and the number of cycles were estimated. Crack propagation simulations were validated using experimental data. Acceptable agreement was achieved between the experimental and estimated results.

* acyildiz@pau.edu.tr
doi : 10.46399/muhendismakina.1333309

YAPIŞTIRMA BAĞLANTILARINDA SMART YÖNTEMİ İLE ÇATLAK İLERLEME SİMÜLASYONLARI

Anahtar Kelimeler

Yorulma çatlağı ilerlemesi, kırılma tokluğu, adaptif ağ yöntemi

Öz

Yapıştırma bağlantılarının çoklu malzeme tasarımı uygulamalarında kullanılabilmeleri gibi önemli avantajları nedeniyle son on yılda kullanımları artmıştır. Yapıştırma bağlantılarının yapısal bütünlüğü için kırılma davranışının belirlenmesi elzemdir. Çatlak ilerleme analizlerinde, karmaşık ön işleme ve zaman yönetimi açısından önemli iyileştirmeler sunması nedeniyle adaptif ağ yöntemi ilgi çekmektedir. Bu çalışma, yapıştırma bağlantılarında statik ve yorulma durumlarını dikkate alarak yeni bir çatlak ilerleme simülasyonu yöntemi olan ayırmalı şekillendirme ve adaptif yeniden ağ oluşturma teknolojisini (SMART) tanıtmaktadır. Statik durum için, karbon çeliği ve Araldite 2015'ten oluşan yapıştırma bağlantılarında R-eğrisi elde edilmiştir. Yorulma durumu için, karbon fiber takviyeli polimer (CFRP) yapıştırma bağlantıları sabit genlikli yükleme koşulları altında analiz edilmiştir. Çatlak ilerleme hızı ve çevrim sayısı tahmin edilmiştir. Çatlak ilerleme simülasyonları deneysel veriler kullanılarak doğrulanmıştır. Deneysel ve simülasyon sonuçları arasında kabul edilebilir bir uyum elde edilmiştir.

Araştırma Makalesi			Research Article		
Başvuru Tarihi	:	26.07.2023	Submission Date	:	26.07.2023
Kabul Tarihi	:	08.09.2023	Accepted Date	:	08.09.2023

1. Introduction

Adhesively bonded joints are one of the most promising joining methods compared to conventional methods, such as welding and rivets. Although the evaluation of the behavior of bonded joints according to the classical approach is a well-known field in the literature, assessment using fracture mechanics methods has drawn increasing attention. It has been an important research area over the past decade (Jones and Kinloch, 2015). It has not yet been fully adapted by design engineers in terms of the design and determination of the life of engineering components. Therefore, it can be considered a relatively new field. Adhesive joints are widely preferred in industries such as automotive, aeronautics, and shipbuilding, and their use is increasing regularly (Zuo and Vassilopoulos, 2021). For example, the main reason for its increased use in the automotive industry is the reduction in the weight of automotive components without a significant reduction in mechanical performance. In this regard, steel and multi-material designs of modern materials, such as titanium, aluminum, magnesium, and composites, are widely preferred because multi-material designs provide a significant advantage in terms of weight decrease (Chen, Avery, Su and Kang, 2017). Another important use of composites is in aeronautic and shipbuilding applications (Saleh, Budzik, Saeedifar, Zarouchas and Teixeira De Freitas, 2022). It is not possible to effectively join composites and other modern engineering materials using traditional methods, such as rivets and welding. This is one of the most prominent advantages of the adhesive joints. In addition, it provides important advantages such as relatively favorable load transfer paths, good fatigue strength, and aesthetics, being suitable for the use of thin materials, low-stress distribution, being relatively economical, and easily adaptable to automation (Korta, Młyniec, Zdziebko and Uhl , 2014).

Fatigue failure in engineering applications, that is, failure of components at stress levels lower than the yield strength due to crack propagation under cyclic loading conditions, is the most typical failure mechanism (Quan and Alderliesten, 2022). Therefore, it is very important to determine the fatigue and fracture behaviors of adhesive joints using fracture mechanics methods. Owing to variables such as various geometries, loading rate, loading mode, and joint parameters, the determination of the fracture behavior of the joint requires long experimental practice and is therefore challenging (Jones, 2014). Banea, Da Silva and Campilho (2015) showed that fracture toughness increased as the thickness increased in the 0.2-2 mm adhesive thickness range. However, increasing the adhesive thickness causes a decrease in lap shear strength. For epoxy (Figueiredo, Campilho, Marques, Machado and Da Silva, 2018) and acrylic (Sekiguchi and Sato, 2021) adhesives, it has been reported that increasing the adhesive thickness leads to an increase in fatigue toughness. The effects of various geometries (Costa, Carbas, Marques,

Viana and Da Silva, 2017), different loading types, that is, Mode I, Mode II, and Mixed Mode (Mode I + Mode II), and different R ratios on the static (Monteiro et al., 2020) and fatigue (Rocha et al., 2020) fracture behaviors of the structural adhesives were investigated. Higher stress amplitudes cause faster crack propagation, resulting in a lower life of the components. It was also observed that the fatigue crack propagation rate decreased as crack extension increased (Huang et al., 2013). Linear elastic fracture mechanics (LEFM)-based or J-integral-based, that is, elastic-plastic fracture mechanics (EPFM) techniques, are used to determine the fracture behaviors of adhesive joints. The use of LEFM for fatigue crack growth (FCG) in adhesively bonded joints is a good prediction method, although the underlying physics have not been fully comprehended (Pascoe, Alderliesten and Benedictus, 2017). However, significant deviations may occur in the LEFM estimates depending on the fracture process zone size, and it has been suggested to use the J-integral in such cases (Sarrado, Turon, Costa and Renart, 2016).

The use of the finite element method (FEM) to examine the fracture behavior of cracked components has attracted increasing attention. The Cohesive Zone Method (CZM) is widely used to analyze the fracture behavior of structural adhesives (Campilho, Banea, Pinto, Da Silva and De Jesus, 2011; Rosas, Campilho and Moreira, 2021; Silva, Peres, Campilho, Rocha and Silva, 2023). The model was resolved by defining special interface elements in the region where the crack was located. However, in these models, every crack propagation step requires crack tip re-meshing, that is, a new mesh model needs to be reconstructed, which increases the computational costs and complicates the model (Funari, Lonetti and Spadea, 2019). Therefore, the use of adaptive mesh methods has attracted increasing attention. The newly introduced Ansys's SMART module eliminates the long and complex re-meshing process. As the crack extended, re-meshing was performed automatically around and adjacent to the crack tip (Alshoaibi, 2021). The validity of the SMART procedure has been demonstrated in different types of cracks (Gupta, Sun and Bennett, 2020; Matvienko, Razumovskii and Fedorov, 2021), fatigue crack growth trajectories (Lee and Lu, 2022), and fatigue crack growth in weld transitions (Kowalski and Rozumek, 2019).

Conducting experiments for every boundary condition in engineering applications is considerably time-consuming and costly. Therefore, the finite element method serves as a powerful tool. Modelling of structural adhesives with CZM is very common in the literature. However, analyses of three-dimensional crack propagation with the Cohesive Zone Model (CZM) typically require a rather complex pre-processing stage and have high time/resource demands. Furthermore, it employs damage parameters that are quite challenging to obtain experimentally. On the other hand, the adaptive mesh method can offer faster solutions with a simpler model structure, particularly in complex three-dimensional geo-

metries. This study aims to investigate the static and cyclic behavior of structural adhesives using the SMART procedure, which is an adaptive mesh method. The applicability of the SMART procedure as an alternative to the CZM in adhesive joints has been investigated. A double cantilever beam (DCB) geometry type was modelled, and stable crack and fatigue crack propagation were analyzed by defining different adhesives. In this regard, the static and cyclic behaviors of adhesive joints were examined and compared with experimental data.

2. Crack Growth Simulations

In this study, two different cases were analyzed with the SMART procedure. In the first case, the static state was evaluated under mode I loading conditions. The adhesive joint was modeled using a structural epoxy adhesive and C45E plain carbon steel adherend. The critical energy release rate (G_{Ic}) and total crack propagation were analyzed and compared with experimental results from the literature. In the second case, the cyclic loading conditions were evaluated under mode I loading conditions. The adhesively bonded joint is modeled from the structural epoxy adhesive and carbon fiber reinforced plastic (CFRP) composite. The crack growth rate (da/dN), total crack propagation, and number of cycles were analyzed and compared with experimental data obtained from the literature. Laboratory conditions were based on both case analyses.

2.1 Theoretical Background

Engineering components have macro-or microscale defects that occur during their production and service. The failure behavior of components with crack-like defects is difficult to determine using the classical approach; therefore, a fracture mechanics approach is necessary. The concept of fracture mechanics becomes more complex with the effects of many parameters such as the location and size of the crack, geometry, and loading mode. Therefore, the fracture toughness obtained in the specimen geometries cannot always be exactly transferred to the actual engineering component geometries. The LEFM concept is one of the most widely used fracture mechanics methods for investigating the behavior of adhesively bonded joints. LEFM assumes that elastic effects dominate the stress-strain regions at the crack tip and adjacent regions with very limited plasticity effects. In this study, simulations performed using the SMART procedure were also based on the LEFM. The fracture behavior of an adhesively bonded component is generally characterized by LEFM parameters, such as the stress intensity factor K or energy release rate G. Determining the fracture toughness (K_{Ic} or G_{Ic}) is generally not sufficient for engineering applications because, in real-life applications, components often work under cyclic loading conditions. The relationship between G and K and its solution for the DCB geometry are defined in Equation 1 (Anderson, 2017):

$$G = \frac{\pi\sigma^2 a}{E} = \frac{K_I{}^2}{E'} \quad (1)$$

where E is Young's modulus, E'=E for plane stress conditions, E'=E/(1-ν²) for plane strain conditions, σ is the stress, a is the crack length. The calculation of the stress intensity factor K_I is performed via the interaction integral method defined in Equation 2 and the angle of fatigue crack propagation is determined by Equation 3 (ANSYS, 2020).

$$I = \frac{\int_v q_{ij}\left[\sigma_{kl}\epsilon_{kl}^{aux}\delta_{ij} - \sigma_{kj}^{aux}u_{kj} - \sigma_{kj}^{aux}u_{kj}\right]}{\int_S \delta q_n dS} \quad (2)$$

$$\theta = cos^{-1}\frac{3(K_{II}^{max})^2 + (K_I^{max})\sqrt{(K_I^{max})^2 + 8(K_{II}^{max})^2}}{(K_I^{max})^2 + 9(K_{II}^{max})^2} \quad (3)$$

Where σ_{ij},ε_{ij},u_i are components of stresses,strains and displacements, respectively; $\sigma_{ij}{}^{aux}$,$\varepsilon_{ij}{}^{aux}$,$u_i{}^{aux}$ are components of stresses, strains and displacements of the auxiliary field, respectively; qi are crack extension vector components. The subscripts under K represent mode-I and mode-II fracture. Under cyclic loading conditions, the Paris-Erdogan equation is often used (Paris and Erdogan, 1963). As defined in Equation 4, Paris-Erdogan revealed that crack propagation per unit cycle, that is, the crack growth rate da/dN expression, was related to G. Crack propagation under cyclic loads was defined in three stages. In the first stage, the crack extension begins. The second stage is the stable crack propagation stage, which covers most of the life before the fracture. This stage was also known as the Paris Regime. In the third stage, the crack propagation became unstable, and fracture occurred with a sudden increase in G.

$$\frac{da}{dN} = Cf(G)^n \quad (4)$$

$$f(G) = \Delta G = G_{max} - G_{min} \quad (5)$$

For f (G), one of the definitions specified in Equation 5 is typically used. Where G_{min} is the energy release rate at the minimum load and G_{max} is the maximum load. In this paper, G_{max} was considered to be compatible with the experimental study.

2.2 Materials and Specimen Geometries

For the first case, the structural epoxy adhesive Araldite 2015 and adherend

C45E plane carbon steel were modelled. In the other case, the structural epoxy adhesive Loctite EA 9395-9396 and CFRP (Hexcel 8552) as the adherend were modelled. The mechanical properties of the materials used in the models for the two cases are listed in Table 1. The Paris-Erdogan parameters obtained experimentally (Floros and Tserpes, 2019) under cyclic loading conditions are listed in Table 2. The DCB-type specimens were modelled for both cases. The DCB specimen geometries are presented in Figure 1 for the first case and in Figure 2 for the second case. All dimensions are in millimeters. The geometric dimensions and material properties are based on the manufacturer's data and literature. The adhered CFRP material was modeled as a solid to simplify the crack propagation simulation and reduce resource/time requirements.

Table 1. Mechanical Properties of the Materials Modelled in the Simulations

Case	Material	Young's Modulus (GPa)	Poisson's Ratio	Tensile Yield Strength (MPa)	Tensile Failure Strength (MPa)	Shear Modulus (GPa)	Critical Energy Release Rate (N/mm)
Static (Lopes, Campilho, Da Silva and Faneco, 2016)	Adhesive	1.85	0.33	13	22	0.56	0.43
	Adherend	204	0.3	279	347	78	
Fatigue (Thäsler, Holtmannspötter and Gudladt, 2019)	Adhesive	3.35	0.35	-	56.8	1.5	-
	Adherend	164	0.3	-	2724	63	

Table 2. Paris-Erdogan Parameters Were Used İn The Simulation (Floros and Tserpes, 2019)

Paris-Erdogan Parameters	
C	0.47
n	7.22

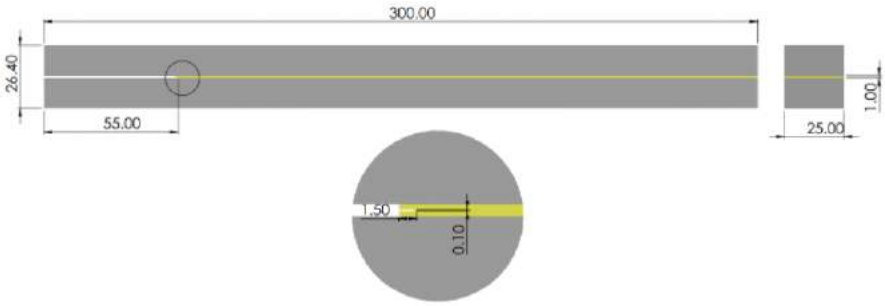

Figure 1. Specimen Geometry For The Static Case, According to (Lopes et al., 2016).

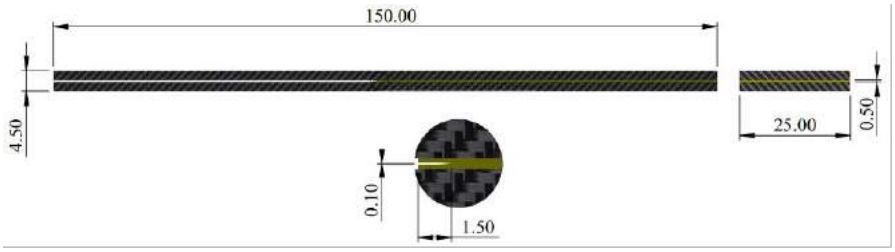

Figure 2. Specimen Geometry for the Cyclic Case, According to (Floros and Tserpes, 2019).

2.3 Crack Growth with SMART Procedure

Although various experimental and numerical methods are extensively used for the evaluation and solution of engineering problems, adaptive mesh and extended finite element methods (XFEM) are drawing more attention as alternative solutions. The experimental and finite element methods were complementary to each other. Finite element applications will gain more importance owing to the cost and time issues of the experimental methods. The SMART procedure, developed and introduced by ANSYS Inc., has introduced many innovations in the field of fracture mechanics. With SMART, crack propagation simulations in 3D geometries can be performed effectively in terms of process time. Since geometry is a parameter that directly affects the fracture behavior of engineering components, it is not always possible to model real and complex geometries of components in 2D, so effective modelling of 3D geometries is essential for engineering applications. In addition, SMART shortens the need for post-processing for designers and researchers by using the unstructured mesh method (UMM) with its tetrahedral mesh elements and significantly minimizes the complex mesh structure and re-meshing time. With SMART, re-meshing is automatically conducted at the crack tip and adjacent to the crack propagation in each subs-

tep time interval. This provides significant flexibility and saves time in terms of complex preprocessing transactions. Figure 3 shows the crack propagation and re-meshing at the crack tip and adjacent under static and cyclic conditions, respectively. Cracks with different shapes (such as semi-elliptical and pre-meshed) can be simulated using SMART technology. However, this method has some significant limitations. In this study, it is assumed based on experimental data that the crack will propagate only through the adhesive. However, this assumption is not always valid in real applications. Moreover, the effects of defects such as local air voids and surface roughness present in adhesive joints were not considered in the conducted simulation.

A pre-meshed crack structure was used for both the analyses. The crack tip and adjacent were improved using the sphere of influence method. For the solution, the contour was determined as 6, and the crack tip, lower, and upper surfaces were defined for the pre-meshed crack, and a separate coordinate system was defined for the crack. The mesh structure created in the DCB specimens for the static case is shown in Fig. 4. The mesh structure is directly related to the precision of the obtained results. The mesh structure of a region/model can be determined by mesh quality criteria, such as aspect ratio, skewness, and orthogonal quality. Since tetrahedral element type was used in the simulation, the skewness mesh quality criterion was preferred. According to the skewness mesh quality criterion, the mesh quality increases as the average skewness value approaches 0 with a minimum of 0 and a maximum of 1. In the models used for both cases, meshing was performed with UMM and tetrahedral SOLID187 elements with an average size of 2 mm. A very fine mesh with an average size of 0.05 mm was applied at the crack tip and adjacent regions. The DCB specimens modelled for the static case had 651357 nodes and 449556 elements. The overall mesh structure has an average value of 0.2 according to the skewness mesh quality criterion. The skewness of a mesh structure indicates how close it is to the ideal shape or form. In general, low orthogonal or high skewness values are not recommended. The SOLID187 element, a 10-node higher-order three-dimensional finite element, is optimally designed for the analysis of solid structures. SOLID187 exhibits quadratic displacement characteristics, making it particularly well-suited for accurately representing irregular mesh geometries. This element is characterized by the presence of ten nodes, each offering three degrees of freedom, enabling translation along the nodal x, y, and z axes.

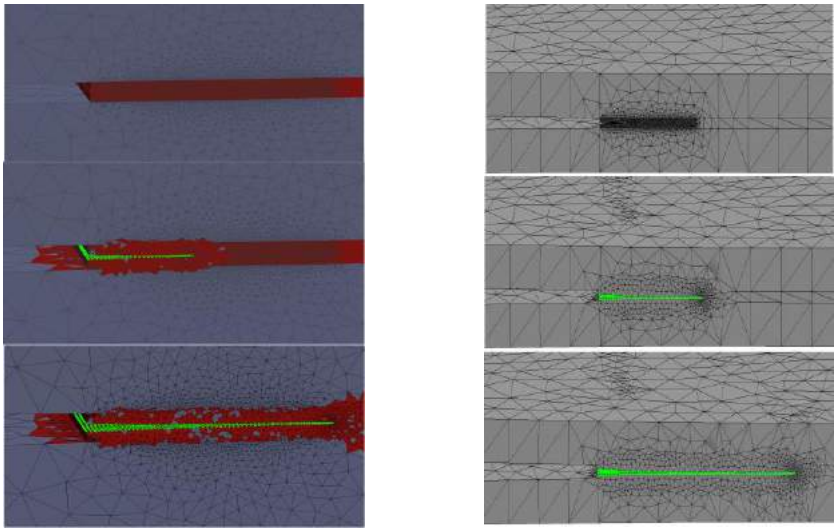

(a) **(b)**

Figure 3. Re-Meshing at the Crack Tip And Adjacent With Crack Propagation, for Static (a) and Cyclic (b) Cases, Respectively

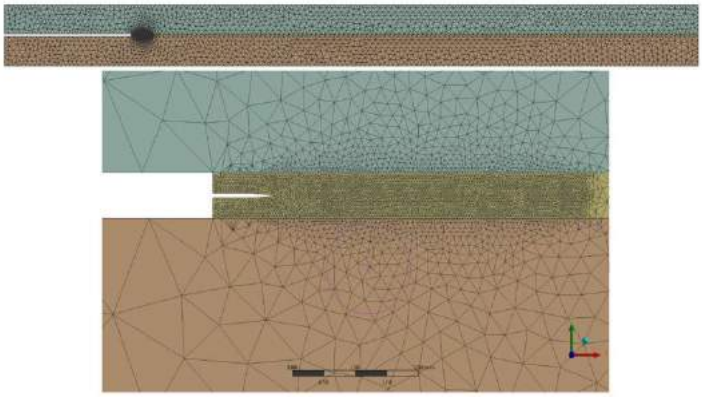

Figure 4. General and Crack Tip Mesh Structures in DCB Specimen for the Static Case

The DCB specimens modelled for the cyclic case had 486266 nodes and 358919 elements. The skewness mesh quality criterion had an average value of 0.28. The overall mesh structure of the DCB specimen in the cyclic case is shown in Figure 5. In the crack propagation simulations performed for both cases, a gradual displacement was applied, and a solution was conducted in 150 sub-steps. A 0.0113 mm/sub-step displacement was applied for the static case, whereas a 0.0073

mm/sub-step displacement was applied for the cyclic case. Crack growth simulations were carried out under a constant amplitude load ratio of R=0.1 for cyclic loading. The boundary conditions of crack growth simulation models prepared for the static and cyclic cases are shown in Fig. 6. In this study, the principles of research and publication ethics have been adhered to.

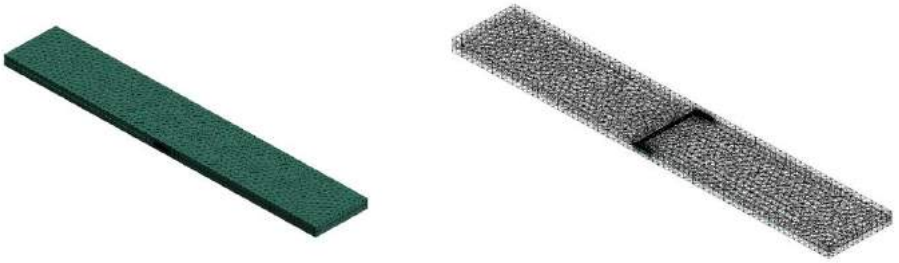

Figure 5. General Mesh Structure İn DCB Specimen For The Cyclic Case

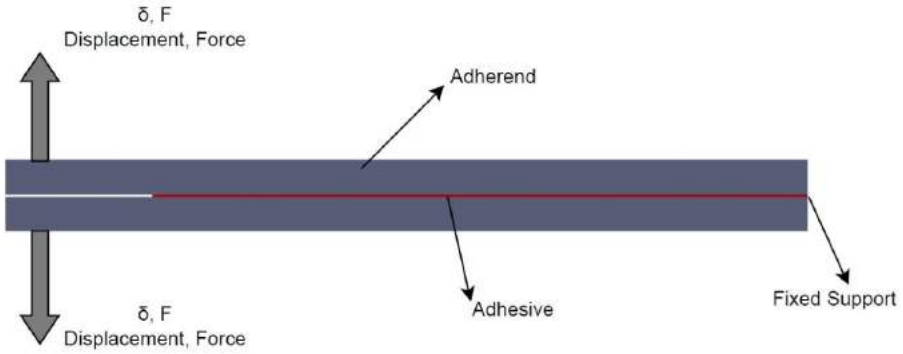

Figure 6. Schematic Representation of Boundary Conditions in Crack Growth Simulation Model

3. Results and Discussions

Two different crack propagation simulations were performed using the SMART procedure for the static and cyclic cases. In the model at mode I loading for the static case, the fracture toughness (G_{Ic}) of Araldite 2015 was defined as 0.43 N/mm. G_{Ic} is the critical level at which the crack propagation begins. A total of 5.45 mm crack propagation occurred in the finite element analysis. The R-curve obtained for the static case is shown in Fig. 7. When compared with the experimental data (Lopes et al., 2016), it was observed that the results obtained from

the analysis converged with the experimental results. After the G_{Ic} level for crack propagation is exceeded, the crack starts to propagate; however, as can be seen from the results, the G level required for crack propagation does not increase linearly. A stable propagation was observed after approximately 5 mm of crack propagation. This is in agreement with the experimental data. When the data obtained from the finite element analysis were compared with the experimental data, the error rate reached a maximum of 20%, while the average was 7%. In finite element analysis, the ideal situation is modelled; however, in experimental practice, deviations may occur owing to adhesive issues, defects, and crack arrest (Campilho, Moura, Banea and Da Silva, 2015). Therefore, the results obtained from the finite element analyses performed using the SMART procedure were within acceptable deviations when compared with the experimental results.

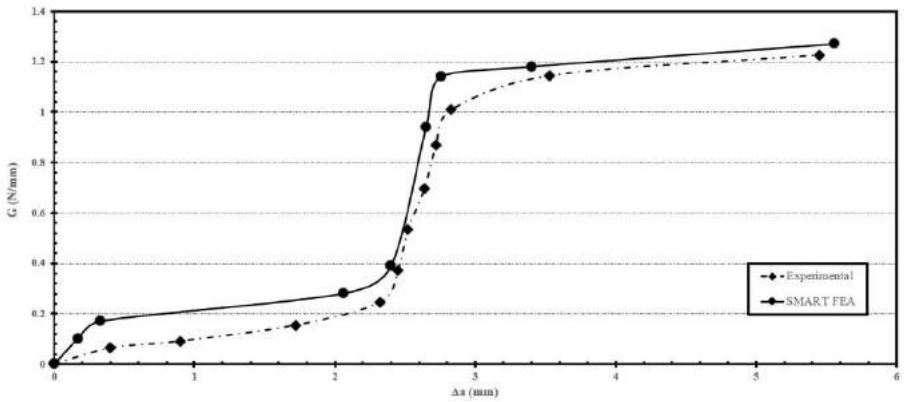

Figure 7. Comparison With the R Curves for the Static Case and the Experiment (Lopes et al., 2016)

A comparison of the crack propagation with the experimental data (Floros and Tserpes, 2019) against the number of cycles obtained from the crack propagation simulation performed for the cyclic case is shown in Figure 8. As the number of cycles increased, the crack propagation decreased. In addition, the crack propagation did not increase linearly. From this analysis, a total crack propagation of approximately 11.7 mm was obtained. The experimental data were separated using finite element analysis at the initial stage of crack propagation. In the finite element analysis, the crack extended much faster than that in the experimental application. This increased the deviation rate. However, when evaluated as a whole, consistent results were obtained in terms of the number of cycles and the total crack propagation parameters.

The fatigue crack growth behavior obtained under constant amplitude R=0.1

mode-I loading conditions is presented in Figure 9 on a log-log scale. Gmin was not considered, and $G_{max}$was used as a basis for compatibility with the experimental results, as previously defined in Equation 3. Large scatterings have occurred in the maximum energy release rate G_{max} curve corresponding to the obtained crack propagation rate da/dN. While the conducted simulation was able to more accurately predict sections with high crack propagation rates, it was unable to achieve sufficient success at low crack propagation rates. There could be many reasons for this. For instance, local air voids in the adhesive could be much more effective at low crack propagation rates. The way the adhesive is applied and the condition of the surface also have a significant impact on the results obtained experimentally. As the crack propagation simulations conducted examined the ideal situation, scatterings can occur in the results obtained. The Paris-Erdogan parameters C and n obtained experimentally have a significant place in the accuracy of the simulation. Wide scatterings in experimental data can affect the accuracy of these parameters.

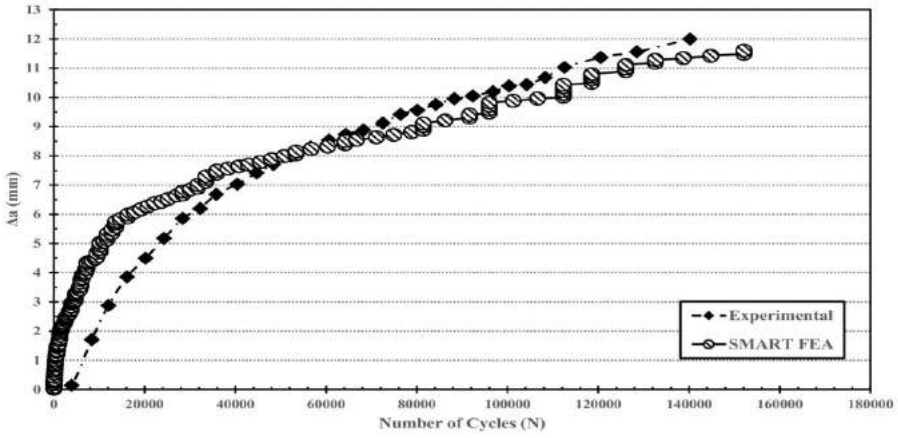

Figure 8. Comparison With Fatigue Crack Propagation and Experimental Data (Floros and Tserpes, 2019) for the Cyclic Case

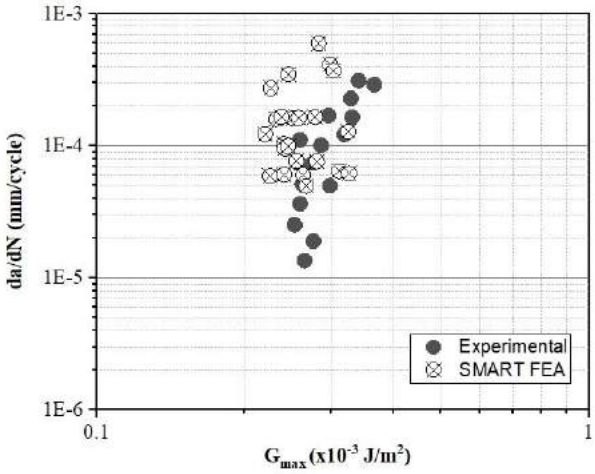

Figure 9. Comparison With Fatigue Crack Growth Rate And Experimental Data (Floros and Tserpes, 2019) for the cyclic case

5. Conclusions

In this study, the SMART procedure, a newly developed adaptive meshing method, was examined. Crack propagation simulations in bonded joints were successfully performed using the SMART procedure and validated using experimental data. Crack propagation occurs in 3D throughout the simulation, and with it, the sensitive crack tip region mesh structure changes and adapts. The finite element method is a powerful tool for determining the effect of complex interactions on the fracture behavior of engineering components. Although experimental methods are the most reliable for determining the fracture behavior of adhesively bonded joints, it is not realistic in terms of cost and time management to experiment for each combination of geometries and joints. Therefore, it became necessary to examine different crack types in complex geometries using 3D finite element simulations. Under mode I loading conditions, valid crack propagation simulations were performed for two different cases: static and cyclic. The R-curve obtained for the static case was compared with the experimental data, and consistent results were obtained. Although the crack propagation for the cyclic case was faster than the experimental data at the beginning, the deviation rate increased; however, the experimental data were generally in agreement with the experimental data. If it remains within the elastic limits, SMART is a highly accurate tool, but its validity should be carefully questioned in situations where plasticity effects are more effective. This is one of the biggest disadvantages of this technology under the current conditions. While the SMART procedure in adhesive joints of-

fers a simple analysis structure and fast analysis solution in three-dimensional complex geometries, we believe that the results obtained need to be carefully examined. Adhesives can exhibit behaviors ranging from brittle to viscoelastic or plastic. We believe that the LEFM approach can also be used within certain error scatters in crack propagation analyses in adhesive joints. However, the character of the plastic zone occurring at the crack tip and the complex stress structure formed in the adhesive can significantly complicate the crack propagation analyses. This situation can limit the accuracy of the LEFM approach. Hence in future studies, investigating different types of adhesives and adherends, and different crack geometries in the application of the SMART procedure to adhesive joints will be decisive for the accuracy of the method.

Nomenclature

a	Crack Length
C	Paris-Erdogan Exponent
CFRP	Carbon Fiber Reinforced Polymer
CZM	Cozehive Zone Method
da/dN	Crack Growth Rate
DCB	Double Cantilever Beam
EPFM	Elastic-Plastic Fracture Mechanics
ε	Strain
FCG	Fatigue Crack Growth
FEM	Finite Element Method
G	Energy Release Rate
G_{Ic}	Critical Energy Release Rate or Fracture Toughness
G_{max}	Energy Release Rate at Maximum Load
G_{min}	Energy Release Rate at Minimum Load
I	Interaction Integral
K	Stress Intensity Factor
$K_{ıc}$	Critical Stress Intensity Factor or Fracture Toughness
LEFM	Linear Elastic Fracture Mechanics
n	Paris-Erdogan Constant
σ	Stress
SMART	Separating Morphing and Adaptive Remeshing Technology
u	Displacement

UMM Unstructured Mesh Method

X-FEM Extended Finite Element Method

θ Angle of Crack Propagation

References

Alshoaibi, A. M. (2021). Computational Simulation of 3D Fatigue Crack Growth under Mixed-Mode Loading. *Applied Sciences, 11*(13), 5953. https://doi.org/10.3390/app11135953

Anderson, T. L. (2017). *Fracture Mechanics* (4. ed.). CRC Press.

ANSYS. Academic Research Mechanical, Release 19.2, Help System. In Coupled Field Analysis Guide, 2020; ANSYS, Inc., USA.

Banea, M. D., Da Silva, L. F. M., & Campilho, R. D. S. G. (2015). The Effect of Adhesive Thickness on the Mechanical Behavior of a Structural Polyurethane Adhesive. *The Journal of Adhesion, 91*(5), 331–346. https://doi.org/10.1080/00218464.2014.903802

Campilho, R. D. S. G., Banea, M. D., Pinto, A. M. G., Da Silva, L. F. M., & De Jesus, A. M. P. (2011). Strength prediction of single- and double-lap joints by standard and extended finite element modelling. *International Journal of Adhesion and Adhesives, 31*(5), 363–372. https://doi.org/10.1016/j.ijadhadh.2010.09.008

Campilho, R. D. S. G., Moura, D. C., Banea, M. D., & Da Silva, L. F. M. (2015). Adhesive thickness effects of a ductile adhesive by optical measurement techniques. *International Journal of Adhesion and Adhesives, 57,* 125–132. https://doi.org/10.1016/j.ijadhadh.2014.12.004

Chen, Q., Guo, H., Avery, K., Su, X., & Kang, H. (2017). Fatigue performance and life estimation of automotive adhesive joints using a fracture mechanics approach. *Engineering Fracture Mechanics, 172,* 73–89. https://doi.org/10.1016/j.engfracmech.2017.01.005

Costa, M., Carbas, R., Marques, E., Viana, G., & Da Silva, L. F. M. (2017). An apparatus for mixed-mode fracture characterization of adhesive joints. *Theoretical and Applied Fracture Mechanics, 91,* 94–102. https://doi.org/10.1016/j.tafmec.2017.04.014

Figueiredo, J. C. P., Campilho, R. D. S. G., Marques, E. A. S., Machado, J. J. M., & Da Silva, L. F. M. (2018). Adhesive thickness influence on the shear fracture toughness measurements of adhesive joints. *International Journal of Adhesion and Adhesives, 83,* 15–23. https://doi.org/10.1016/j.ijadhadh.2018.02.015

Floros, I., & Tserpes, K. (2019). Fatigue crack growth characterization in adhesive CFRP joints. Composite Structures, 207, 531–536. https://doi.org/10.1016/j.compstruct.2018.09.020

Funari, M. F., Lonetti, P., & Spadea, S. (2019). A crack growth strategy based on moving mesh method and fracture mechanics. Theoretical and Applied Fracture Mechanics, 102, 103–115. https://doi.org/10.1016/j.tafmec.2019.03.007

Gupta, A., Sun, W., & Bennett, C. J. (2020). Simulation of fatigue small crack growth in additive manufactured Ti–6Al–4V material. *Continuum Mechanics and Thermocyclics, 32*(6), 1745–1761. https://doi.org/10.1007/s00161-020-00878-0

Hexcel HexPly 8552, Product Data Sheet, EU Version, 2016.

Huang, Y., Bu, Y., Zhou, L., Zhu, J., Shi, H., Xie, H., & Feng, X. (2013). Fatigue crack growth and propagation along the adhesive interface between fiber-reinforced composites. *Engineering Fracture Mechanics, 110,* 290–299. https://doi.org/10.1016/j.engfracmech.2013.08.011

Jones, R. (2014). Fatigue crack growth and damage tolerance. *Fatigue & Fracture of Engineering Materials & Structures, 37*(5), 463–483. https://doi.org/10.1111/ffe.12155

Jones, R., Hu, W., & Kinloch, A. J. (2015). A convenient way to represent fatigue crack growth in structural adhesives. *Fatigue & Fracture of Engineering Materials & Structures, 38*(4), 379–391. https://doi.org/10.1111/ffe.12241

Korta, J., Młyniec, A., Zdziebko, P., & Uhl, T. (2014). Finite Element Analysis Of Adhesive Bonds Using The Cohesive Zone Modeling Method. *Mechanics and Control, 33*(2), 51. https://doi.org/10.7494/mech.2014.33.2.51

Kowalski, M., & Rozumek, D. (2019). *Numerical simulation of fatigue crack growth in steel-aluminium transition joint.* 170020. https://doi.org/10.1063/1.5138099

Lee, Y. F., & Lu, Y. (2022). Advanced numerical simulations considering crack orientation for fatigue damage quantification using nonlinear guided waves. *Ultrasonics, 124,* 106738. https://doi.org/10.1016/j.ultras.2022.106738

LOCTITE EA 9395 AERO Epoxy Paste Adhesive Technical Process Bulletin

LOCTITE EA 9396 AERO Epoxy Paste Adhesive Technical Process Bulletin.

Lopes, R. M., Campilho, R. D. S. G., Da Silva, F. J. G., & Faneco, T. M. S. (2016). Comparative evaluation of the Double-Cantilever Beam and Tapered Double-Cantilever Beam tests for estimation of the tensile fracture toughness of ad-

hesive joints. *International Journal of Adhesion and Adhesives, 67,* 103–111. https://doi.org/10.1016/j.ijadhadh.2015.12.032

Matvienko, Y. G., Razumovskii, I. A., & Fedorov, A. A. (2021). Numerical Modeling the Effect of Static Indentation on the Rate and the Fatigue Crack Growth Trajectory. Journal of Physics: *Conference Series, 1945*(1), 012039. https://doi.org/10.1088/1742-6596/1945/1/012039

Monteiro, J., Akhavan-Safar, A., Carbas, R., Marques, E., Goyal, R., El-zein, M., & Silva, L. F. M. (2020). Influence of mode mixity and loading conditions on the fatigue crack growth behaviour of an epoxy adhesive. *Fatigue & Fracture of Engineering Materials & Structures, 43*(2), 308–316. https://doi.org/10.1111/ffe.13125

Paris, P., & Erdogan, F. (1963). A Critical Analysis of Crack Propagation Laws. *Journal of Basic Engineering, 85*(4), 528–533. https://doi.org/10.1115/1.3656900

Pascoe, J. A., Alderliesten, R. C., & Benedictus, R. (2017). On the physical interpretation of the R-ratio effect and the LEFM parameters used for fatigue crack growth in adhesive bonds. *International Journal of Fatigue, 97,* 162–176. https://doi.org/10.1016/j.ijfatigue.2016.12.033

Quan, H., & Alderliesten, R. C. (2022). The energy dissipation during fatigue crack growth in adhesive joints under Mode-I loading. *Theoretical and Applied Fracture Mechanics, 120,* 103418. https://doi.org/10.1016/j.tafmec.2022.103418

Rocha, A. V. M., Akhavan-Safar, A., Carbas, R., Marques, E. A. S., Goyal, R., El-zein, M., & Silva, L. F. M. (2020). Fatigue crack growth analysis of different adhesive systems: Effects of mode mixity and load level. *Fatigue & Fracture of Engineering Materials & Structures, 43*(2), 330–341. https://doi.org/10.1111/ffe.13145

Rosas, M. F. M. O., Campilho, R. D. S. G., & Moreira, R. D. F. (2021). Numerical analysis of geometrical modification combinations of the tensile strength of tubular adhesive joints. *Procedia Structural Integrity, 33,* 115–125. https://doi.org/10.1016/j.prostr.2021.10.016

Saleh, M. N., Budzik, M. K., Saeedifar, M., Zarouchas, D., & Teixeira De Freitas, S. (2022). On the influence of the adhesive and the adherend ductility on mode I fracture characterization of thick adhesively-bonded joints. *International Journal of Adhesion and Adhesives, 115,* 103123. https://doi.org/10.1016/j.ijadhadh.2022.103123

Sarrado, C., Turon, A., Costa, J., & Renart, J. (2016). On the validity of linear elastic fracture mechanics methods to measure the fracture toughness of adhesive

joints. *International Journal of Solids and Structures, 81,* 110–116. https://doi.org/10.1016/j.ijsolstr.2015.11.016

Sekiguchi, Y., & Sato, C. (2021). Effect of Bond-Line Thickness on Fatigue Crack Growth of Structural Acrylic Adhesive Joints. *Materials, 14*(7), 1723. https://doi.org/10.3390/ma14071723

Silva, A. F. M. V., Peres, L. M. C., Campilho, R. D. S. G., Rocha, R. J. B., & Silva, F. J. G. (2023). Cohesive zone parametric analysis in the tensile impact strength of tubular adhesive joints. Proceedings of the Institution of Mechanical Engineers, Part E: *Journal of Process Mechanical Engineering, 237*(1), 26–37. https://doi.org/10.1177/09544089221088261

Thäsler, T., Holtmannspötter, J., & Gudladt, H. J. (2019). Monitoring the fatigue crack growth behavior of composite joints using in situ 2D-digital image correlation. *Journal of Adhesion, 95*(5–7), 595–613. https://doi.org/10.1080/00218464.2018.1562923

Zuo, P., & Vassilopoulos, A. P. (2021). Review of fatigue of bulk structural adhesives and thick adhesive joints. *International Materials Reviews, 66*(5), 313–338. https://doi.org/10.1080/09506608.2020.1845110

Mühendis ve Makina / Engineer and Machinery
https://dergipark.org.tr/tr/pub/muhendismakina

BULAŞIK MAKİNELERİ İÇİN DOĞAL HAVALANDIRMA YÖNTEMİNİ KULLANAN YENİ BİR KURUTMA SİSTEMİ TASARIMI VE DENEYSEL ANALİZİ

Fatih ENGİNSEL[1*], Halil Kürşad ERSOY[2]

[1] Arçelik A.Ş, Bulaşık Makinesi İşletmesi Ar-Ge Merkezi, Ankara
ORCID No : 0000-0002-2866-9844

[2] Konya Teknik Üniversitesi, Mühendislik ve Doğa Bilimleri Fakültesi, Makine Mühendisliği, Konya
ORCID No : 0000-0001-8588-296X

Anahtar Kelimeler

Bulaşık makinesi, doğal havalandırma, EN 60436, kurutma

Öz

Bulaşık makinelerinde yüklerin yıkanmasına ek olarak kurutulması da temel işlevlerdendir. Kurutma, makine sepetlerinde yer alan yüklerin yüzeyindeki su zerreciklerinin tamamen buharlaştırılması ile gerçekleşir. Bulaşık makinesi yıkama algoritmasında sıcak durulama sonrasında kurutma adımına geçilir. Sıcak durulama aşaması sonrasında kabindeki nem miktarı çok yoğundur. Kurutma adımında kabinde herhangi bir su ısıtılması olmamasına rağmen sepetteki yüklerin buharlaşması nedeniyle nem yoğunluğu artmaya devam etmektedir. Yükler üzerindeki buharlaşmanın, yani kurutmanın devam etmesi için kabin nem miktarının azaltılması gereklidir. Bunun sağlanması için geliştirilen kurutma sistemleri temelde buharlaşan su damlacıklarının daha soğuk bir yüzeyde yoğuşturulması ya da makineden uzaklaştırılması mekanizmalarını gerçekleştirir. Bu çalışmada doğal havalandırma yöntemini kullanan düşük maliyetli, sürdürülebilir ve çevre dostu bir kurutma sistemi tasarlanmıştır. Tasarlanan yeni sistemde makineye eklenen kurutma kanalları, kabindeki nemli havanın dışarı atılmasını ve kabin içine taze hava alınmasını sağlamaktadır. Çalışma kapsamında gerçekleştirilen deneyler EN 60436 standardına göre yapılmış olup; statik, fanlı ve tasarlanan doğal taşınımlı sistemin kurutma indeksi ve enerji tüketimi üç farklı program için karşılaştırılmıştır. Üç programın ortalama sonuçları incelendiğinde tasarlanan yeni kurutma sisteminin kurutma etkinliği, statik kurutma sistemine göre %9,9 daha yüksek iken fanlı kurutma sistemi ile benzerdir. Tasarlanan yeni kurutma sistemi en az enerji tüketirken, fanlı sistem %5 daha fazla enerji tüketmektedir. Statik sistemin ise %7,5 daha fazla enerji tükettiği gözlemlenmiştir.

* fatih.enginsel@arcelik.com
doi : 10.46399/muhendismakina.1356262

DESIGN AND EXPERIMENTAL ANALYSIS OF A NEW DRYING SYSTEM USING NATURAL VENTILATION FOR DISHWASHERS

Keywords

Dishwasher, drying, EN 60436, natural ventilation

Abstract

In addition to washing, the drying of loads is one of the main functions of dishwashers. Drying takes place by completely evaporating the water particles on the surface of the loads in the dishwasher baskets. In the dishwasher washing algorithm, the drying step is started after the hot rinse step. After the hot rinse step, the amount of moisture in the cabinet is very high. Although there is no water heating in the cabinet during the drying step, the moisture density continues to increase due to the evaporation of the loads in the basket. In order for evaporation on the loads, and therefore drying, to continue, the cabin humidity must be reduced. Drying systems developed to achieve this basically perform the mechanisms of condensing the evaporated water droplets on a colder surface or removing them from the machine. In this study, a low-cost, sustainable and environmentally friendly drying system using natural ventilation method was designed. In the new designed system, the drying channels added to the machine allow the humid air in the cabin to be evacuated and fresh air to be taken into the cabin. The experiments performed for the study were carried out according to EN 60436 standard. Drying score and energy consumption of static, fan and designed natural convection system were compared for three different programs. When the average results of the three programs are examined, the drying efficiency of the new designed drying system is 9.9% higher than the static drying system and similar to the fan drying system. The new designed drying system consumes the least energy, while the fan system consumes 5% more energy. The static system consumes 7.5% more energy.

Araştırma Makalesi			Research Article		
Başvuru Tarihi	:	06.09.2023	Submission Date	:	06.09.2023
Kabul Tarihi	:	24.01.2024	Accepted Date	:	24.01.2024

1. Giriş

1.1. Bulaşık Makinesinin Genel Yapısı ve Çalışma Mekanizması

Bulaşık makineleri, tencere, tabak, bardak, fincan, çatal, bıçak gibi yemek takımlarının, insan gücü kullanmadan temizlenmesi amacıyla geliştirilmiştir. Bu nedenle bulaşık makinelerinde elle yıkamada yapılan mekanik bir ovma işlemi yoktur. Temizleme işlemi, makine içerisinde bulunan yıkama kollarından çıkan sıcak ve basınçlı suyun, bulaşıklar üzerine püskürtülmesi ile gerçekleştirilir. Makinede basınçlı su elde etmek için bir pompa ve suyu istenilen sıcaklığa çıkarmak için de bir ısıtıcı bulunur. Ayrıca kir ve lekelerin daha kolay çözünmesi için, yıkama işlemi sırasında özel arıtıcılar (deterjan) ve durulama aşamasında kurutmaya da yardımcı olan parlatıcılar kullanılır.

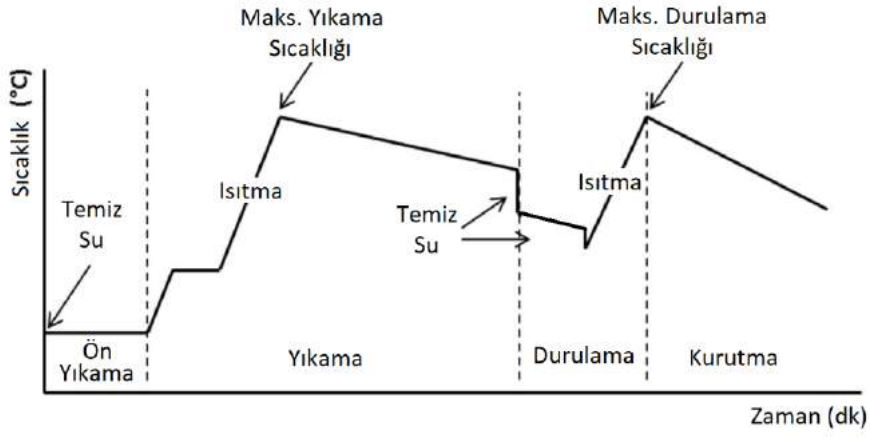

Şekil 1. Bulaşık Makinesi Program Akışı (Bengtsson, Berghel ve Renström, 2015)

Şekil 1'de bulaşık makinesinin program akışı gösterilmiştir. Standart bir bulaşık makinesi programı; ön yıkama, ana yıkama, durulama ve kurutma olarak dört adımdan oluşmaktadır.

Ön yıkama işlemi soğuk su ile kaba kirlerin bulaşıklardan uzaklaştırılması için yapılmaktadır. Çok kirli olmayan bulaşıklar yıkanacağı zaman ön yıkama adımı olmayan programlar kullanılmalıdır. Ana yıkama adımında ise su ısıtılır ve deterjan alımı yapılır. Bu adımda, kirlerin tümüyle bulaşıklardan uzaklaştırılması hedeflenir. Durulama adımı kendi içerisinde iki aşamaya bölünebilir. Soğuk su ile yapılan birinci durulama aşamasında, ana yıkama sonrasında bulaşıklar üzerinde kalan çıkmış kir taneleri ve deterjan kalıntılarının temizlenmesi işlemi yapılır. İkinci durulama aşamasında ise sıcak su kullanılarak bulaşıklar tümüyle deter-

jandan arındırılır. Sıcak su kullanımı, temizliğin ve kurutma veriminin arttırılmasını da sağlar. Bu adımda durulama suyu içerisine, parlatıcı alımı da gerçekleştirilir. Parlatıcı, lekeleri önler, parlaklık sağlar ve suyun yüzeylerde tutunmasını zorlaştırarak kurutmaya da yardımcı olur. Yıkama adımları tamamlandıktan sonra makine kurutma adımına geçer ve program döngüsünü tamamlar.

Bulaşık makinesinin temel işlevlerinden biri kurutmadır. Kurutma işleminde bulaşık makinesi içine yerleştirilmiş bulaşıkların üzerindeki suyun buharlaştırılması ve buharlaşan suyun bir bölgede yoğuşturulması ya da makine dışına atılması hedeflenmektedir. Kurutma adımı başlangıcında makinenin içerisinde yoğun ölçüde nem bulunmaktadır. Kurutma aşamasında, bulaşıklar üzerindeki buharlaşmanın etkisiyle, makine içerisindeki nem oranı, sürekli olarak artar. Yüksek bağıl nemdeki makine iç havasının, buharlaşan suyu tutabilmesi ve makinenin istenmeyen bölgelerinde veya bulaşıkların üzerinde yoğuşmaması için nemin denetimli bir şekilde uzaklaştırılması gerekmektedir.

1.2 Bulaşık Makinelerinde Kurutma Mekanizmaları

Kurutma ısı, kütle ve moment taşımalarını içeren, düşük ısıl verimle gerçekleşen enerji yoğun bir süreçtir (Sai ve Linga, 2010). Gözenekli ya da su emebilen bir cismin kurutulmasında iki evre söz konusudur. Bunlar suyun malzeme içinden taşınması ve yüzeyden buharlaşmasıdır (Mujumdar, 2006). Ancak gözenekli olmayan yani su tutmayan bulaşıkları kuruturken, yalnızca bulaşıkların yüzeyinde kalan suyun buharlaşması evresi gerçekleşir.

Bulaşık makinesinin kurutma aşamasında buharlaşma ve yoğuşma olayları oluşur. Makine içindeki bazı ıslak yüzeyler çiy noktasının üzerindedir ve buharlaşmayla karşılaşırlar. Diğer yüzeyler ise çiy noktasının altındadır ve yoğuşma yaşarlar. Bulaşık makinalarının kurutma sistemleri bulaşıklar üzerindeki buharlaşmayı özendirmek için geliştirilmiştir (Kumar, Rendall, Turnaoglu, Gluesenkamp, Patel, Abuheiba ve Gehl, 2021). Bunun sağlanabilmesi için makine iç havasının bağıl neminin düşürülmesi ve makine içindeki nemli havanın makine dışarısına taşınması ya da makine duvarlarında denetimli bir şekilde yoğuşturulması gerekir.

Bu amaçla geliştirilen kurutma sistemleri atmosfere açık veya kapalı, dinamik (fanlı) veya statik (fansız) olabilir. Bengtsson ve Berghel (2017), yaptıkları çalışmada bu sistemleri Şekil 2'de gösterildiği gibi beş kategoride ayrıntılı olarak incelemiştir. Bu gösterimde yer alan kurutma sistemlerinden farklı olan sistemler ise Şekil 3'te söz konusu çalışmadaki gösterime benzer şekilde oluşturulmuştur.

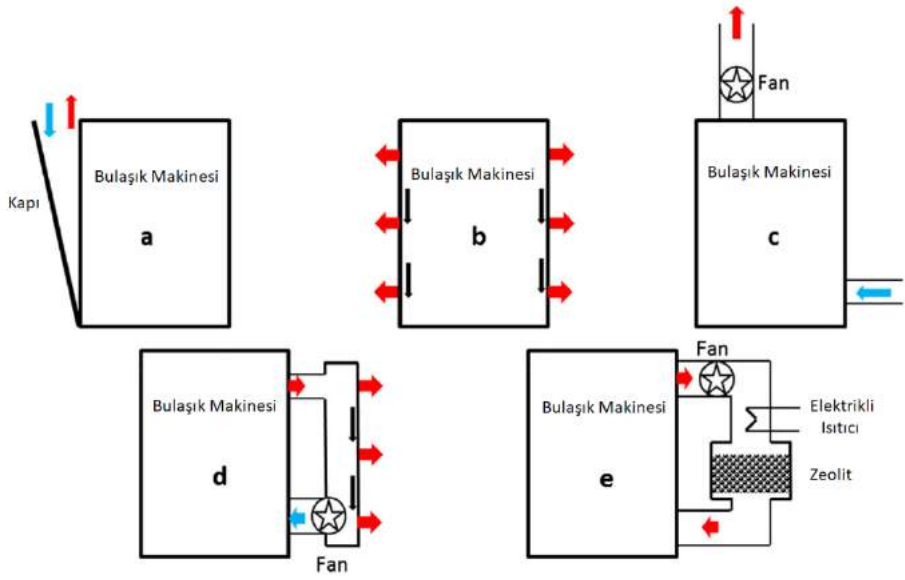

Şekil 2. Bulaşık Makinesinde Kullanılan Kurutma Sistemleri (Bengtsson ve Berghel, 2017)

Şekil 2.b'de gösterilen statik kapalı devre kurutmada, son durulama suyu sıcaklığı yüksek tutularak durulama sonrasında yıkanmış bulaşıkların yüzey sıcaklığının olabildiğince yüksek olmasından yararlanılır. Bulaşık makinasının gövde sıcaklığı, yüksek sıcaklıkta durulanan bulaşıklardan soğuk olacağı için buhar, gövde üzerinde yoğuşarak tabana iner ve sonrasında da atık su kanalına atılır. Bu sistemlerde kurutma süreleri uzun ve harcanan enerji yüksektir.

Jeong ve Lee (2014), bulaşık makinesinin enerji verimliliğinin araştırılması ile ilgili literatürde çalışmaların olduğu fakat kurutma mekanizması ile ilgili çalışmaların çok nadir olduğunu belirtmiş ve bu sebeple son durulama sıcaklığı, sirkülasyon akış hızı ve fan çalışma süresinin kurutma performansı üzerindeki etkilerini araştırmıştır. Çalışma, son durulama adımında yükler üzerinde depolanan enerjinin bulaşıklardaki suyun buharlaşmasından sorumlu olduğunu ve son durulama sıcaklığının kurutma performansını ve enerji tüketimini etkileyen ana faktör olduğunu göstermiştir. Bulaşık makinesinde yapılan kurutma işleminde, ortamdan gelen ısının bulaşıklara iletilmesi gerekmez. Bunun yerine, son durulama adımında bulaşıklar üzerinde depolanan ısının, bulaşık yüzeylerindeki suyu buharlaştırması gerçekleşir. Bu nedenle kurutma başlangıç sıcaklığı ile aynı olan son durulama sıcaklığı, bulaşıkları kuruturken önemli bir etkendir.

Statik kurutma işlemi sırasında otomatik olarak kapının açılması ile makine

içindeki buharın dışarı atılmasına olanak sağlayan uygulamalar da vardır. Şekil 2.a'da gösterilen bu uygulamalar, statik-açık devre kurutma olarak isimlendirilir.

Statik kurutmanın bazı özel uygulamalarında bir hava borusu da kullanılabilir. Makinenin üst kısmına doğal konveksiyon ile çıkan nemli buhar, bu bölgede yer alan bir delik ve bağlı olan hava kanalı yardımıyla makine dışına gönderilir. Bu uygulamaya ait şematik gösterim Şekil 3.a'da verilmiştir.

Statik sistemlerde kurutma veriminin arttırılması için makine yan duvarlarının daha çabuk soğutulmasını sağlayan yöntemler geliştirilmiştir. Yan duvarlarda gerçekleşen yoğuşmanın veriminin artırılabilmesi amacıyla bazı makinelerde büyük su cebi kullanılmaktadır. Bu ceplere kurutma sırasında soğuk su alınır. Bulaşık makinesi yan duvarlarının bu şekilde soğutulması, yoğuşmanın daha verimli olmasını sağlar.

Şekil 2.c'de gösterilen dinamik- açık devre kurutma sistemlerinde, hava borusu kullanan statik kurutmalı sisteme ek olarak bir fan kullanılır. Kullanılan fan ile doğal konveksiyon yerine zorlanmış konveksiyon ile ısı akışı sağlanarak kurutma sürelerinin kısaltılması hedeflenir. Bu sistemde de makine içindeki nemli hava fan tarafından emilir ve mutfak ortamına atılır.

Şekil 3.b'de gösterilmiş olan farklı bir uygulamada ise makineden çekilen nemli hava, mutfakta bulunan kuru hava ile karıştırılarak dış ortama gönderilir. Böylece mutfak ortamına gönderilen havadaki nem derişimi azaltılmış olur.

Şekil 3. Diğer Örnek Kurutma Sistemleri

Şekil 2.d'de gösterilen dinamik- kapalı devre kurutma sistemlerinde ise makine içerisinden çekilen nemli hava bir kanaldan geçirilerek tekrar makine içine gönderilir. Bu kanalda oluşturulan geometrik eklentiler yardımıyla yoğuşma yüzeyi elde edilir.

Şekli 3.c'de benzer sistemin geliştirilmiş bir uygulamasında makineden çekilen nemli havanın bir kısmı doğrudan mutfak ortamına verilirken kalan kısmı ise kuru hava ile karıştırılarak tekrar makine içerisine gönderilir. Makine içine gönderilmiş olan görece kuru ve ılık hava yoluyla, kurutma verimi artırılır.

Dinamik- kapalı devre kurutma sistemlerinde nem tutucu malzemelerin kullanıldığı uygulamalar da bulunur. Bunlardan en bilineni zeolit kullanımıdır. Makine içerisinden bir fan yardımıyla emilen nemli hava, içinde zeolit bulunan bir hazne üzerinden geçirilerek tekrar makine içine verilir. Zeolit üzerinden geçen nemli hava, su buharını kaybederek kuru bir şekilde makine içine tekrar gönderilir. Böylece makine dışına herhangi bir çıkış olmadan kurutma işlemi başarılı bir biçimde tamamlanabilir. Sisteme ait şema Şekil 2.e'de gösterilmiştir.

Hauer ve Fischer (2011), çalışmalarında adsorpsiyon yöntemi aracılığıyla bulaşık makinesinin enerji tüketimini azaltmayı hedeflemiştir. Geleneksel bulaşık makinelerinde kurutma adımı öncesinde gerçekleştirilen son durulama adımında su sıcaklığı kurutmanın sağlanabilmesi için yüksek tutulur. Yapılan çalışma ile bu su ısıtma aşaması atlandı ve bulaşıkların sıcak hava ile kurutulduğu bir adsorpsiyon aşaması eklenmiştir. Nem tutucu malzeme olarak zeolit kullanılmıştır. Çalışma sonucunda enerji tüketimi, geleneksel bir bulaşık makinesine kıyasla %25 oranında düşürülmüştür.

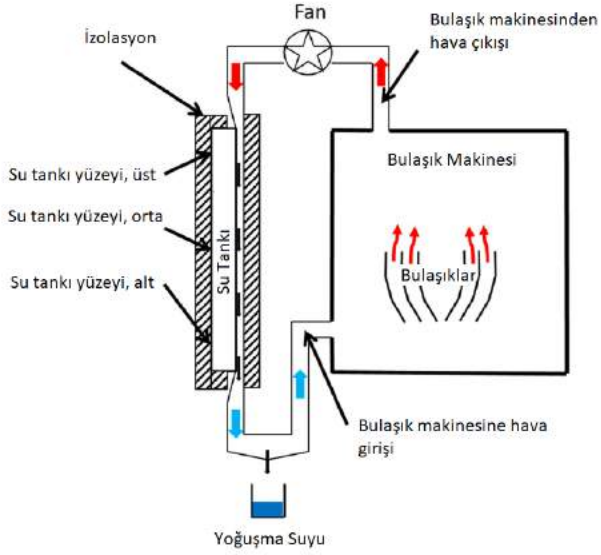

Şekil 4. Isı Pompalı Bulaşık Makinesi Kurutma Sistemi (Bengtsson ve Berghel, 2017).

Bengtsson ve Berghel (2017), ısı pompalı bir bulaşık makinesi için yeni bir kurutma yöntemi önermiştir. Isı pompalı bulaşık makinesinde, kondenserde yıkama suyu ısıtılırken evaporatörde ise soğuk bir su deposu kaynağı oluşmaktadır. Önerilen yöntemde kurutma işlemi, bir fanın makine içindeki nemli havayı kapalı bir sistemde evaporatör üzerinden sirküle etmesiyle gerçekleşir. Sistem, yükler üzerindeki suyun, makine kabininde buharlaşıp ve daha sonra evaporatör soğuk

yüzeyinde yoğuşması prensibi ile çalışır. Sonuçlar, ısı pompalı kurutma yönteminin mevcut kurutma yöntemine kıyasla daha verimli olduğunu göstermiştir. Kurutma başlangıç sıcaklığı ve kurutma süresinin, kurutma performansı üzerinde önemli bir etkiye sahip olduğu tespit edilmiştir. Şekil 4'te ısı pompalı bir bulaşık makinesinin kurutma devresi şeması gösterilmiştir.

2. Tasarım Çalışmaları

2.1 Teorik Model

Şekil 5'te şematik olarak çalışma mekanizması gösterilen bu çalışmada, dinamik kurutma sistemleri ile benzer verimde ancak elektrikle çalışan herhangi bir bileşen içermeyen, statik-bacalı bir kurutma sistemi geliştirilmiştir. Sistemde makine içindeki buharın dışarı çıkışı için bir baca ve hava desteği için de bir emiş açıklığı yer almaktadır. Bu şekilde baca açıklığından makine içerisindeki sıcak ve nemli hava makine dışına atılırken, hava emiş açıklığından makine içine taze hava girişi olmaktadır. Sistem temel olarak kabin içindeki buharın, kurutma adımında denetimli ve hızlı bir şekilde atılması ilkesine dayanmaktadır.

Geliştirilen bu sistem yardımıyla makine içerisindeki nemli ve sıcak hava daha hızlı bir şekilde dışarıya atılır. Nemli ve sıcak havanın yerini ise kuru ve soğuk olan ortam havası doldurur. Bu yöntem ile makine içerisinde buharlaşan suyun hava içerisinde tutulma gücü sürekli olarak arttığından bulaşıkların üzerinde yeniden yoğuşma olmasının önüne geçilir. Ayrıca içeriye taze hava dolmasından ötürü bulaşıklar ile makine iç havasının sıcaklık farkı artar. Bu da bulaşıklar üzerindeki kütle transferini, yani buharlaşmayı hızlandıracak yönde bir etki gösterir. Bu şekilde kurutma verimi iyileşir. Şekil 5'te sistemin çalışma ilkesini gösteren şema verilmiştir.

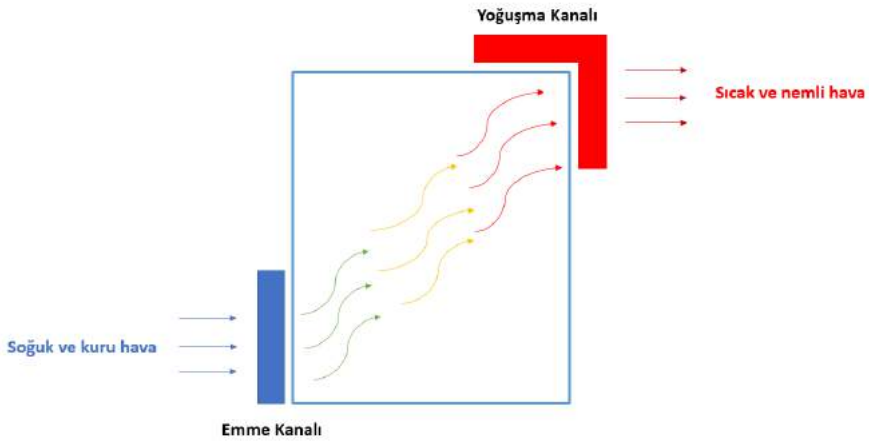

Şekil 5. Tasarlanan Sistemi Gösteren Şema

Sistemin çalışması doğal taşınım ilkelerine dayanmaktadır. Eğer makineye bir baca açıklığı açılırsa, makine içerisindeki sıcak ve nemli hava yükselme eğiliminde olduğundan doğal taşınım yoluyla kontrol hacmini terk edecektir. Baca açıklığına ek olarak açılan bir emiş açıklığı ise atılan nemli havanın yerine kuru havanın alınmasını sağlar. Ayrıca bu açıklık kurutma süresini kısaltıcı etkiye de sahiptir.

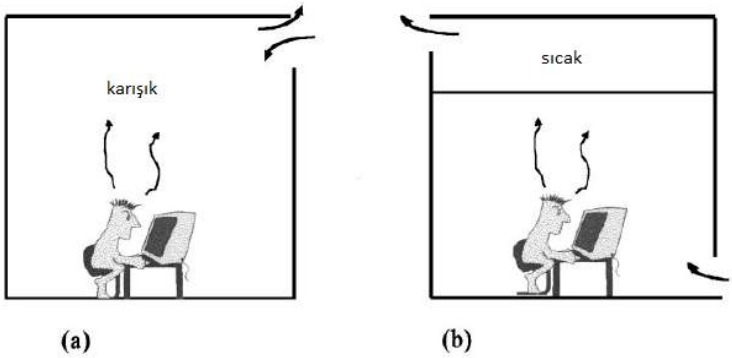

Şekil 6. (a) Karışım Havalandırması, (b) Yer Değiştirme Havalandırması (Linden, 1999)

Linden (1999), doğal havalandırma ile ilgili yaptığı çalışmasında Şekil 6.a'da gösterilen havalandırma tipi ile Şekil 6.b'de gösterilen havalandırma sisteminin farkını incelemiştir. Şekil 6.a'da gösterilen sistemde makine hacmi içerisinde homojen bir sıcaklık oluşurken, Şekil 6.b'de ise üst kısımların daha sıcak olduğu gösterilmektedir. Buna ek olarak Şekil 6.a'daki sistemde odanın havalandırması için Şekil 6.b'de gösterilen sisteme göre uzun zaman gerektiğini belirtmektedir.

Benzer olaylar farklı alanlarda da karşımıza çıkmaktadır. Güç santrallerindeki doğal çekişli soğutma kuleleri, buzdolaplarının ve soğuk hava depolarının kapılarının açılmasıyla gerçekleşen hava infiltrasyonu ve kuzine sobalar buna örnek olarak verilebilir.

Karlsson ve Quintiere (1999), yangın dinamiği hesaplamalarında doğal havalandırma ilkelerini kullanmıştır. Geliştirilen sistem de benzer şekilde doğal havalandırma yöntemlerindeki baca etkisi ya da yığın etkisi ilkesine benzemektedir. Bu nedenle aşağıda ayrıntıları verilen mühendislik hesaplamalarında Karlsson ve Quintiere'ın Enclosure Fire Dynamics (1999) kitabı kaynak olarak kullanılmıştır.

Doğal havalandırmada havanın bir açıklıktan içeri ve dışarı akışı, basınç farkından dolayı gerçekleşir. Akışkanların hareketi her zaman yüksek basınçlı bölgeden düşük basınçlı bölgeye doğrudur. Şekil 7'de üst ve alt bölgesinde açıklıkları olan ve denetlenen bir kapalı hacim gösterilmiştir. Bu hacmi, geliştirilmiş olan kurutma sisteminin kaba bir modeli olarak kabul edebilirsiniz. Şekilde, dış ortam

hava yoğunluğu ve sıcaklığı ρ_a ve T_a, kontrol hacmi hava yoğunluğu ve sıcaklığı ρ_g ve T_g ile gösterilmiştir. Kontrol hacmi sıcaklığı dış ortam sıcaklığından daha yüksek ve sabit olduğu kabul edilirse, kontrol hacmine alt açıklıktan giren bir soğuk hava akışı (T_a) ve üst açıklıktan çıkan bir sıcak hava akışı (T_g) beklenir. Bunun nedeni hidrostatik basınç farkıdır (Karlsson ve Quintiere, 1999).

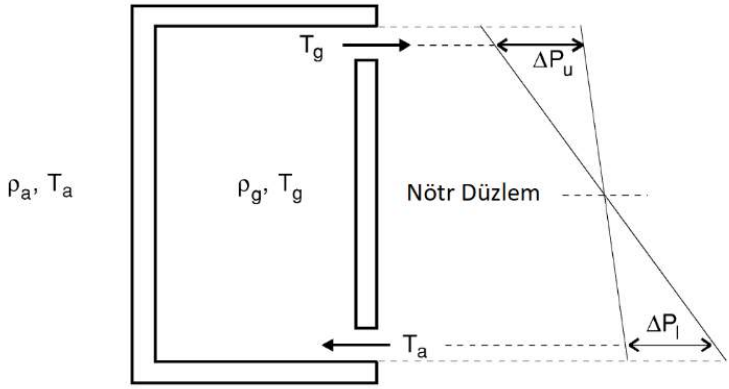

Şekil 7. Isıtılmış Bir Kapalı Hacimdeki Hidrostatik Basınç Farkları (Karlsson ve Quintiere, 1999).

Kontrol hacmi içi veya dışındaki basınç profillerinde herhangi bir süreksizlik olmaması nedeniyle profiller nötr düzlem olarak adlandırılan belirli bir yükseklikte kesişecektir. Bu yükseklikte basınç farkları sıfırdır. Nötr düzlem Şekil 7'de gösterilen iki açıklık arasında herhangi bir yerde olabilir. Nötr düzlemin yüksekliği, açıklıklardaki akış direnci ve sıcaklık farkının büyüklüğü ile belirlenir. Örneğin alt açıklık büyükse veya düşük akış direncine sahipse nötr düzlem, alt açıklığa yakın olacaktır.

Basınç farkı, kontrol hacmi içi ve dışındaki yoğunluk farkından kaynaklanır. Yoğunluk farkına ise iç ve dış ortamdaki sıcaklık farkı neden olur. Diğer bir deyişle ısınan havanın yükselme eğiliminde olmasının nedeni, hava içindeki moleküllerin genleşip yoğunluğunun azalmasıdır. Aynı şekilde soğuyan hava da yoğunluğun artması sonucunda alçalma eğilimindedir. Sıcak gazların kaldırma kuvvetinden veya daha doğrusu sıcak ve soğuk gazlar arasındaki yoğunluk farklarından dolayı basınç farkı oluşur.

Sistemdeki hava akışının basınç ve hız ilişkisini anlatmak için Bernoulli denklemi kullanılmıştır. Esas olarak viskoziteden kaynaklanan kayıpların düşük olduğu havalandırma açıklıklarında, havanın laminer akışı inceleneceği için sürtünme kaybı olmadığı ve akışkanın sıkıştırılamaz olduğu kabul edilir (Karlsson ve Quintiere, 1999).

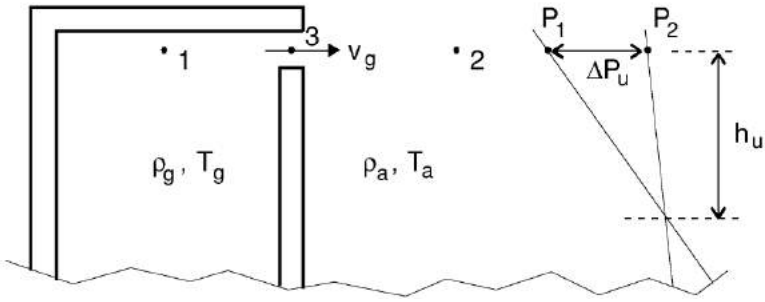

Şekil 8. Isıtılmış Bölümün Üst Açıklığının Ayrıntılı Görüntüsü (Karlsson ve Quintiere, 1999)

Bernoulli denklemi ilk olarak Şekil 8'deki 1 ve 2 noktaları için yazılarak bir eşitlik elde edilir. 1 ve 2 noktalarında hız sıfır olduğu için denklem (1) formunda yazılabilir.

$$P_1 - P_2 = h_2\rho_2 g - h_1\rho_1 g \tag{1}$$

Şekil 8'de görüldüğü gibi 1 ve 2 noktalarında yükseklik eşittir. Bu durumda $h_1=h_2=h_u$ olduğundan 1 ve 2 noktaları arasındaki hidrostatik basınç farkı ΔPu için ifade:

$$\Delta P_u = h_u(\rho_a - \rho_g)g \tag{2}$$

1 ve 3 noktaları arasında yazılan Bernoulli denkleminden bir eşitlik (3) daha elde edilir. Bu eşitliğin yazılmasında amaç kütle akış hızının hesaplanmasıdır.

$$P_1 + \frac{1}{2}v_1^2\rho_1 + h_1\rho_1 g = P_3 + \frac{1}{2}v_3^2\rho_3 + h_3\rho_3 g \tag{3}$$

1 noktasındaki hız değeri v1=0'dır. Kontrol hacmi içindeki hava yoğunluğu, kontrol hacmi çıkış noktasındaki hava yoğunluğu ile aynıdır ($\rho_1=\rho_3=\rho_g$). Dolayısıyla eşitlik (4) halini alır.

$$P_1 - P_3 = \frac{1}{2}v_3^2\rho_3 \tag{4}$$

Son olarak, nötr düzlemden 1 ve 3 noktalarının yükseklikleri aynıdır ($h_1=h_3=h_u$). Denklem sadeleştirilerek (5) halini alır.

$$\Delta P_u = \frac{1}{2}v_g^2\rho_g \tag{5}$$

İlk elde edilen eşitlik ikinci eşitlikte yerine yazılarak havanın hu yüksekliğindeki çıkış hızı ile ilgili (6) numaralı denkleme ulaşılır.

$$v_g = \sqrt{\frac{2\Delta P_u}{\rho_g}} = \sqrt{\frac{2h_u(\rho_a - \rho_g)g}{\rho_g}} \tag{6}$$

Üst açıklık için yapılana benzer şekilde Bernoulli denklemi kullanılarak alt açıklık için de denklemler türetilebilir. Şekil 9, bazı ek notasyonlarla birlikte Şekil 8'in bir benzeridir. Üst noktaya atıfta bulunan değişkenler daha önce olduğu gibi "*u*" alt indisine ve alt noktaya atıfta bulunanlar "*l*" alt indisine sahiptir. Kontrol hacmi içindeki havayı "*g*" indisi, dışındaki havayı ise "*a*" indisi ifade eder.

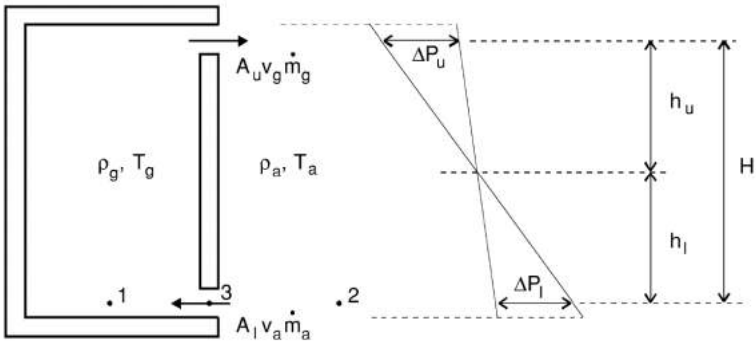

Şekil 9. Notasyonların Eklendiği Alt ve Üst Açıklığın Ayrıntılı Görüntüsü (Karlsson ve Quintiere, 1999)

Bernoulli denklemi ilk olarak Şekil 9'daki 1 ve 2 noktaları için yazılarak bir eşitlik elde edilir. 1 ve 2 noktalarında hız sıfır olduğu için denklem (7) formunda yazılabilir.

$$P_1 - P_2 = h_2\rho_2 g - h_1\rho_1 g \tag{7}$$

Şekil 9'da gösterildiği gibi h_1=h_2=h_1 olduğundan 1 ve 2 noktaları arasındaki hidrostatik basınç farkı ΔP_l için ifade şu hale gelir:

$$\Delta P_l = h_l(\rho_a - \rho_g)g \tag{8}$$

2 ve 3 noktaları arasında yazılan Bernoulli denkleminden bir eşitlik (9) daha elde edilir. Bu eşitliğin yazılmasında amaç, kütle akış hızının hesaplanmasıdır.

$$P_2 + \frac{1}{2}v_2^2\rho_2 + h_2\rho_2 g = P_3 + \frac{1}{2}v_3^2\rho_3 + h_3\rho_3 g \tag{9}$$

2 noktasındaki hız değeri v_2=0'dır. Kontrol hacmi içindeki hava yoğunluğu, kontrol hacmi çıkış noktasındaki hava yoğunluğu ile aynıdır ($\rho_2=\rho_3=\rho_a$). Dolayısıyla eşitlik (10) halini alır.

$$P_2 - P_3 = \frac{1}{2} v_3^2 \rho_3 \tag{10}$$

Son olarak, nötr düzlemden 2 ve 3 noktalarının yükseklikleri aynıdır ($h_2=h_3=h_l$). Denklem sadeleştirilerek (11) halini alır.

$$\Delta P_l = \frac{1}{2} v_a^2 \rho_a \tag{11}$$

İlk elde edilen eşitlik ikinci eşitlikte yerine yazılarak havanın h_l yüksekliğindeki giriş hızı ile ilgili (12) numaralı denkleme ulaşılır.

$$v_a = \sqrt{\frac{2\Delta P_u}{\rho_a}} = \sqrt{\frac{2h_l(\rho_a - \rho_g)g}{\rho_a}} \tag{12}$$

Bir açıklıktan geçen kütle akışının temel doğa yasalarını kullanarak hassas bir şekilde hesaplanması Navier-Stokes denklemlerinin çözülmesiyle gerçekleştirilebilir. Bu çözümlerin gerçekleştirilmesinde güçlü bilgisayarlar kullanılır. Bernoulli denklemi yalnızca idealize edilmiş akış koşulları için geçerlidir. Bununla birlikte tüm mühendislik amaçları için yukarıda verilen denklemlerin bazı düzeltme katsayıları ile birlikte kullanımı da gerçek sonuçlara önemli ölçüde yaklaşım sağlar (Karlsson ve Quintiere, 1999).

Bir kontrol hacminde bulunan açıklıklar arasında basınç farkı olduğunda, akışkan yüksek basınç bölgesinden düşük basınç bölgesine hareket eder. Pratikte akışkan ideal (sürtünmesiz, sıkıştırılamaz ve izotermal) değildir ve akışa karşı bir parça direnç vardır. Bu direnç, temelde açıklığın yalnızca bir bölümünün akışın içinden etkin bir şekilde akmasına izin vereceğini belirten bir akış katsayısı ile hesaba katılır. Akış katsayısı C_d ile gösterilir.

Basınç farkının tüm kontrol hacmi yüksekliği boyunca sabit bir değer olduğu sistemlerde, hızın tüm yükseklik boyunca sabit olduğu da söylenebilir. Kontrol hacmi kenarlarına çok yakın bölgelerde bu durum söz konusu olamaz. C_d akış katsayısı bu durumda kenar etkisini hesaba katar. Bu durumda kütle akışı (13) numaralı denklemdeki gibi yazılabilir:

$$\dot{m} = C_d A v \rho \tag{13}$$

Burada A kesit alanı, v kesit üzerindeki sabit hızı ve ρ akışkanın yoğunluğunu

gösterir. Bu eşitlik hızın kontrol hacmi yüksekliği boyunca sabit olması durumunda kurulabilir. Aksi durumlarda toplam kütle akışının elde edilebilmesi için hız görünüşünün, yüksekliğe göre değişimi dikkate alınmalıdır.

Buradan yola çıkarak denklem (6) ve (12) de elde edilen üst ve alt noktalardaki çıkış hızlarından kütlesel debiler:

Buradan yola çıkarak denklem (6) ve (12) de elde edilen üst ve alt noktalardaki çıkış hızlarından kütlesel debiler:

$$\dot{m}_g = C_d A_u \rho_g \sqrt{\frac{2h_u(\rho_a - \rho_g)g}{\rho_g}} \tag{14}$$

$$\dot{m}_a = C_d A_l \rho_a \sqrt{\frac{2h_l(\rho_a - \rho_g)g}{\rho_a}} \tag{15}$$

Kütlenin korunumu yasası gereği giren kütlesel debi ile çıkan kütlesel debi birbirine eşittir. Bu durumda (14) ve (15) numaralı denklemler birbirine eşitlenirse yükseklik ve hava yoğunluklarının birbiri ile olan ilişkisini açıklayan (16) numaralı eşitlik elde edilir.

$$\frac{h_l}{h_u} = \left(\frac{A_u}{A_l}\right)^2 \frac{\rho_g}{\rho_a} \tag{16}$$

Bu bölümde elde edilen denklemler yorumlanarak tasarıma yardımcı olacak çıkarımlar yapılmıştır:

- Debilerin artması, baca açıklığı yardımıyla makine dışına atılan nemli havanın ve hava emiş açıklığı yardımıyla makine içine alınan taze havanın miktarlarının artması demektir. Makine içerisindeki havanın giriş-çıkışının artması makine içerisindeki nemin sürekli olarak azaltılması ve makine içindeki havanın nem tutma yeteneğinin artması anlamına gelmektedir. Yani, bulaşıklar üzerinden buharlaşan suyun tekrardan bulaşıklar üzerinde yoğuşmasının önüne geçilmiş olur.
- Ayrıca, hava giriş-çıkışının hızlanması, içeriye daha çok taze (soğuk ve kuru) hava dolması anlamına gelir. Bu şekilde, makine iç sıcaklıkları daha hızlı bir şekilde düşer ve makine içindeki hava ile bulaşıklar arasındaki sıcaklık farkı artar. Bu da bulaşıklar üzerindeki kütle transferini, yani buharlaşmayı hızlandıracak yönde bir etki gösterir. Bu şekilde kurutma verimi iyileşir.
- Açıklıkların konumları önemli değişkenlerdir ve denklemlerde çarpan duru-

munda bulunmaktadırlar. Baca açıklığı ile hava emiş açıklığı arasında yükseklik farkı bulunmalıdır ve baca açıklığı her zaman hava emiş açıklığından yukarıda olmalıdır. Aradaki yükseklik farkı arttıkça, kontrol hacmi içerisine giren (taze hava) ve dışarıya atılan (nemli hava) hava hızları, buna bağlı olarak debileri artacaktır ve daha hızlı bir hava giriş-çıkışı gerçekleşecektir. Böylece, baca açıklığını olabildiğince en yüksek konuma, hava emiş açıklığını ise olabildiğince en alçak konuma yerleştirmek, çarpan durumunda olan yükseklik değişkenini büyütür. Bunun sonucunda hava hızları ve debi yükselir ve makine dışına atılan nemli hava ve makine içine alınan taze hava miktarları artar.

- Açıklıkların kesit alanları da önemli değişkenlerdir ve denklemlerde çarpan durumunda bulunmaktadırlar. Baca ve hava emiş açıklıklarının kesit alanları, hacimsel debi denklemlerinde çarpan durumunda olduğundan, bu açıklıklar büyütüldüğünde baca açıklığından makine dışarısına çıkan nemli havanın ve hava emiş açıklığından içeriye giren taze havanın hacimsel debileri de aynı oranda artar.
- Söz konusu sistemde, açıklıkların yükseklik farkları dışında konumları da önem taşımaktadır. Sistem her ne kadar yükseklik farkı olduğu sürece çalışır durumda olsa da konum düzenlemeleriyle sistemin verimi artırılabilecektir. Baca açıklığı ile hava emiş açıklığının karşılıklı olarak konumlandırılması bu düzenlemelerden biridir. Makinenin tercihen alt bölümlerinde bulunan hava emiş açığından, nemli ve sıcak hava bulunan makineye taze (kuru ve soğuk) hava girişi olur. Nemli ve sıcak hava yükselme eğiliminde olacağından baca açıklığından dışarıya çıkar. Havanın akış yolu da bu doğal harekete göre gerçekleşir.

Baca açıklığı ve hava emiş açıklıklarının karşılıklı olması havanın yolunu şekillendirir. Makinenin bir köşesindeki hava emiş açıklığından hava girip, karşı köşesindeki baca açıklığından dışarıya çıktığı bir sistemde, makine içerisindeki en yüksek sayıda bulaşık akış yolu üzerinde kalır. Bu şekilde hava akışı daha çok bulaşık üzerinden geçtiğinden, bulaşıklar üzerindeki kütle transferi artar. Bu da bulaşıklar üzerinden daha fazla su damlasının buharlaşacağı anlamını taşır. Yani kurutma verimi yükselir.

2.2. Tasarım Doğrulama

Bu bölümde, tasarlanan kurutma sisteminin işlevinin kanıtlanması amaçlanmıştır. Bu doğrultuda sistemi oluşturan emme ve yoğuşma kanallarının öncül tasarımları yapılmış ve Şekil 10'da gösterilen ilk örnek (prototip) üretimleri gerçekleştirilmiştir. Prototipler üzerinden yapılan sıcaklık ölçümleri ile sistemin işlevselliği araştırılmıştır. Ölçümlerde ±0,5 °C doğrulukta ölçüm yapabilen termokupllar kullanılmıştır.

Şekil 10. Prototip Test Bulaşık Makinesi

İlk olarak yalnız kurutma çevriminde ölçümler alınmıştır. Yoğuşma kanalına makine içerisinden nemli havanın girdiği açıklığa, taze havanın emildiği açıklığa ve kanalın çıkış açıklığına termokupllar yerleştirilmiştir. Sıcaklık değerleri Şekil 11'de verilmiştir. İlk testlerin ardından, yıkama çevrimi süresince ölçümler alınarak sistemin çalışma durumu incelenmiştir. Sıcaklık sensörleri makinenin bulunduğu ortama, makine içine, yoğuşma kanalı çıkışına ve emme kanalı girişine yerleştirilmiştir. Ölçülen sıcaklık değerleri Şekil 12'de gösterilmiştir.

Kanaldan dışarıya atılan havanın sıcaklığı, beklendiği şekilde makine içerisindeki hava ile makine yan bölümünden giren taze havanın karışımından elde edilen bir sıcaklıktır. Makine yan bölümünün test odasından daha sıcak olmasının nedeni yıkama süresinde makine duvarlarının ısınarak yan bölümündeki havayı da ısıtmasıdır. Testler tezgâh içine gömülü ankastre bir ürün üzerinde yapıldığı için makine üzerine yerleştirilen kabin de yalıtım etkisi yaratmaktadır. Doğrulama amacıyla açıklıkların önüne cam yüzeyler konmuş ve yoğuşma olmadığı gözlenmiştir. Test sonuçlarına göre tasarlanan kurutma sisteminin işlevini yerine getirdiği kanıtlanmıştır.

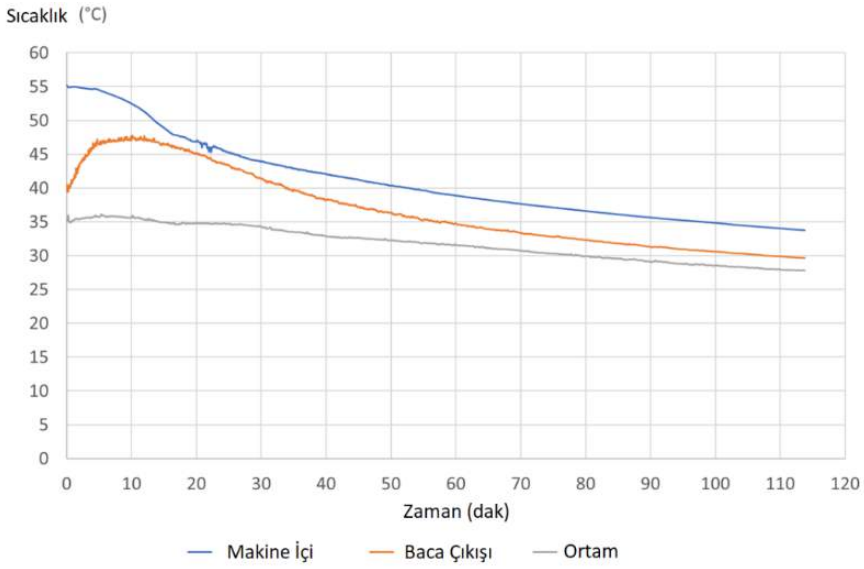

Şekil 11. Kurutma Adımı Boyunca Sıcaklık Ölçümleri

Kanaldan dışarıya atılan havanın sıcaklığı, beklendiği şekilde makine içerisindeki hava ile makine yan bölümünden giren taze havanın karışımından elde edilen bir sıcaklıktır. Makine yan bölümünün test odasından daha sıcak olmasının nedeni yıkama süresinde makine duvarlarının ısınarak yan bölümündeki havayı da ısıtmasıdır. Testler tezgâh içine gömülü ankastre bir ürün üzerinde yapıldığı için makine üzerine yerleştirilen kabin de yalıtım etkisi yaratmaktadır. Doğrulama amacıyla açıklıkların önüne cam yüzeyler konmuş ve yoğuşma olmadığı gözlenmiştir. Test sonuçlarına göre tasarlanan kurutma sisteminin işlevini yerine getirdiği kanıtlanmıştır.

Yoğuşma kanalı çıkışında yer alan sensör makine iç sıcaklıklarına benzer bir eğilimde sıcaklık değişimini göstermektedir. Emme kanalı girişindeki sensör ise kabin iç sıcaklığından bağımsız olarak yalnızca dış ortam sıcaklığını okumaktadır. Bu demektir ki; makinenin baca açıklığından makine dışarısına sıcak ve nemli hava salımı, hava emiş açıklığından ise makine içerisine taze hava beslemesi olmaktadır. Sonuçlar, sistemin tam olarak beklendiği gibi çalıştığını göstermektedir.

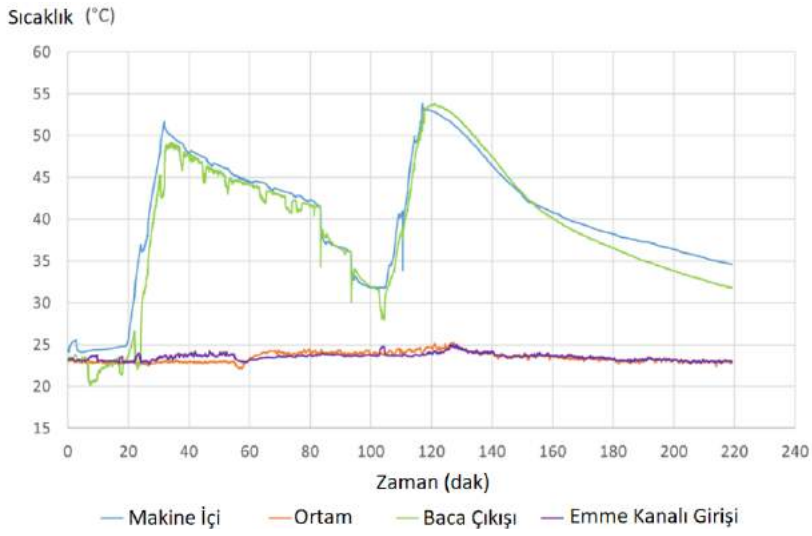

Şekil 12. Yıkama Programı Boyunca Sıcaklık Ölçümler

3. Deneysel Çalışmalar

3.1 Yöntem

Bulaşık makinelerinin performans kriteri; yıkama ve kurutma değerleri, enerji ve su tüketimi, program süresi ve ses gücü düzeyine göre belirlenir. Ölçüm yöntemi olarak EN 60436 numaralı "Elektrikli bulaşık makinaları: Ev ve benzeri yerlerde kullanılan - performans ölçme metotları" standardı kullanılmaktadır.

Tasarlanan sistem, kurutma sistemi üzerine kurulduğundan yıkama performansı ve su tüketimine etkisi yoktur. Bu nedenle yıkama performansı ve su tüketimi irdelenmemiştir. Sistemin ses düzeyini yükseltmesi ile ilgili bir risk de öngörülmemektedir. Fanlı kurutma sistemlerine göre ses düzeyinde düşüş beklenmektedir ancak tasarlanan sistemin ses düzeyini düşürme hedefi olmadığından ses düzeyi de araştırılmamıştır.

Yıkama ve kurutma indekslerinin hesaplanmasında birbiri ardına sıralı testler yapılabileceği gibi (yıkama ve kurutma) ayrı ayrı testler de (yıkama ya da kurutma) yapılabilir. Ancak yıkama ve kurutma puanı ile birlikte su ve enerji tüketimi de belirlenecek ise sıralı testler yapılmalıdır. Sıralı testlerde kirli yükler kullanılırken yalnızca kurutma puanının hesaplanacağı ayrı yapılan bir testte ise temiz yükler kullanılabilir. Çalışma kapsamında enerji tüketimi de belirleneceği için sıralı testler yapılmıştır.

Performans testlerine başlamadan önce EN 60436 standardında belirlenen aşağıda sıralanan şartlar sağlanmıştır:

- Şebeke frekansı: 50 Hz ± %1 ve şebeke voltajı: 230 V ± %1
- Ortam sıcaklığı 23 ± 2°C ve bağıl nem: %55 ± 5
- Su giriş sıcaklığı 15±2°C, sertliği 2.5 ± 0.5 mmol/l, basıncı 240 ± 20 kPa

Testlerde standartta belirtilen referans deterjan ve parlatıcı kullanılmıştır. Deterjan ve parlatıcı miktarı üretici firma tarafından önerildiği kadardır.

Çalışma kapsamında statik, fanlı ve tasarlanan doğal taşınımlı sistemin enerji tüketimleri standartta belirtildiği üzere koşul ve yöntemlerde enerji analizörü (Entes MPR-53S, Doğruluk: ±%1) ile ölçülmüştür.

3.2 Kurutma Indeksinin Hesaplanması

Kurutma performansının değerlendirmesinde EN 60436 numaralı standartta tanımlanan ışık kaynağı kullanılarak yükler üzerindeki damlacık miktarının sayılması yöntemi kullanılır. Program süresi tamamlandıktan 30 dakika sonra makine kapağı açılır. Değerlendirmeye alt sepetteki parçalardan başlanır. Daha sonra üst sepetteki parçalar, en son ise kaşık-çatal ve servis takımları değerlendirilir. Bir parçanın değerlendirilmesi için ortalama 8 s harcanmalıdır. Yükler kuruluk düzeyine göre kuru, orta ve nemli olarak değerlendirilir.

- Kuru: bir parçanın tamamen kuru olmasını belirtir ve puanlamada “2” puan alır.
- Orta: bir parçanın iki damlaya kadar su veya hareketli bir su izi içermesini belirtir (toplam ıslak alan 50 mm^2 den az olmalıdır) ve puanlamada “1” puan alır.
- Nemli: bir parçanın iki damladan fazla su, bir damla su ile hareketli bir su izi, iki hareketli su izi veya fincan, bardak çukur bölgelerinde kalmış suyu veya toplam ıslak alanın 50 mm^2 den fazla olmasını belirtir ve puanlamada “0” puan alır.

Belirtilen değerlendirme kriterlerine uygun olarak Tablo 1 doldurulur.

Tablo 1. Kurutma Performansı Değerlendirme Formu

Parça Tanımı EN 60436 (EK-A)	Parça No	Kurutulan Parçalar	Kategoriye göre parça sayısı	b puanını almış öğe sayısı, a_b			$T_z = \sum a_b \times b$
			S_z	2	1	0	
A1	1	Yemek Tabağı					
A2	2	Tatlı Tabağı					
A3	3	Tatlı Kasesi					
A4	4	Kupa					
A5+B5	5	Bardak					
A6+B6	6	Çatal					
A7+B7	7	Bıçak					
A8+B8	8	Çorba Kaşığı					
A9+B9	9	Tatlı Kaşığı					
A10+B10	10	Çay Kaşığı					
B1	11	Çorba Kasesi					
B2	12	Melamin Tatlı Tabağı					
B3	13	Fincan Tabağı					
B4	14	Kahve Kupası					
S1a	15	Küçük Kap					
S1b	16	Fırın Kabı					
S2	17	Cam Kâse					
S3	18	Oval Tabak					
S4	19	Melamin Kâse					
S5	20	Servis Kaşığı					
S6	21	Servis Çatalı					
S7	22	Sos Kepçesi					
		N=	S_z=				$\sum Tz$=

Notlar: Test No:

Sofra takımının her bir parçası için T_z değeri (17) formülüne göre hesaplanır. Bu formülde $a_b \times b$ her bir parça için 0-2 arasında verilen puan ile bu puanı alan parça sayısının çarpımını ifade eder.

$$T_z = \sum a_b \times b \tag{17}$$

Toplam yıkanan parça sayısı N ile ifade edilir. (18) numaralı formül ile hesaplanır.

$$N = \sum S_z \tag{18}$$

Bir deneye ait kurutma puanı T_i, her bir parça türü için hesaplanan T_z değerleri kullanılarak (19) numaralı formül ile hesaplanır.

$$T_z = \sum a_b \times b \tag{19}$$

Test edilen makine için kurutma puanı T, n deney sonunda elde edilen T_i değerlerinin aritmetik ortalamasıdır. (20) numaralı formül ile hesaplanır.

$$\mathrm{T} = \frac{1}{n}\sum T_i \tag{20}$$

3.3 Standart Koşul Test Sonuçları

EN 60436 standardında belirtilen koşullarda tasarlanan doğal taşınımlı kurutma sistemi, fanlı kurutma sistemi ve statik sistem kıyaslanmıştır. Karşılaştırılması yapılan her üç sistem de üçer kez teste alınmış ve ortalama kurutma puanları hesaplanmıştır.

Karşılaştırmanın daha anlaşılır olması için hesaplanan kurutma puanları ve ölçülen enerji tüketimleri statik sistem birinci program sonucu 1 birim olacak şekilde indekslenmiştir.

Şekil 13'te her üç sistemin üç farklı yıkama programındaki karşılaştırmalı verim sonuçları yer almaktadır. Şekil 14'te ise karşılaştırmalı enerji tüketimleri verilmiştir.

Tasarlanan kurutma sistemi, standart koşullarda yapılan testlerde tüm yıkama programlarında statik kurutma sistemine oranla daha yüksek kurutma indeksine sahiptir. Tasarlanan kurutma sistemi ile fanlı kurutma sistemi karşılaştırıldığında ise ikinci programda tasarlanan sistemin, birinci ve üçüncü programlarda ise fanlı kurutma sisteminin kurutma indeksi yüksektir.

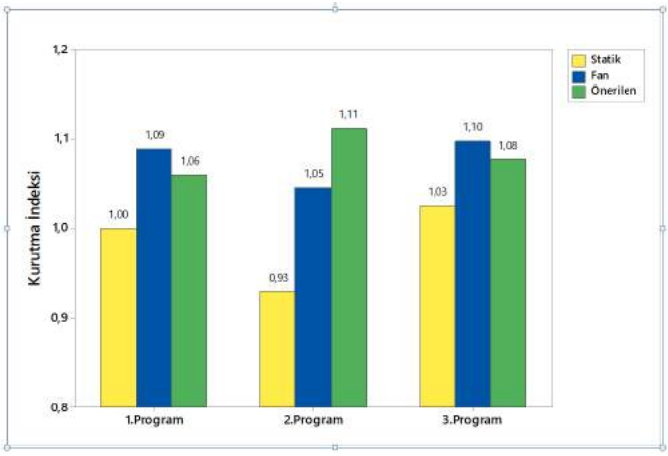

Şekil 13. Standart Koşullarda Karşılaştırmalı Kurutma Verimleri

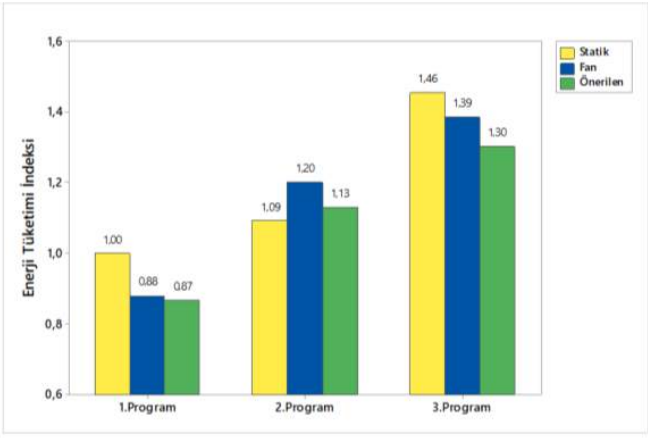

Şekil 14. Standart Koşullarda Karşılaştırmalı Enerji Tüketimleri

Fanlı ve tasarlanan doğal taşınımlı kurutma sistemi enerji tüketimleri karşılaştırıldığında; tasarlanan sistem, tüm programlarda fanlı sistemden daha az enerji tüketir. Birinci ve üçüncü programlarda statik kurutma sistemi ise en çok enerji harcayan programdır. Bu durumun sebebi statik sistemde durulama sıcaklığının yüksek olmasıdır. İkinci programda ise statik sistemin enerji tüketiminin düşük olmasının nedeni ise program süresinin statik kurutmanın gerçekleşmesi için gerekli sürenin altında olmasıdır. Bu programda kurutma tam anlamıyla gerçekleşmediği için enerji tüketimi de düşük olmaktadır. Bu programda son durulama sıcaklığının artırılması ve program süresinin uzatılmasıyla, istenilen kurutma performansı elde edilebilir. Ancak bu yapılırsa enerji tüketimi artacaktır.

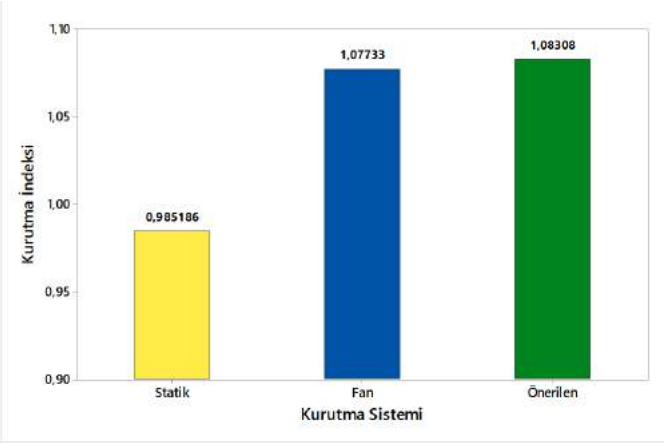

Şekil 15. Ortalama Kurutma İndeksi

Karşılaştırmanın yapıldığı üç yıkama programının ortalama kurutma indekslerine ait grafik Şekil 15'te verilmiştir. Grafikte de görüldüğü üzere tasarlanan sistem ve fanlı sistemin kurutma skorları birbirine çok yakındır. Statik sistemin ise kurutma skoru diğer iki sistemden düşüktür.

Benzer şekilde karşılaştırmanın yapıldığı üç yıkama programının ortalama enerji indekslerine ait grafik ise Şekil 16'da verilmiştir. Grafikte de görüldüğü üzere, tasarlanan sistem ortalama enerji tüketimi en düşük kurutma sistemidir. En çok enerji tüketen sistem ise statik kurutmadır.

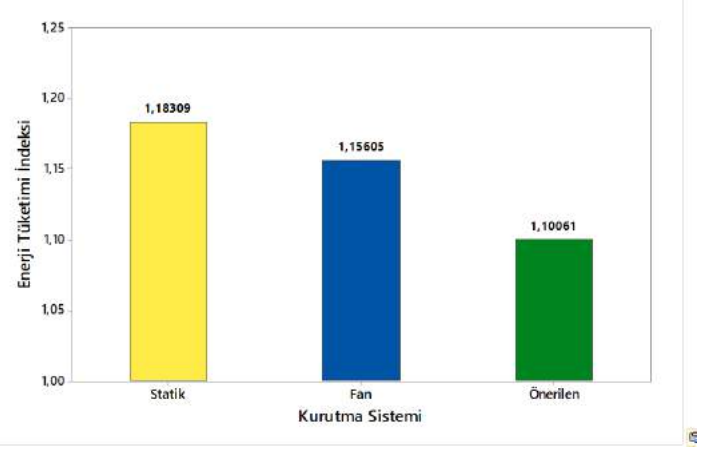

Şekil 16. Ortalama Enerji Tüketimi İndeksi

Özet olarak standart koşullarda sistemlerin performansları karşılaştırıldığında;

- Statik kurutma tüm programlarda en düşük kurutma performansına sahiptir.
- Fanlı kurutma sistemi birinci ve üçüncü yıkama programlarında en yüksek performansı göstermiştir.
- Tasarlanan kurutma sistemi, ikinci programda en yüksek performansı göstermiştir.
- Enerji tüketimleri birinci ve üçüncü programlarda statik – fanlı – tasarlanan sistem şeklinde azalarak sıralanmaktadır.
- İkinci programda statik kurutma sistemi en az enerji tüketmektedir.

4. Sonuçlar ve Öneriler

Tasarlanan kurutma yönteminde doğal bir hava akış yolu oluşturularak kurutma adımında nemli havanın kabin içinden atılması sağlanmaktadır. Nemli hava bir yoğuşma kanalı vasıtasıyla atılırken kabin içine taze hava alınabilmesi amacıyla bir emme kanalı sisteme eklenmiştir.

Kurutma kanallarının bağlantısı için makinede oluşturulan açıklıkların kesit alanı ve konumu, sistemden geçecek debi değerini doğrudan etkileyen değişkendir. Bunun yanı sıra kanalların geometrisi ve basınç düşümü de debiyi etkileyen diğer değişkenlerdir.

Kurutma sistemleri, sıcaklık ve nem farkı ile tetiklenmektedir. Kurutma adımının başında nem atma hızı yüksekken, kurutma adımı sonuna doğru kabin içiyle bulaşık makinesi ortamı arasındaki sıcaklık ve nem farkı azaldığı için nem atma hızı düşmektedir.

Programdan bağımsız olarak ortalama performanslar karşılaştırıldığında, tasarlanan yeni kurutma sisteminin kurutma etkinliği, statik kurutma sistemine göre %9,9 daha yüksek iken fanlı kurutma sistemi ile benzerdir.

Benzer şekilde ortalama enerji tüketimi de programdan bağımsız olarak değerlendirildiğinde, tasarlanan yeni kurutma sistemi en az enerji tüketirken, fanlı sistem %5 daha fazla enerji tüketmektedir. En çok enerji tüketen statik sistemin ise tasarlanan sistemden %7,5 daha fazla enerji tükettiği gözlemlenmiştir.

Yıkama programları özelinde değerlendirildiğinde, tasarlanan kurutma sistemi, standart koşullarda yapılan testlerde tüm yıkama programlarında statik kurutma sistemine oranla daha yüksek kurutma skoruna (Birinci program %6, ikinci program %19,4, üçüncü program %11,2) sahiptir. Diğer taraftan, statik kurutma, tüm programlarda en düşük kurutma performansı göstermiştir.

Birinci ve üçüncü programlarda ise fanlı kurutma sisteminin kurutma skoru daha yüksektir (Birinci program %2,8, üçüncü program %1,8).

Tasarlanan sistemin kurutma skoru, ikinci programda fanlı sistemden %5,7 fazladır.

EN 60436 standardına göre, kurutma performansının değerlendirilmesi program bitiminden 30 dakika sonra yapılır. Tasarlanan sisteminin en büyük üstünlüğü, barındırdığı atmosfer açıklıkları nedeniyle denge noktasına gelene kadar kurutma işleminin kendiliğinden sürmesidir. Bu nedenle fanlı kurutma sistemine göre yaklaşık 30 dakika fazladan kurutma işlemi yapabilmektedir. Tasarlanan kurutma sisteminin veriminin ikinci programda fanlı sistemden daha üstün olmasının nedeni budur.

Fanlı ve tasarlanan sistemin enerji tüketimleri karşılaştırıldığında ise tasarlanan sistem, tüm programlarda fanlı sistemden daha az enerji tüketmektedir.

Bu çalışmada araştırma ve yayın etiğine uyulmuştur.

Teşekkür

Bu çalışma, Konya Teknik Üniversitesi "Kamu-Üniversite-Sanayi İş Birliği ile Öğrenci Kabulü" programı kapsamında tamamlanan "Ev Tipi Bulaşık Makinelerinde Doğal Taşınım Prensibine Göre Çalışan Yeni Bir Kurutma Sisteminin Geliştirilmesi ve Kurutma Performansının Deneysel Olarak Araştırılması" başlıklı yüksek lisans tezinden üretilmiş ve Arçelik Bulaşık Makinesi işletmesi tarafından desteklenmiştir.

Kaynakça

Bengtsson, P. ve Berghel, J. (2017). Concept study of a new method for drying dishware in a heat pump dishwasher. *Energy Efficiency,* 10(6), 1529–1538. Doi: 10.1007/s12053-017-9541-4

Bengtsson, P., Berghel, J. ve Renström, R. (2015). A household dishwasher heated by a heat pump system using an energy storage unit with water as the heat source. *International Journal of Refrigeration,* 49, 19–27. https://doi.org/10.1016/j.ijrefrig.2014.10.012

BS EN 60436:2020+A11:2020, Electric dishwashers for household use, Methods for measuring the performance.

Jeong, S. W. ve Lee, D. H. (2014). Drying performance of a dishwasher with internal air circulation. *Korean Journal of Chemical Engineering,* 31(9), 1518–1521. Doi: 10.1007/s11814-014-0194-0

Karlsson, B. ve Quintiere, J. (1999). *Enclosure Fire Dynamics.* Boca Raton: CRC Press, 93–102.

Kumar, N., Rendall, J., Turnaoglu, T., Gluesenkamp, K. R., Patel, V. K., Abuheiba, A. Ve Gehl, A. (2021). *Measurements of Evaporation and Condensation Mass Transfer Resistances for Surfaces in Residential Dishwashers,* 18th Interna-

tional Refrigeration and Air Conditioning Conference, Purdue University, Indiana, USA.

Linden, P. F. (1999). The Fluid Mechanics of Natural Ventilation, *Annual Review of Fluid Mechanics,* 31 (1), 201–238. https://doi.org/10.1146/annurev.fluid.31.1.201

Mujumdar, A. S. (2006). *Handbook of industrial drying.* Boca Raton: CRC Press, 3rd edition.

Sai, P. S. T. ve Linga, A. (2010). *Studies on drying kinetics of solids in a rotary dryer,* 3rd International Conference on Thermal Issues in Emerging Technologies, Theory and Applications, Cairo, Egypt.

Mühendis ve Makina / Engineer and Machinery
https://dergipark.org.tr/tr/pub/muhendismakina

SEQUENCING MODEL FOR A SEAT BELT MANUFACTURER

Talha SATIR[1], Aleyna KARATAS[2], Yasemin GUVENDI FILIZ[3], Mohammed Mohanad Yawar SAYAN[4], Ilayda ULKU[5*]

[1] Industrial Engineering Department, Istanbul Kultur University, Istanbul, Turkey
ORCID No : http://orcid.org/ 0000-0002-1191-2764

[2] Industrial Engineering Department, Istanbul Kultur University, Istanbul, Turkey
ORCID No : http://orcid.org/ 0000-0003-3393-0653

[3] Industrial Engineering Department, Istanbul Kultur University, Istanbul, Turkey
ORCID No : http://orcid.org/ 0000-0001-6741-0539

[4] Industrial Engineering Department, Istanbul Kultur University, Istanbul, Turkey
ORCID No : http://orcid.org/ 0000-0003-0174-3570

[5] Industrial Engineering Department, Istanbul Kultur University, Istanbul, Turkey
ORCID No : http://orcid.org/0000-0003-0464-7007

Keywords

Sequence and scheduling, assembly line, unfinished works, ERP (enterprise resource planning), APP (aggregate production planning)

Abstract

The study focuses on optimizing the production process of a Turkish family company specializing in seat belt manufacturing, boasting an annual capacity of 810,000 units and employing 150 individuals. Serving major clients such as Otokar, Ford Otosan, Bmc, Karsan, Anadolu Isuzu, Mercedes, Man, Temsa, and Türk Traktör, the company utilizes pressing, plastic injection, and assembly lines in its production. With a specific emphasis on the sequencing and scheduling of the assembly lines, a mathematical model was formulated and solved using GAMS software. Comparative analysis, incorporating scenario assessments, revealed that the proposed model significantly enhanced efficiency compared to various scenario outcomes.

* i.karabulut@iku.edu.tr
doi : 10.46399/muhendismakina.1364669

BİR EMNİYET KEMERİ ÜRETİCİSİ İÇİN SIRALAMA MODELİ

Anahtar Kelimeler

Sıra ve çizelgeleme, montaj hattı, tamamlanmamış işler, KKP (kurumsal kaynak planlama), APP (toplam üretim planlama)

Öz

Ticari araç sektörüne yönelik emniyet kemeri ve yedek parça üretimi gerçekleştiren, yılda 810.000 emniyet kemeri üretebilen aile şirketi, müşterileri arasında Otokar, Ford Otosan, Bmc, Anadolu Isuzu, Mercedes, Man, Temsa, Türk Traktör gibi önemli markaları bulundurmaktadır. Firmanın üretim kapasitesi, pres, plastik enjeksiyon ve montaj hatlarından oluşmaktadır. Şirketin üretimini geliştirmek amacıyla emniyet kemeri montaj hatlarının sıralanması ve programlanmasını ele almaktadır.

Şirketin 3 adet emniyet kemeri montaj hattı bulunmaktadır. Sıralama ve çizelgeleme sorununu çözmek için matematiksel bir model geliştirilmiş ve model GAMS yazılımı kullanılarak çözülmüştür. Çalışmanın sonuçları, GAMS modelindeki tamamlanmamış senaryo analizlerinin karşılaştırmasıdır. Önerilen modelin sonuçları, farklı senaryo analizlerine dayalı sonuçlarla kıyaslandığında, önerilen modelin daha etkili sonuçlar elde ettiğini göstermektedir.

Araştırma Makalesi
Başvuru Tarihi : 29.01.2024
Kabul Tarihi : 15.03.2024

Research Article
Submission Date : 29.01.2024
Accepted Date : 15.03.2024

1. Introduction

Seat belt is a valuable product in the automotive industry to protect the lives of passengers and vehicle users and to prevent accidents. Gustave Liebau is invented in 1903. In the 1930s, an American physician placed two-point seat belts in his car and insisted that car manufacturers put them on new models. Over time, seat belt technology, product features, and diversity have evolved. The automobile industry is a constantly evolving industry. Pedestrian and passenger safety in particular comes to the forefront for automobile manufacturers.

Seat Belt manufacturer Ark Pres, which is the subject of study, started production with the Static Seat Belts in 1973 and short time started to supply seat belts to one of the national automotive giants, Tofaş for the Kartal vehicle model and Dogan vehicle model. With that, it reached an important position in the sector in 1981. The company has various products such as 2-point, 3-point, 4-point, and 5-point, and sub-products of these products. The company within the developments in our age, the company can compete with its competitors in the sector with a minimum focus on the cost of production.

In production and operations management, dispatching rules are decision rules that specify the sequence in which jobs or tasks are completed in a manufacturing or service setting. These guidelines are essential for organizing and allocating work in a way that maximizes a system's overall effectiveness and performance. Often, the main goal of dispatching rules is to reduce performance indicators such as makespan and overall completion time (Salama, Kaihara, Fujii, & Kokuryo, 2023).

The Parallel Machines and Flow Workshop problem type is the focus of the study. To improve the company's production efficiency, APP (Total Production Planning) and MRP (Material Requirements Planning) studies were used in the SAS (Sorting and Scheduling) research. The investigation's goal is to locate incomplete work.

The work with the Smallest Processing Time (SPT) or Expected Processing Time is processed first out of all the tasks that are processed. Linear programming (LP) is used to give fresh evidence of the correctness of SPT. The LP formulation was one that Wolsey and Balas had first introduced and improved (Cheng, Tang, & Zhang, 2023). According to the work presented by Qi, the SPT schedule is optimal for the interstation problem; The main problem is to minimize the sum of all job times completed at a single station and apply the SPT rule to obtain an optimal schedule. That is, all jobs are listed in non-decreasing order. Inter-station operations and idle periods between these operations are not allowed (Qi, Bard, & Yu, 2006).

Total flow time, or the amount of time it takes for a work to go through the complete production process, may be reduced with the use of SPT. By finishing shorter work sooner and enabling a faster resource turnover, it often optimizes the use of available resources. The Shortest Processing Time (SPT) rule offers an optimal solution to the problem of scheduling jobs on the same parallel machines to reduce average work completion times, which is one of the first achievements in scheduling theory. SPT offers a predictable planning sequence that facilitates the planning and management of manufacturing operations (Kim & Jeong, 2007). In addition to this facilitation, it is necessary to mention its limitations.

Even while SPT is good at cutting down on processing times for certain projects, it can make jobs wait longer and even lengthen lead times overall. When it comes to lowering completion time or other planning criteria like total completion time, it can not necessarily produce the best overall performance (Cho, Shmoys, & Henderson, 2023).

The job with the most processing or the largest possible processing time is processed first. In parallel scheduling of stations, it cannot generally be assumed that all stations are present along the schedule. Some stations are linked to unfinished work from the previous planning period, some are scheduled for correction, and some may be linked to specific work that must be done. In detail, it analyzes how the worst-case performance of the longest runtime first algorithm (or LPT for short) is affected by varying degrees of station availability (Hwang, Lee, & Chang, 2005).

It is generally not possible to assume that every machine will be accessible for use for the whole planning horizon in real-world parallel machine planning. A specific set of work that has to be done may partially occupy certain machines, some may be scheduled for repair or maintenance within a specific time frame, and some may be occupied by incomplete work from the previous planning period. It is scheduled at specific intervals because of a number of unavoidable factors. Given the restricted number of machines available, the scheduling problem's combinatorial character is undoubtedly made more difficult. Like all rules, the LPT rule has its limitations (Liao, Shyur, & Lin, 2005). Some studies contend that by minimizing the delay of individual jobs, LPT can result in longer flow times for the entire job group and potentially increase overall completion time. Lee contends that LPT can provide a program with an arbitrarily large runtime if all machines are shut down together for an arbitrarily long period of time (Zhao, Ji, & Tang, 2011). Furthermore, in terms of reducing other planning criteria like completion time or total completion time, LPT might not necessarily offer the greatest overall results.

In production and operations management, the Earliest Due Date (EDD) dis-

patching rule is used to schedule jobs or activities in a manufacturing or service setting. The idea of EDD is to arrange tasks according to their due dates. In particular, the earliest-due jobs are scheduled first (Bryant, Lakner, & Pinedo, 2022). By finishing the projects with earlier due dates first, EDD aims to reduce overall tardiness or lateness of jobs (Lushchakova, 2006). The due date is taken into account for each work, and the jobs are arranged in ascending order of their due dates. Jobs that have the earliest deadlines are booked ahead of those that have later deadlines. Even while the restrictions have their uses, they might not always result in the best overall performance when it comes to lowering other scheduling criteria like makespan or total completion time (Jiang, Lee, & Michael, 2021).

The order is made first as it is the milestone with the earliest delivery date in the project phase. To create a timed work queue in a three-station production area, this method must be considered to maximize total early work due to the same delivery day. Early completion of a job is a parameter defined as the total amount of work done before the time requested by the customer. This work mainly focuses on the unweighted model and proposes a dynamic programming approach that works in "O" time. This is studied by an approximation method where it has been shown that the Earliest Due Date (EDD) algorithm, best known in factory planning, can achieve only the most erroneous performance ratio for propagation optimal minimization problems. With the motivation to suggest better approximation algorithms. Finally, it is noted that the approximation results also work for the weighted model if a certain constraint is met (Chen, Miao, Lin, Sterna, & Blazewicz, 2022).

The first job to the station is done first. When the customer order reaches the seat belt assembly line, a production plan is taken according to the order of the order, and the "first come, first served" principle is kept in the foreground to manage the service requests in the name of equality. Most CSS studies do not directly model shared seat belt supply-demand interactions, especially when demand shortages arise. This work formulates the supply-demand dynamics of one-way CSS under different First Come First Serve (FCFS) mechanisms and puts them in the constrained rational dynamic user equilibrium (BR-DUE) problem. Two separate FCFS mechanisms have been proposed to improve the use of shared seat belts given the same CSS resources at the split time. To accurately capture CSS selection in space and time, a path-expansion strategy has been proposed to deal with different wait times under separate FCFS mechanisms. Numerical examples show that FCFS mechanisms have a significant impact on supply-demand dynamics and CSS selection (Wang & Liao, 2021).

One of the most basic scheduling principles is FCFS, which processes jobs in the order that they arrive. Reducing the lead time or waiting period for each task is the main objective. Jobs are booked according to the times of arrival. The first

work that arrives gets handled first, and then the second task in the sequence of arrival. FCFS is simple to use and appropriate in situations where business priorities are not crucial or if arrival order is the only factor to be taken into account (Jia, Bard, Chacon, & Stuber, 2015).

One of its limitations is that FCFS might not be the best option for overall system performance. It doesn't account for work deadlines or processing times, which might result in wasteful use of resources or longer flow times (Winograd & Kumar, 1996).

While investigating APP and MRP concerns, it is determined that SAS issues are critical in production and assembly lines. Today, most of the goods we use to make our lives simpler are constructed. These things are sub-items that are sequentially merged to make the main product. The assembly line is the manufacturing mechanism utilized to create these items. This manufacturing system is made up of several workstations that are organized along with the material handling system. A series of jobs direct workers or robots to handle components at each workstation. Tasks are delegated to a predefined group of workstations depending on their priority relationship. To achieve acceptable productivity, the total cycle time per workstation and processing time of assemblies should not exceed. The ALB (assembly line balance) problem refers to the priority connections between activities. These challenges address the issue of distributing jobs to workstations to achieve a specified goal, such as decreasing cycle time for a given number of workstations or optimizing assembly line efficiency (Becker & Scholl, 2006). On the other hand, Abdelsalam et al. developed a mixed integer programming model. They solved it with GAMS by considering several scenarios to determine the current system's idle time and unused machine capacities. With the developed model, they mentioned that the proposed model maximizes the company's efficiency (Abdelsalam, et al., 2023).

A Gant Chart is created using assumptions such as the steps to be followed to solve the problem, arrival time, process time, and cycle time. A mathematical model is established, and a scenario analysis is made.

The rest of this study is structured as follows: Section 2 the proposed methodology of the problem is defined. In Section 3, the implementation and the numerical results are discussed. The conclusion of the proposed method is presented in Section 4.

GAMS and scenario analysis in the study. The Gantt Chart drawing shows the production cycle of the assembly line and the duration of the unfinished works, the estimation, and the estimation of the bottleneck situation for 3 assembly lines in the company. Transition times from all processed stations are observed at 174, 183, and 170 seconds. The most efficient method for line 1 in scenario analysis;

is time to completion: 6.5, Usage Capacity: 6.45%, average number of jobs completed in the system: 3.2, number of jobs delayed: 0.41, and FCFS method. The most efficient method in line 2; Completion time with EDD method: 12.5, Usage capacity: 38.67%, average number of completed jobs in the system: 2.58, number of delayed jobs: 4.5. on the 3rd line;

Average completion time: 16, Usage Capacity: 37.37, the average number of completed jobs: 2.67, and the number of delayed jobs: 7.5, the most efficient method is the SPT method.

2. Methodology

In this part of the study, methodology, data collection, analysis method, and flow chart of mathematical models are created. To overcome these challenges, are created a linear programming paradigm. SAS is a significant instrument in the management of production and operations. In everyday life, decision-makers are eager to discover an excellent strategy to properly manage resources to provide the most actual for the industrial and service industries. Scheduling is a timeline that comprises the start and finish timings of machine jobs, among other things. Machines are commonly used to refer to resources, whereas jobs or operations refer to tasks. The store is the setting for the scheduling problem. There are several sorts of shops utilized in scheduling difficulties, such as the job shop, mixed shop, flow shop, open shop, and so on. This paper describes the various methods to solve the SAS problem. Various works have been formulated to obtain the optimal solution in the field of scheduling problems. There are two different significant characteristics of other solution methods. The first characteristic is the quality of the solution, and the second characteristic is the computation time involved. This study classified these methods into the dispatching rules. Research and publication ethics were complied with in this study.

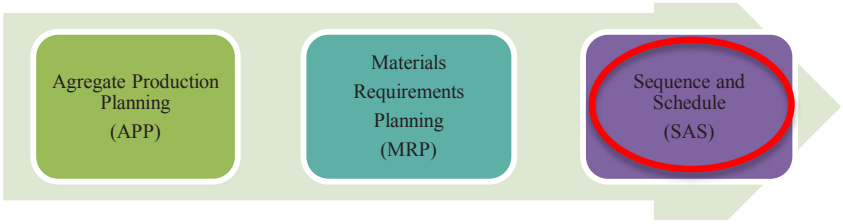

Figure 1. Production Planning and Control Relationship

In the Figure 1, orders from customers are gathered together by making an APP. All collected data is transferred to the relevant departments via MRP in order to prevent data loss and ensure correct information flow. The production, planning, supply, and related departments that receive this data initiate the necessary

studies in order to realize production in a shorter and more efficient manner by making SAS.

2.1 Flow Chart of The Methodology

In Figure 2, a flow chart about the efficient capacity planning study process has been created. There is a need for some data about the Company in question.

These; machines used, machine capacities, production times and costs, setup time, customer order delivery date, order quantity, cycle process, transaction process, current stock, and other basic data. Thanks to the data obtained, past demands are analyzed, and production capacity is determined with ERP. An optimal result is obtained thanks to the linear mathematical model. In the SAS methods used, 4 different methods are used, and GAMS software is preferred for the solution of this model and the solution is collected from here. Optimum production planning according to the solution is realized as the lowest cost and maximum profit. These strategies and outcomes are discussed in order to expand the capability of the company.

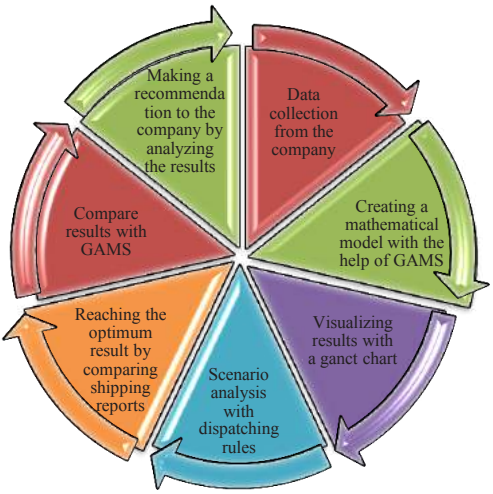

Figure 2. Proposed Methodology

In the Figure 2, the steps to be taken to achieve the optimal result are visually enriched. First, the data obtained from the company is collected. In order to attain the best possible outcome, a mixed integer programming model is constructed by sorting the workloads. After all the data are considered, a Gantt chart is created and at the end, a comparison is made by making a scenario analysis and a recommendation can be made to the company.

2.2 Data Collection and Analysis Methods

In this section, SAS analyses are made with the data taken from Ark Pres. First, the company's own planning method is observed. For example, in the weekly customer order, the production planning is determined according to the order dates. 4 strategies for this study are SPT, FCFS, EDD, and SLC. Details of the production process of the selected products are given below.

2.1.1 3 Point Seat Belt

This type of seat belt consists of 20 sub-products. There are 3 different types of this product in itself. The differences between these products are the variety of mechanisms. These products; Collector frame, Shaft, Rabbit, mainspring spring, Plastic cover, screw, Plastic gear, Angle element, plastic pin, triangle buckle, T-buckle, Bottom link bracket, Label, Sewing thread, plastic stopper, plastic cover with triangle buckle, Bolt, Isher, Belt, Plastic belt guide. It consists of 8 stations for the production of 3-point seat belts. Station 1 is 10 seconds, station 2 is 25 seconds, station 3 is 20 seconds, station 4 is 15 seconds, station 6 is 25 seconds, station 7 is 20 seconds, and station 8 is 22 seconds. In other words, a production process of around 2.50 is determined. A time loss of 6 seconds is determined between stations 1 and 2.

(a) (b) (c)

Figure 3. (a) 3Point AR3 Seat Belt (b) 3Point AR2 Seat Belt (c) 3Point All Age Seat Belt

In the Figure 3, different types of 3-point seat belts are added as a product image. The type (a) product mechanism has a newer and larger design, while the type (b) product has a smaller mechanism. Therefore, the belt wrapping feature of the (a) type product is higher than the (b) type product. Type (c) product is suitable for children's school bus/bus.

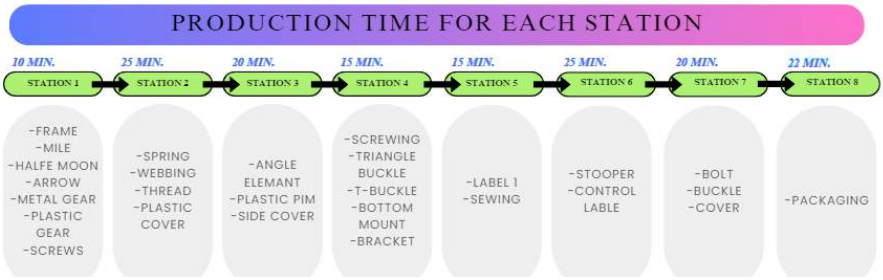

Figure 4. 3 Point Seat Belt Production Line

In the Figure 4 for visual to shows that the assembly line of the 3-point seat belt consists of 8 stations. There is a detailed explanation of the processing time of each station and the sub-product group assembled at this station. For a seat belt to become a product, it must complete these processes.

2.2.2 2 Point Seat Belt

This type of seat belt consists of 15 sub-products. There are 3 different types of this product in itself. The differences between these products are the variety of mechanisms. These products are collector frame, shaft, half-moon, mainspring, metal gear, plastic cover, screw, plastic gear, angle bracket, spring, label, plastic belt guide, bottom link bracket, plastic stopper, and belt. The construction of the 2-point seat belt consists of 7 stations. Station 1 lasts in 15 seconds, station 2 in 25 seconds, station 3 in 25 seconds, station 4 in 17 seconds, station 5 in 15 seconds, station 6 in 25 seconds, and station 7 in 14 seconds.

(a) (b) (c)

Figure 5. (a) 2Point ELR Seat Belt (b) 2Point Static Seat Belt (c) 2Point ALR Seat Belt

In the Figure 5 different types of 2-point seat belts are added as a product image. The technical feature of the (d) type product has a 3-point seat belt feature. Since it has a 2-point fastening feature, it is referred to as a 2-point seat belt. (e) type product does not have a mechanism. The fixation provision of this belt is also seen in the image. The product mechanism in the image (f) is different from all

other seat belt mechanisms. The belt does not have a rewind mechanism feature.

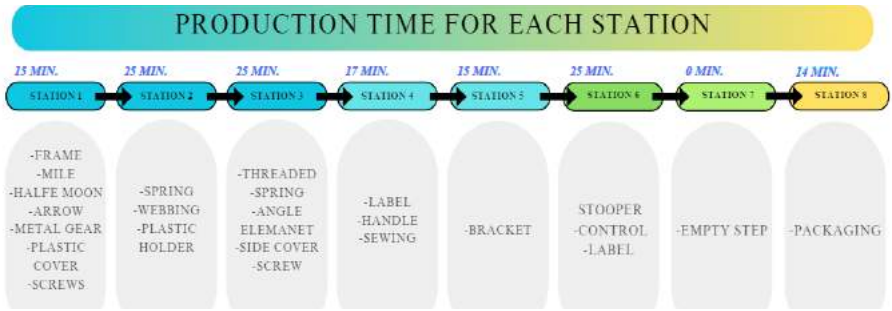

Figure 6. 2 Point Seat Belt Production Line

In the Figure 6 depicts the production process for the 2-point seat belt, which has 7 stations. In the image above, station 7 is an empty step, that is, a station that is not used in the 2-point seat belt assembly process. There is a detailed explanation of the processing time of each station and the sub-product group assembled at this station. For a seat belt to become a product, it must complete these processes.

2.3 Mathematical Modelling Approach

In this part of the study, there are the formulas of the constraints created from the sequence and scheduling perspective in order to calculate the objective function.

$$Min\ Z = \sum_{i=1}^{6} \sum_{i=1}^{6} U_{ij} \qquad \forall_{,j} \tag{1}$$

Equation 1 represents the objective function to minimize the time of unfinished work.

$$S_{ij} - A_{ij} \geq 0 \qquad \forall_{,j} \tag{2}$$

Equation 2 presents the processing of a model cannot start before the model arrives at the station.

$$S_{ij} - T_{ij} \geq -M * (2 - x(i,k) - x(1,k-1)) \qquad \forall_{,j} \tag{3}$$

Equation 3 symbolizes the starting time of a model art a station cannot be less than the finishing time of the model before itself.

$$T_{ij} - A_{ij} \geq c_{ij} \qquad \forall, j \qquad (4)$$

Equation 4 imitates a job must be finished at the station in a cycle time after its arrival.

$$T_{ij} \geq S_{ij} + P_{ij} \qquad \forall, j \qquad (5)$$

Equation 5 exemplifies the finishing time of a job is less than or equal to the sum of its starting time and its processing time.

$$U_{ij} \geq S_{ij} + P_{ij} - T_{ij} \qquad \forall, j \qquad (6)$$

Equation 6 represents the equation of unfinished jobs.

$$\sum_{i=1}^{6} X_{i,k} = 1 \qquad \forall, j \qquad (7)$$

Equation 7 describes every model should be assigned to a slot.

$$\sum_{k=1}^{6} X_{i,k} = 1 \qquad \forall, j \qquad (8)$$

Equation 8 presents a model that should be assigned to every slot.

This problem has been solved using the MIP model. Demand for production for use for products, available capacity per resource, worker-hour, machine-hour, raw material, production, inventory cost, and setup time data are used as parameters.

Data collecting is one of the basic elements of maintaining an effective, productive operation, as most industrial organizations will confirm. Having the capacity to analyze and manage production data may have a big influence on a company's ability to function and expand in a particular sector, and it can be the difference between flourishing and going out of business.

Cycle time is among the most important production KPIs. ERP and MES systems employ cycle time to schedule, buy, and budget manufacturing. While there are a plethora of metrics and KPIs to follow, Cycle Time is one of the most regularly evaluated in discrete manufacturing plants. Cycle time is the time it takes from the moment a produced Seat Belt gets started to the time it takes to get in the hands of our customers.

Cycle Time is the time a team works through the process before delivering the product. It is the amount of time required to execute a single job. This covers both the time spent making the item and the time spent waiting between active labor periods.

When calculating OEE (Overall Equipment Effectiveness), cycle time is also included. As a result, cycle time is the first to have a good full understanding of what a production activity is.

Scheduling and shipping rules are created to deal with uncertainty in the task process while monitoring the intended production in the mix. The facility's throughput is forecasted online, and the sequencing strategy is constantly altered as a result of the scheduling and dispatching rules.

In this study, it is tried to reach the optimal result by using the SAS method. In order to find the optimal order of the machines, a Gantt chart is created and commented on using GAMS software. In order to access this data, arrival time, process time, finishing time, and cycle time should be used. Therefore, the place of the cycle time here is very important.

2.4 Dispatching Rules

A dispatch rule is a rule that prioritizes all phases waiting to be processed on a station. The posting rule analyzes the jobs to be done and selects the job with the highest priority when the station is released.

Dispatching rules are called priority rules, scheduling rules, decision rules, or sequencing rules. These are the classical methods to solve scheduling problems based on the priority of jobs. Priority of jobs is defined as a function of shop characteristics, machine parameters, or job parameters. Generally, dispatching rules are applied without a proficient system. Therefore, for most scheduling problems, these rules do not have the guarantee to provide the optimum solution and are used as an initial sequence for improvement heuristics and metaheuristics methods.

Priority dispatching rules are the most often used scheduling strategy in job shops. The primary concept is to plan a work operation as quickly as feasible; if many productions waiting to be processed by the same station, schedule the one with the highest priority. A timetable and a Gantt Chart are simple to create. At the end of the day, this study aims to achieve the optimal timing by maintaining customer performance at its best level through shipment performance, average lead time, maximum lead time, average delay, maximum delay, number of delayed tasks, total and average preparation time performance data.

$$\text{Average Completion Time} = \frac{\text{Sum of total flow time}}{\text{Number of jobs}} \quad (9)$$

$$\text{Utilization Metric} = \frac{\text{Total job work(processing)}time}{\text{Sum of total flow time}} \quad (10)$$

$$\text{Average number of jobs in the system} = \frac{\text{Sum of total flow time}}{\text{Total job work time}} \quad (11)$$

$$\text{Average Job Lateness} = \frac{\text{Total late days}}{\text{Number of jobs}} \quad (12)$$

To calculate the average product assembly time in Equation (9), the total product flow time is divided by the number of stages. To calculate the current capacity utilization rate in Equation (10), the process time of the total jobs is divided by the total flow time. To calculate the average number of workflows on the assembly line in Equation (11), the total run time is divided by the total business process time. When calculating the average late work in Equation (12), the total number of days not completed is divided by the total number of jobs done.

Model Parameters Indicate

- i = 2PointAR3, 2PointALR, 2PointELR, 3PointH57, 3PointAR2, 3PointALLAGE
- j = Line 1, Line 2, Line 3
- k = Slot index 1, 2, 3, 4, 5, 6
- c = Cycle time
- at = Arrival time
- p = Process time

Model Variables

- z obj = minimizing the time of unfinished works
- X_{ik} = Arrival time of two consecutive models at a station
- A_{ij} = The arrival time of a pattern between two successive stations should be equal to the cycle time.
- S_{ij} = Processing of a model cannot begin until the model arrives at the station.
- T_{ij} = At a model station, the start time depends on the finish time of the previous jo

- U_{ij} = Cycle time in arrival

3. Implementation and Results

The GAMS output, cycle time, SPT, LPT, EDD, FCFS calculations, the numerical results, the comparison of performance measures, and a summary of rules are discussed. After the applied methods, the results obtained from GAMS are compared.

Table 1. GAMS Production Plan

Product \ Sequencing	1	2	3	4	5	6
2PointAR3						
2PointALR						
2PointELR						
3PointH57						
3PointALLAGE						
3PointAR2						

The analysis made in GAMS shows that; In order to produce 6 seat belts (models), the machines (assembly line) are assigned to the GAMS Production Plan in the Table 1.

Table 2. Cycle Time

Product Name	Line1	Line2	Line3
3PointALLAGE	26	38	34
3PointH57	32	30	28
2PointELR	31	29	33
2PointAR3	28	25	30
2PointALR	29	25	27
3PointAR2	28	23	31
Total Time	174	170	183

In the Table 2, there are cycle time details of 6 different seat belts for each assembly line.

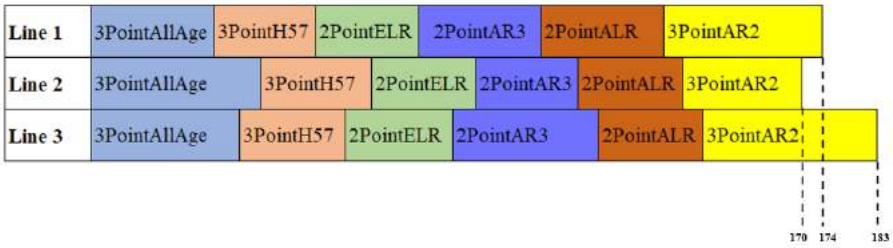

Figure 7. Gantt Chart From GAMS

Gantt chart assignments in the Figure 7 are made with GAMS software. According to the result of GAMS analysis, Line 2 makes the shortest and most efficient production.

Table 3. Gams Results For Unfinished Works

Product	Line 1	Line 2	Line 3
2PointAR3	109	104	111
2PointALR	100	96	99
2PointELR	112	109	107
3PointH57	139	136	131
3PointAR2	128	130	126
3PointALLAGE	125	123	125

A mathematical model is developed in GAMS using the processing time, arrival time, cycle time, and due date data obtained from the company. Unfinished works, which is the purpose of this study, are clearly expressed in the Table 3 above with the results from GAMS.

3.1 Numerical Result of Proposed Method

Results obtained by the proposed methodology are depicted Tables 5, 6, 7, 8, 9, 10, 11, and 12.

3.1.1 Numerical Result of SPT

The SPT sequencing rule is that the job is completed first in the shortest time to process. The SPT Rule is the method of ordering the assembly process time of the product from the shortest to the longest. The product process calculation solved by this method is as in Table 4 below.

Line 1	2PointAR3	3PointALLAGE	2PointELR	2PointALR	3PointAR2	3PointH57
Line 2	3PointALLAGE	3PointH57	2PointELR	3PointAR2	2PointALR	2PointAR3
Line 3	3PointH57	2PointAR3	2PointALR	2PointELR	3PointALLAGE	3PointAR2

Figure 8. SPT Gant Chart

The diagram in the Figure 8 is product sequences listing the shortest processing and cycle times of the SPT method for Line 1, Line 2, and Line.

Table 4. SPT Calculation Table

	Line1	Line2	Line3
Average Comletition Time =	6,50	12,50	16,50
Utilization Metric =	%45	%39	%37
Average Number of in the System=	2,23	2,59	2,68
Average Job Lateness =	0,42	4,67	7,50

For Line 1, Line 2, Equation (9), (10), (11), (12). The results in the Table 4 are calculated. The job completion time is the shortest on Line 1 and the longest on Line 3. In general, In the Table 4 minimized results are obtained in Line 1.

3.1.2 Numerical Result of LPT

LPT assignment is a rule in timed duration theory that prioritizes timed assignment jobs (or tasks) over non-increasing processing times.

Line 1	2PointAR3	3PointAL-LAGE	2PointALR	2PointELR	3PointAR2	3Po-intH57
Line 2	3PointAL-LAGE	3PointH57	3PointAR2	2PointELR	2PointALR	2Poin-tAR3
Line 3	3PointH57	2PointAR3	2PointALR	2PointELR	3PointAL-LAGE	3Poin-tAR2

Figure 9. LPT Gant Chart

The diagram in the Figure 9 is product lines listing the longest processing and cycle times of the LPT method for Line 1, Line 2, and Line 3.

Table 5. LPT Calculation Table

	Line1	Line2	Line3
Average Comletition Time =	13,92	16,33	26,67
Utilization Metric =	%20	%30	%23
Average Number of in the System=	5,06	9,80	4,32
Average Job Lateness =	6,42	8,00	18,17

In the Table 5, the LPT schedule is calculated using Equation (9), (10), (11) and (12). According to the results, Line 1 gives the most optimal results compared to Line 2 and Line 3. Line 2 and Line 3, on the other hand, give more optimal results than Line 2 and Line 3 when compared to each other.

3.1.3 Numerical Result of EDD

The EDD assignment rule is: "Jobs are processed according to the due date, earliest due date first." Table 8 shows the Job, Processing time, Due Date, Flow Time, and Job Lateness.

Line 1	2PointAR3	3PointAL-LAGE	2PointALR	2PointELR	3PointAR2	3Po-intH57
Line 2	3PointAL-LAGE	3PointH57	3PointAR2	2PointELR	2PointALR	2Poin-tAR3
Line 3	3PointH57	2PointAR3	2PointALR	2PointELR	3PointAL-LAGE	3Poin-tAR2

Figure 10. EDD Gant Chart

Based on the diagram in Figure 10 customer demand date (due date) for Line 1, Line 2, and Line 3, the incoming orders are distributed to 3 lines, and the production flow is determined.

Table 6. EDD Calculation Table

	Line1	Line2	Line3
Average Comletition Time =	6,58	12,50	16,50
Utilization Metric =	%44	%39	%37
Average Number of in the System=	2,26	2,59	2,68
Average Job Lateness =	0,42	4,50	7,50

The EDD chart in the Table 6 is calculated using Equations (9), (10), (11) and (12). When the results are examined, Line 1 usage rate is more beneficial than

Line 2 and Line 3. The job completion time is observed in the most optimal Line 1.

3.1.4 Numerical Result of FCFS

The FCFS assignment rule is processing jobs in the order they arrive at a machine or job center. Job, working time, Deadline, Flow Time, and Job Delay are shown in Table 7.

Line 1	2PointALR	2PointAR3	2PointELR	3PointH57	3PointAR2	3PointALLAGE
Line 2	2PointALR	2PointAR3	2PointELR	3PointH57	3PointAR2	3PointALLAGE
Line 3	2PointALR	2PointAR3	2PointELR	3PointH57	3PointAR2	3PointALLAGE

Figure 11. FCFS Gant Chart

While creating the production order in Figure 11 the demands from the customer are distributed to Line 1, Line 2, and Line 3 lines according to the demand receipt date and flows are created. Production is planned by dividing the demands of the customer into 3 assembly lines.

Table 7. FCFS Calculation Table

	Line1	Line2	Line3
Average Comletition Time =	9,33	15,67	18,67
Utilization Metric =	%31	%30	%33
Average Number of in the System=	3,20	3,36	3,03
Average Job Lateness =	2,83	7,33	9,83

The FCFS chart in Table 7 is calculated using Equations (9), (10), (11) and (12). Calculations in this table are prioritized and calculated according to the order of work from the customer. Line 1 gives the best results, while Line 2 and Line 3 are close together.

3.2 Summary of Dispatching Rules

As requested, a comparison is made in Table 8 First to order, first served Between the existing assignment rule using FCFS basis and the other two SPT, earliest end date EDD, and LPT program operation rules. The focus of the comparison is the determination of the best sequencing rule for the manufacture of The company Seat belts. The following are the findings.

Table 8. Average Detail Calculation

Rule	Average Completion Time (days)	Utilization (%)	Average number of jobs in system	Average lateness (days)
FCFS	16.17	29.29%	3.49	8.06
SPT	11.83	40.30%	2.50	4.19
EDD	11.86	40.11%	2.51	4.14
LPT	18.97	24.56%	6.30	10.86

3.3 Comparison of Performance Measures

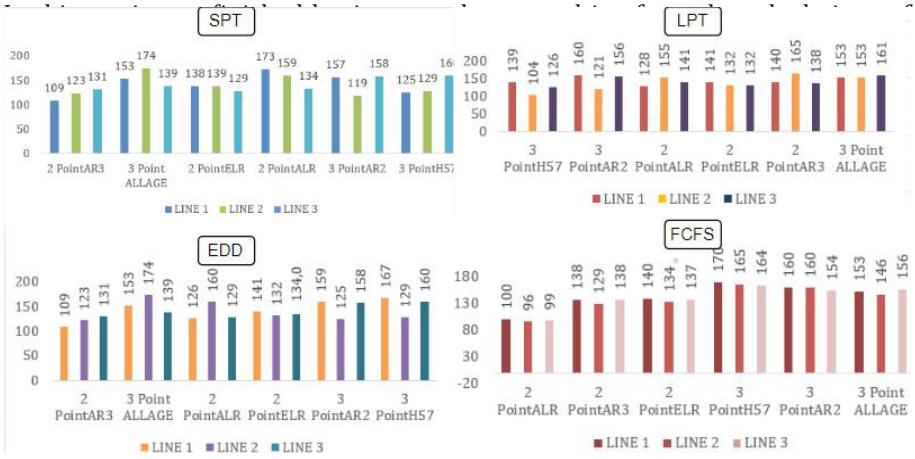

In the Table 9, unfinished works according to SPT, LPT, EDD, and FCFS rules in scenario analyzes are shown in detail. When the analyses are compared, the average of the incomplete works is the LPT ranking. The highest is the SPT method.

Table 10. Dispatching Rules Compares

		FCFS	SPT	EDD	LPT
Line1	Average Comletition Time	9,33	6,50	6,58	13,92
	Utilization Metric	0,31	0,45	0,44	0,20
	Average Number of in the System	3,20	2,23	2,26	5,06
	Average Job Lateness	2,83	0,42	0,42	6,42
Line2	Average Comletition Time	20,50	12,50	12,50	16,33
	Utilization Metric	0,24	0,39	0,39	0,30
	Average Number of in the System	4,24	2,59	2,59	9,80
	Average Job Lateness	11,50	4,67	4,50	8,00
Line3	Average Comletition Time	18,67	16,50	16,50	26,67
	Utilization Metric	0,33	0,37	0,37	0,23
	Average Number of in the System	3,03	2,68	2,68	4,32
	Average Job Lateness	9,83	7,50	7,50	18,17

In Table 10, the average completed time, station usage rate, average work time in the system, and average delayed work are calculated. Looking at the data obtained, Line1 provides a clear advantage over Line2 and Line3 in calculating the average delayed work in the FCFS Method. It has also been determined that Line 1 is approximately 30% more efficient than Line 2 and Line 3 in terms of the time completed in the FCFS Method.

Table 11. Compares Of Scenario Analysis and GAMS For Unfinished Works

EDD		GAMS
LINE 1		
2 PointAR3	109	109
3 Point ALLAGE	153	125
2 PointALR	126	100
2 PointELR	141	112
3 PointAR2	159	128
3 PointH57	167	139
SPT		GAMS
LINE 1		
2 PointAR3	109	109
3 Point ALLAGE	153	125
2 PointELR	138	112
2 PointALR	173	100
3 PointAR2	157	128
3 PointH57	125	139
LPT		GAMS
LINE 1		
3 PointH57	139	139
3 PointAR2	160	128
2 PointALR	128	100
2 PointELR	141	112
2 PointAR3	140	109
3 Point ALLAGE	153	125
FCFS		GAMS
LINE 1		
2 PointALR	100	100
2 PointAR3	109	100
2 PointELR	140	112
3 PointH57	170	139
3 PointAR2	160	128
3 Point ALLAGE	153	125

EDD		GAMS
LINE 2		
3 Point ALLAGE	123	123
3 PointH57	174	136
3 PointAR2	160	130
2 PointELR	132	109
2 PointALR	125	96
2 PointAR3	129	104
SPT		GAMS
LINE 2		
3 Point ALLAGE	123	123
3 PointH57	174	136
2 PointELR	139	109
3 PointAR2	159	130
2 PointALR	119	96
2 PointAR3	129	104
LPT		GAMS
LINE 2		
2 PointAR3	104	104
2 PointALR	121	96
3 PointAR2	155	130
2 PointELR	132	109
3 PointH57	165	136
3 Point ALLAGE	153	123
FCFS		GAMS
LINE 2		
2 PointALR	96	96
2 PointAR3	129	104
2 PointELR	134	109
3 PointH57	165	136
3 PointAR2	160	130
3 Point ALLAGE	146	123

EDD		GAMS
LINE 3		
3 PointH57	131	131
2 PointAR3	139	111
2 PointALR	129	99
2 PointELR	134	107
3 Point ALLAGE	158	125
3 PointAR2	160	126
SPT		GAMS
LINE 3		
3PointH57	131	131
2PointAR3	139	111
2PointALR	129	99
2PointELR	134	107
3PointALLAGE	158	125
3PointAR2	160	126
LPT		GAMS
LINE 3		
3 PointAR2	126	126
3 Point ALLAGE	156	125
2 PointELR	141	107
2 PointALR	132	99
2 PointAR3	138	111
3 PointH57	161	131
FCFS		GAMS
LINE 3		
2 PointALR	99	96
2 PointAR3	138	104
2 PointELR	137	109
3 PointH57	164	136
3 PointAR2	154	130
3 Point ALLAGE	156	123

Scenario analysis is calculated in Table 15 and applied according to the data obtained; Among the FCFS, SPT, EDD, and LPT methods, the most efficient is determined as the SPT Method for Line 1, EDD Method for Line 2, and SPT for Line

3. The data in this table represent unfinished works. When Table 14 and Table 15 are compared, it is observed that GAMS results are much more efficient than scenario analysis.

4. Conclusion

Maximum efficiency is tried to be obtained from the assembly line by using the GAMS program and FCFS, SPT, EDD, and LPT methods in the assembly line of Ark Pres company. There are 3 stations in the assembly line in the company. 7 workers for 2-point seat belts and 8 workers for 3-point seat belts work at these stations. As a result of the analysis, unfinished works and bottlenecks on the stations are determined. Necessary information is obtained from the company to find solutions to these problems. This information; cycle time, input time, manpower, customer demand, and production process at stations. First, is determined the cycle time of the products, the time of the entry of the products to the station, the installation time, and the unfinished works in the GAMS program. Then, the bottleneck rate in the company is determined by creating the Gantt chart diagram. In this way, the product order has been updated again to minimize the bottleneck in the stations. Incomplete works from the GAMS program are analyzed. The analyses made and the scenario analysis is made are compared. Scenario analysis is made according to the results of FCFS, SPT, EDD, and LPT methods. Methods are calculated according to customer demand. In the scenario analysis, it is observed that different methods are efficient in 3 stations. It has been analyzed that the SPT method is more efficient than other methods in terms of capacity utilization and completion time at Line 1 station. The minimum time loss in terms of the average delayed job in Line 2 is determined in the EDD method. In Line 3, the SPT and EDD methods are found to be the same and it is observed that these two methods are more efficient than FCFS and LPT methods in terms of average delayed work, capacity utilization, completed work, and average number of works in the system. The values found in the GAMS are compared with the values found in the methods. It has been observed that the values found in the GAMS of the average incomplete work process of the stations are better than the values found in the scenario analysis. As a result, in the study, a solution proposal is presented for the product ordering of the company's station use and the bottleneck problem resulting from this.

5. Conflict of Interest

No conflict of interest is declared by the authors.

References

Abdelsalam, N., Mohammoud, F., Eder, H., Abuyosef, A., Kaya, O., Kılıc, A. C., & Ulku,

I. (2023). A Production Line Assignment Problem For A Textile Industry. *Journal of Engineering Sciences and Design, 11*(1), 22-32. https://dergipark.org.tr/en/pub/jesd/issue/76248/1101063 adresinden alındı

Becker, C., & Scholl, A. (2006). A survey on problems and methods in generalized assembly line balancing. *European Journal of Operational Research,* 694-715. https://www.sciencedirect.com/science/article/abs/pii/S0377221704004801 adresinden alındı

Bryant, R., Lakner, P., & Pinedo, M. (2022). On the optimality of the earliest due date rule in stochastic scheduling and in queueing. *European Journal of Operational Research, 298*(1), 202-212. https://www.sciencedirect.com/science/article/abs/pii/S0377221721008158 adresinden alındı

Chen, X., Miao, Q., Lin, B. M., Sterna, M., & Blazewicz, J. (2022). Two-machine flow shop scheduling with a common due date to maximize total early work. *European Journal of Operational Research, 300*(2), 504-511. https://ideas.repec.org/a/eee/ejores/v300y2022i2p504-511.html adresinden alındı

Cheng, L., Tang, Q., & Zhang, L. (2023). Mathematical model and adaptive simulated annealing algorithm for mixed-model assembly job-shop scheduling with lot streaming. *Journal of Manufacturing Systems, 70,* 484-500.

Cho, W.-H., Shmoys, D., & Henderson, S. (2023). SPT optimality (mostly) via linear programming. *Operations Research Letters, 51*(1), 99-104. https://www.worldscientific.com/doi/abs/10.1142/S0217595923500409?download=true&journalCode=apjor adresinden alındı

Hwang, H.-C., Lee, K., & Chang, S. Y. (2005). The effect of machine availability on the worst-case performance of LPT. *Discrete Applied Mathematics, 148*(1), 49-61. https://www.sciencedirect.com/science/article/pii/S0166218X0400383X adresinden alındı

Jia, S., Bard, J. F., Chacon, R., & Stuber, J. (2015). Improving performance of dispatch rules for daily scheduling of assembly and test operations. *Computers & Industrial Engineering, 90,* 86-106. https://www.researchgate.net/publication/283097709_Improving_Performance_of_Dispatch_Rules_for_Daily_Scheduling_of_Assembly_Test_Operations adresinden alındı

Jiang, X., Lee, K., & M. L. (2021). Ideal schedules in parallel machine settings. *European Journal of Operational Research, 290*(2), 422-434. https://www.sciencedirect.com/science/article/abs/pii/S0377221720307013 adresinden alındı

Kim, S., & Jeong, B. (2007). Product sequencing problem in Mixed-Model Assembly Line to minimize unfinished works. *Computers & Industrial Engineer-*

ing, 53(2), 206-214. https://yonsei.elsevierpure.com/en/publications/product-sequencing-problem-in-mixed-model-assembly-line-to-minimi adresinden alındı

Liao, C.-J., Shyur, D.-L., & Lin, C.-H. (2005). Makespan minimization for two parallel machines with an availability constraint. *European Journal of Operational Research, 160*(2), 445-456. https://www.researchgate.net/publication/4871987_Makespan_minimization_for_two_parallel_machines_with_an_availability_constraint adresinden alındı

Lushchakova, I. N. (2006). Two machine preemptive scheduling problem with release dates, equal processing times and precedence constraints. *European Journal of Operational Research, 171*(1), 107-122. https://www.sciencedirect.com/science/article/abs/pii/S0377221704006174 adresinden alındı

Qi, X., Bard, J. F., & Yu, G. (2006). Disruption management for machine scheduling: The case of SPT schedules. *International Journal of Production Economics,* 103(1), 166-184. https://ideas.repec.org/a/eee/proeco/v103y2006i1p166-184.html adresinden alındı

Salama, S., Kaihara, T., Fujii, N., & Kokuryo, D. (2023). Dispatching Rules Selection Mechanism Using Support Vector Machine for Genetic Programming in Job Shop Scheduling. *IFAC-PapersOnLine, 56*(2), 7814-7819. https://www.sciencedirect.com/science/article/pii/S2405896323015525 adresinden alındı

Wang, D., & Liao, F. (2021). Analysis of first-come-first-served mechanisms in one-way car-sharing services. *Transportation Research Part B: Methodological,* 22-41. https://www.sciencedirect.com/science/article/pii/S0191261521000436 adresinden alındı

Winograd, G., & Kumar, P. (1996). The FCFS service discipline: Stable network topologies, bounds on traffic burstiness and delay, and control by regulators. *Mathematical and Computer Modelling, 23*(11-12), 115-129. https://www.sciencedirect.com/science/article/pii/S1474667016333511#! adresinden alındı

Zhao, C., Ji, M., & Tang, H. (2011). Parallel-machine scheduling with an availability constrain. *Computers & Industrial Engineering, 61*(3), 778-781. https://www.sciencedirect.com/science/article/abs/pii/S0360835211001343 adresinden alındı

Mühendis ve Makina / Engineer and Machinery
https://dergipark.org.tr/tr/pub/muhendismakina

OPTIMIZING RENEWABLE ENERGY INTEGRATION: A CASE STUDY OF STANDALONE PV-BATTERY SYSTEMS IN IZTECH CAMPUS

Beste RAMAZAN[1], Emin AÇIKKALP[2], Başar ÇAĞLAR[3*]

[1] Izmir Institute of Technology, Faculty of Engineering, Department of Energy Systems Engineering, Izmir, ORCID No : http://orcid.org/0000-0001-8622-3018

[2] Department of Mechanical Engineering, Faculty of Engineering, Eskisehir Technical University, Eskisehir, ORCID No : http://orcid.org/0000-0001-5356-1467

[2] Izmir Institute of Technology, Faculty of Engineering, Department of Energy Systems Engineering, Izmir, ORCID No : http://orcid.org/0000-0001-8732-6772

Keywords

University Campus, off-grid system, solar energy, photovoltaic panel, battery

Abstract

In this research paper the feasibility of renewable-powered, self-sufficient university campuses was explored by conducting a technoeconomic analysis of standalone PV-Battery systems for the buildings of Izmir Institute of Technology (IZTECH) in Izmir, Turkey. Given the high energy demand and dependence on fossil-based grids by universities, integrating renewables becomes important for minimizing carbon footprints. In this study the campus's solar potential was focused and the techno-economic feasibility of grid-independent operations provided by PV-battery systems was evaluated. Four scenarios were investigated: (i) maximum PV installation for each building (MPVB), (ii) maximum PV installation for the entire campus (MPVC), (iii) necessary PV installation for self-sufficiency of each building (NPVB), and (iv) necessary PV installation for self-sufficiency of the whole campus (NPVC). The first two scenarios considered the maximum achievable rooftop PV installation while the latter two included additional PV installation to cover all electricity needs. For all scenarios both lead-acid and Li-ion batteries were considered. Mathematical models were developed using PVSol and TRNSYS software, and technoeconomic analysis was conducted using Levelized Cost of Energy (LCOE) and Net Present Value (NPV) methods. It was found that the NPVC scenario with lead-acid batteries is the most favorable, as it minimizes battery utilization by enabling more PV installation and facilitating energy transfer between buildings. Additionally, the research showed that off-grid PV-battery systems are economically less feasible compared to on-grid counterparts, primarily due to the high cost of batteries.

* basarcaglar@iyte.edu.tr
doi : 10.46399/muhendismakina.1425616

YENİLENEBİLİR ENERJİ ENTEGRASYONUNUN OPTİMİZE EDİLMESİ: İYTE YERLEŞKESİNDEKİ BAĞIMSIZ PV-PİL SİSTEMLERİNE İLİŞKİN BİR ÖRNEK OLAY İNCELEMESİ

Anahtar Kelimeler

Üniversite Kampüsü, şebekeden bağımsız sistem, güneş enerjisi, fotovoltaik panel, pil

Öz

Bu araştırma makalesinde, İzmir, Türkiye'deki İzmir Yüksek Teknoloji Enstitüsü'nün (İYTE) binaları için bağımsız PV-Pil sistemlerinin teknoekonomik analizi yapılarak yenilenebilir enerjiyle çalışan, kendi kendine yeten üniversite kampüslerinin fizibilitesi araştırılmıştır. Yüksek enerji talebi ve üniversitelerin fosil bazlı şebekelere bağımlılığı göz önüne alındığında, yenilenebilir enerji kaynaklarının entegre edilmesi, karbon ayak izinin en aza indirilmesi açısından önem kazanmaktadır. Bu çalışmada kampüsün güneş enerjisi potansiyeline odaklanılmış ve PV-batarya sistemleri tarafından sağlanan şebekeden bağımsız operasyonların tekno-ekonomik fizibilitesi değerlendirilmiştir. Dört senaryo incelenmiştir: (i) her bina için maksimum PV kurulumu (MPVB), (ii) tüm kampüs için maksimum PV kurulumu (MPVC), (iii) her binanın kendi kendine yeterliliği için gerekli PV kurulumu (NPVB) ve (iv) tüm kampüsün kendi kendine yeterliliği (NPVC) için gerekli PV kurulumu. İlk iki senaryo, elde edilebilecek maksimum çatı üstü PV kurulumunu dikkate alırken, son iki senaryo, tüm elektrik ihtiyaçlarını karşılamak için ilave PV kurulumunu içeriyordu. Tüm senaryolar için hem kurşun-asit hem de Li-iyon piller dikkate alındı. PVSol ve TRNSYS yazılımları kullanılarak matematiksel modeller geliştirilmiş, Seviyelendirilmiş Enerji Maliyeti (LCOE) ve Net Bugünkü Değer (NPV) yöntemleri kullanılarak teknoekonomik analiz yapılmıştır. Kurşun-asit akülü NPVC senaryosunun, daha fazla PV kurulumuna olanak sağlayarak ve binalar arasında enerji transferini kolaylaştırarak akü kullanımını en aza indirdiği için en uygun senaryo olduğu bulunmuştur. Ek olarak araştırma, şebekeden bağımsız PV akü sistemlerinin, öncelikle akülerin yüksek maliyeti nedeniyle, şebekeye bağlı muadillerine kıyasla ekonomik olarak daha az uygulanabilir olduğunu göstermiştir.

Araştırma Makalesi
Başvuru Tarihi : 25.01.2024
Kabul Tarihi : 15.03.2024

Research Article
Submission Date : 25.01.2024
Accepted Date : 15.03.2024

1. Introduction

Energy generation and management is an essential topic for sustainable development, due to its close link with economic growth, environmental protection, and social balance of countries (Dursun, 2012; Oymen, 2020). The main challenge in the current energy infrastructure is the excessive utilization of fossil fuels, which creates environmental burden due to the global warming effect of fossil fuel-derived gas emission and leads to socioeconomic instability for countries with insufficient reserves. To overcome this challenge, there is an urgent call for the transition from fossil fuels to renewable energy sources. Turkey is a one of the countries, which heavily depend on imported fossil fuels. The transition from fossil fuels to renewable energy is essential for Turkey to decrease its the dependence on imported energy and the resulting economic burden. The total electricity generation of Turkey in 2020 is 306 TWh and the share of renewable energy sources in the total electricity generation is around 40% (TEİAŞ, 2020). Although the share of renewable is almost the same as the world average, the renewable energy generation of Turkey is still a way below its potential, suggesting that renewable energy resources have not been effectively used yet (TMMOB, 2023). To address this issue, the implementation of renewable technologies in different sectors should be accelerated.

Renewable energy technologies can be applied to different areas to meet energy demand, such as highly populated university campuses; shopping centers, restaurants, theatres, swimming pools, gyms, and recreational facilities (Dursun, 2012). In particular, the renewable energy integration into university campuses has received considerable attention due to the intention of making campuses sustainable and green. For a sustainable green campus several indicators have been proposed such as green campus layout and infrastructure, waste management, water management, and environmentally friendly transportation opportunities (Günerhan & Günerhan, 2016). Renewable energy resources with new practices for improving energy efficiency play a central role in covering these indicators (Sevilgen, 2008). To implement renewable energy technologies to university campuses, their technical and economic feasibilities need to be investigated, which has been addressed in literature several times. The related studies are summarized in the following parts.

Dursun (2012) investigated the feasibility of renewable energy systems containing photovoltaic array (PV) and fuel cell in comparison to diesel generator with and without grid connection for meeting the electricity need of Kirklareli University campus. In the fuel cell-containing system electrolyzers and hydrogen tanks were considered for energy storage during the mismatch between load and demand. Four different systems such as (i) stand-alone PV-diesel generator, (ii) grid connected PV, (iii) stand-alone PV-fuel cell, and (iv) grid connected PV-fuel cell

were analyzed by using HOMER software. Authors determined optimum configurations for each case and found that the grid-connected systems are more cost-effective compared to the systems without grid connection. They also determined that the grid-PV system has the lowest levelized cost of electricity (LCOE) (0.256 $/kWh) and net present cost (NPC) ($82,000). The grid-connected PV-fuel cell hybrid system was found to have a slightly higher cost (0.294$/kWh) compared to the grid-connected PV system even if it has a higher renewable fraction.

The technical and economic feasibility of the replacement of diesel generator by PV-based renewable systems was also investigated by Chedid, Sawwas, & Fares (2020) for meeting energy demand of the American University in Beirut. Different from the previous study, authors considered PV in combination with battery energy storage systems (BESS). A heuristic genetic algorithm and a rules-based dynamic programming approaches were used for system sizing and ensuring optimal power flow. The research shows that implementing the hybrid system results in a remarkably low operational cost, as it nearly eliminates the need for diesel generators and significantly reduces grid energy consumption during peak hours. The proposed PV-BESS system provided an average annual savings of $ 1,336 million, confirming the economic viability of the hybrid PV-BESS system compared to conventional diesel generators (DG). They reduced the overall COE of the system from 13.7 ¢/kWh to 8.8 ¢/kWh in the first year and from 14.4 ¢/kWh to 10 ¢/kWh in the 10th year. The feasibility of the PV-based renewable energy systems for university campus were also proved by other studies.

Wind turbine-containing renewable energy systems were also evaluated in terms of their energy generation potential and economic feasibility. Park & Kwon (2016) investigated the optimum energy system configuration by HOMER software for the Global Campus of Kyung-Hee University in South Korea. Authors evaluated 10 different energy system scenarios including PV, wind turbine, diesel generator, battery in on- and off-grid modes and found that on-grid scenarios are more feasible than off-grid scenarios. The simulation results show that the optimum energy system is the one containing PV, diesel generator and battery. NPC and COE values of the related system were calculated as 101,288,488 $ and 0.509 $/kWh, respectively. Authors determined that the hybrid PV-wind-battery system can be the renewable alternative of the related system with a very small increase in NPC and COE values (101,727,728$ and $0.511 $/kWh). Similar analysis was done by Khan et al. (2017) for a university campus in Abbottabad, Pakistan. Different from the previous one, they only consider off-grid systems and compare the economic performance of diesel generator and the hybrid PV-wind-battery systems. They found that the hybrid PV-wind-battery configuration has a significantly lower NPC (3,054,109$) and COE (0.258 $/kWh) values than diesel generator-based system.

Biomass including renewable energy systems are the other option to meet the energy demand of university campuses. The feasibility of the hybrid grid-connected Wind/PV/ Biomass power system from the techno-economic and environmental point of view was analyzed by Aykut & Terzi (2020) for Marmara University Goztepe campus. HOMER software was used for the sizing and optimization of renewable energy systems and a sensitivity analysis was performed for wind speed and solar radiation. According to the simulation results, the energy system with minimum NPC and COE was found as the grid-connected wind/ biomass hybrid energy system with the power utilization of 1,000-kW from the grid, 1,000 kW from the biomass generator, and 1,500 kW from the wind turbine. The NPC and LCOE values of the related system were determined as $5,612,501 and $0.067/kW, respectively. In another study conducted by Sava et al. (2017) biogas generator was considered in combination with PV and battery. Authors tried to determine the optimum standalone system configuration for the Bucharest "Regie" campus of Politehnica University and found that the optimum design is the hybrid system with a 50 kW PV module, a 50-kW converter, 1 kW storage batteries and a 110-kW biogas generator. The hybrid system generates approximately 60% of the energy from biomass, 25% of the energy from PV panels, and 15% from the grid. The proposed hybrid system has enabled cluster buildings to achieve a nearly zero building concept.

Fossil-fuel powered combined heat and power (CHP) along with renewable options was also considered in the literature for university campuses. Fernando, Gupta, Özveren, & Linn (2018) studied the optimum configuration of a hybrid power system including PV, wind, and CHP and its economic performance for the Abertay University Campus library building in Dundee Scotland. The best scenario was found to be the grid-connected hybrid system with 70 kW PV array including a converter and 500 kW CHP plant. NPC and COE values of the related system were calculated as 338,241 $ and 0.032 $/kWh, respectively. Authors also determined that the hybrid PV-wind-CHP system is not a feasible option due to high operation and maintenance costs.

The literature studies show that several on-grid and off-grid renewable energy systems were analyzed in terms of their technical and economic performance for meeting energy demand of university campuses. In some of them, non-renewable energy generation components were also included to observe the system economic performance comparatively. In almost all cases, grid-connected systems were found to be more economically feasible than off-grid systems due to the relatively high cost of energy storage systems. However, off-grid systems are still the attractive option for remote locations and for the areas suffering from grid instabilities and they are important to minimize the energy loss due to transmission and distribution. In addition, national grids mainly depend on fossil

fuel-sourced energy, which prevents on-grid systems from being sustainable and green. Since the IZTECH campus has suffered from regular power cuts and instabilities and a sustainable and green campus is desired, off-grid renewable energy systems were considered in the current study. This helps to evaluate the cost of energy for a self-sufficient campus and to develop improvement suggestions for future planning. Among renewable alternatives PV was selected as a power source for our off-grid system since PV seems to be the best option in terms of system economy due to their relatively low initial investment and operational and maintenance costs based the literature studies explained above. Considering the related literature studies, the novelty of this study is as follows:

(i) The PV-battery combination required for meeting energy needs of individual campus buildings and the whole campus were analyzed separately and the effect of energy transfer between buildings on the system economic performance was evaluated.

(ii) Two different battery options, namely lead acid and Li-ion batteries, were considered for detailed analysis of various off-grid scenarios.

(iii) The optimum system configuration depends on the locations, load profile and grid prices, which makes the technoeconomic analysis of a standalone energy system for the IZTECH campus a unique case, which was not studied before.

In this study, standalone PV-battery systems were designed to meet the electricity needs of the IZTECH campus buildings. Four different renewable energy scenarios were considered, and systems were modeled for each scenario by using PV*SOL and TRNSYS software. Based on the system size (e.g., number of units) and capacity, the economic performance of each scenario was also evaluated by LCOE and NPV analysis. The annual hourly electrical load was taken from the electricity supplier and the power output of PV modules was calculated based on the fixed tilt angle of modules by using real meteorological data for the campus location. The number of PV modules was determined to meet the annual electricity demand of the campus buildings while the capacity and number of batteries were determined in a way that the total accessible battery capacity covers the maximum cumulative energy deficiency in a year. This study contributes to determining PV-sourced energy generation capacity of each building and to understanding the importance of energetically interconnected buildings.

2. Description of Campus, Load Profile and Solar Potential

2.1 IZTECH Campus Layout and Building

Izmir Institute of Technology University (IZTECH) is in Izmir/Urla-Gulbahce re-

gion. Its coordinates are latitude 38° 19′ 13" N and longitude 26° 38′ 11" E (Fig.1). The total campus area is 132,000 . IZTECH consists of 3 faculties, one graduate school, one school of foreign languages and several administrative units. There are in total 30 buildings on the campus, which are listed in Table 1 with their total roof areas and type. The total roof area is not the usable area for PV installation due to the shading and blockage caused by other structures on the roofs (e.g., chimney outlets, column protrusions) depending on shapes and slopes of roofs. For this reason, suitable areas for installation were determined by using PV*SOL software and they are listed in Table 1. As seen from the Table 1, the total available area for PV installation is 23,199.

Figure 1. The satellite view of IZTECH Campus

Table 1. The total roof areas, the available roof areas for PV installation, and the roof types of IZTECH Campus Buildings

	Roof area (m^2)	**Suitable area for PV (m^2)**	**Roof Type**
General Culture Building	450.17	208.3	Flat
Recroate Building	456.69	278.6	Pitch
Head Of Department	1,315.97	753.1	Pitch
Faculty Of Science			
A Block	1,117.77	928.2	Pitch

B Block	1,172.97	1,045.70	Pitch
C Block	1,172.97	1,045.20	Pitch
Classroom Building	1,289.94	573.41	Flat
Physic Building	2,214.36	1,021.20	Flat
Mathematics Building	604.9	242.2	Flat
Biology Building	1,799.22	691.1	Flat
Foreign Language Building			
Foreign Language A Block	701.17	324.9	Flat
Foreign Language B Block	784.56	606.1	Flat
Administrate Building	1,118.65	633.8	Flat
Energy System Lab. Building	1,032.50	758.2	Pitch
Center Work	1,032.50	758.2	Pitch
Mechanical Engineering Building	2,162.34	1,005.60	Flat
Faculty of Architecture			
A Block	1,108.36	941.3	Pitch
B Block	1,278.94	1,072.70	Pitch
C Block	471.14	196	Flat
D Block	728.74	322.3	Pitch
E Block	1,141.09	628.6	Flat
Chemistry Eng. Building.	1,905.90	974.2	Flat
Computer Eng. Building	2,517.88	1,132.10	Flat
Library	2,211.49	1,049.50	Flat
Gym Center	2,775.29	1,354.80	Pitch
Pool	1,125.62	630.4	Flat
Café	1,653.16	606	Flat
Civil Engineering	5,206.74	400.2	Flat
Electric Electronic	2,185.84	1,124.20	Flat
Integrated Research Building	2,421.73	871.6	Flat
TOTAL	45,934	23,199	-

2.2 Load Profile

The electricity requirement of the campus is currently met by the grid, which also mostly covers the cooling and heating load. In this study, the electricity load of the whole campus was taken from the Electricity Distribution Company (Gediz Elektrik A.S.) for the year of 2019 on an hourly basis. This year was specifically chosen to exclude the effect of Corona breakdown. The hourly electricity load of the whole campus does not contain information about the share of each building in the total electricity consumption. Therefore, the hourly electricity consumption of each building was calculated by multiplying the fractional consumption of buildings (taken from the university based on the monthly data) with the hourly consumption of the whole campus. The monthly electricity consumption of the whole campus in 2019 is shown in Table 2 to indicate the change of electricity consumption throughout the year. As seen from the Table, the total electricity consumption of the campus is 5748.7 MWh and the lowest and highest electricity consumption were observed in January (623.3 MWh) and May (328.6 MWh), respectively.

Table 2. IZTECH Campus Monthly and Daily Average Electricity Consumption in 2019

IZTECH TOTAL	Total (MWh)	Daily Average (MWh)
January	623.3	8.37
February	495.5	7.37
March	535.4	7.19
April	457.7	6.35
May	328.6	4.41
June	513.1	7.12
July	562.9	7.56
August	464.4	6.10
September	437.1	6.07
October	366.6	4.92
November	399.0	5.54
December	565.1	7.59
TOTAL	5748.7	78.66

2.3 Solar Radiation

The solar radiation data of the IZTECH campus was taken from the PVGIS-SAR-

AH2 program. The solar data used in this study are hourly horizontal beam radiation ($G_{T,b}$), diffuse radiation ($G_{T,d}$) and ground reflected diffuse radiation ($G_{T,gnd}$). The monthly average values of these radiation along with total radiation incident on PV array (G_T) based on the optimum angle of incidence (See section 3.2) throughout the year are shown in Figure 2. As seen from the Figure the lowest and highest total radiation values incident on the PV array are 98.54 (kWh//mo), and 239.92 (kWh//mo), observed in December and July, respectively.

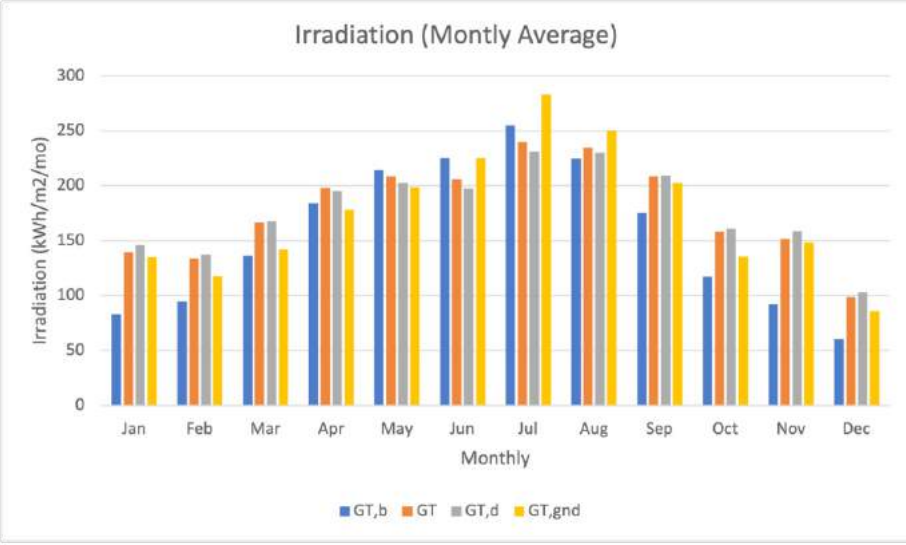

Figure 2. The Monthly Averaged Solar Radiations On The Campus

3. Modeling Approach

Four different PV-battery combinations were analyzed as standalone renewable energy systems for meeting electricity requirement of IZTECH campus buildings explained in Section 2.1. The investigated scenarios are (i) maximum PV panel installation for each building (MPVB), (ii) maximum PV panel installation for the whole campus (MPVC), (iii) necessary PV installation for each building (NPVB), and (iv) necessary PV installation for the whole campus (NPVC). For the first two scenarios (MPVB, MPVC) the maximum amount PV installation was determined based on the available roof area of each building while for the last two scenarios (NPVB, NPVC) additional PV installations on free land areas in the campus were considered to cover the total electricity demand of the campus building. In scenario 1 (MPVB) and scenario 3 (NPVB) each building in the campus was taken as a separate unit and the analysis was made based on no energy transfer between buildings. On the other hand, in the second (MPVC) and fourth (NPVC) scenarios

buildings were evaluated as interconnected so that the excess energy produced in one building can transfer to the other, which suffers from energy deficiency.

For all scenarios the components of these systems, namely the PV module, lead-acid battery, and inverter, were mathematically modeled and all system scenarios were analyzed dynamically in TRNSYS (Klein et al., 2018). The maximum allowable PV installation on the rooftop area of each building was determined by PV-Sol software while the number of batteries required was determined based on the maximum cumulative energy deficiency in a year, i.e., the total accessible battery capacity covers the whole energy deficiency in a year. To access the economic feasibility of the related systems, Levelized Cost of Energy (LCOE) and Net Present Value (NPV) methods were used. The approaches used for mathematical modelling of system components by TRNSYS and PV-Sol software and for the economic analysis were explained in the following sections.

3.1 TRNSYS Modeling

The considered standalone energy systems consist of photovoltaic panel, lead acid battery and regulator-inverter. The mathematical references of each unit are available in the TRNSYS software. The main expressions used to model the system were shown in the following parts.

3.1.1. Simple Photovoltaic System Modeling

For mathematical modelling of PV array Type 103 in TRNSYS software was used considering that the PV array operates at maximum power point condition. This model is based on the four-parameter equivalent circuit (John & Beckham, 1991) consisting of a direct current (DC) source, diode, and resistor (Figure 3). According to this model, the power of the PV array was calculated by the following equation (Klein et al., 2018):

$$P = \left[N_p I_L - N_p I_0 \left[exp\left(\frac{q}{\gamma k T_C}\left(\frac{V}{N_s} + \frac{I R_s}{N_p}\right) - 1\right)\right]\right] \times \left[\frac{\gamma k T_C}{q} ln\left(\frac{I_L + I_0 + I + N_p}{I_0}\right) - I R_s\right] \quad (1)$$

where N_p is the number of PV module in parallel, N_s is the number of PV module in series, q is electron charge (1.6x10-19 C), k is the Boltzman constant (1.38x10-23 J/K), γ is PV curve-fitting parameter, I is the module current, V is the module voltage, I_L is the module photocurrent and is the diode reverse saturation current.

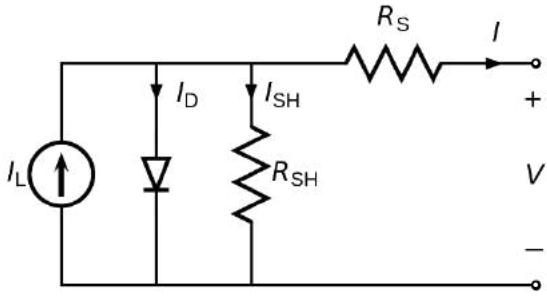

Figure 3. The Equivalent Circuit Of A Solar Cell *(John & Beckham, 1991)*

The I-V relation of the PV module changes with solar radiation and cell temperature. The photocurrent is affected by the solar radiation while the diode saturation current is influenced by the cell temperature. The photocurrent changes linearly with on the incident solar radiation as follows:

$$I_L = I_{L,ref} \frac{G_T}{G_{T,ref}} \tag{2}$$

where is the module photocurrent at the reference conditions (25°C, 1000 W/m^2), is incident radiation on the PV module, is incident radiation at reference conditions (1000 W/m^2). The incident radiation on the PV module was determined by the following formula:

$$G_{T,eff} = \tau\alpha_{normal}\left(G_{T,b}IAM_b + G_{T,d}IAM_d + G_{T,gnd}IAM_{gnd}\right) \tag{3}$$

where $\tau\alpha_{normal}$ is the transmittance-absorptance product at normal incidence (0.95), G_T and IAM are solar radiation and angle incidence modifiers for the beam, diffuse and ground reflected radiation. IAM values were calculated by using relation taken from King et al. (Keelialafreniere, 2018) as follows:

$$IAM = 1 - 1.1098x10^{-4}\theta - 6.267x10^{-6}\theta^2 + 6.583x10^{-7}\theta^3 - 1.427x10^{-8}\theta^4 \tag{4}$$

where θ is the angle of incidence, which was calculated as:

$$\theta = cos^{-1}\begin{bmatrix} sin\,\delta\,sin\,\phi\,cos\,\beta - sin\,\delta\,cos\,\phi\,sin\,\beta\,cos\,\gamma + cos\,\delta\,cos\,\phi\,cos\,\beta\,cos\,\omega \\ + cos\,\delta\,sin\,\phi\,sin\,\beta\,cos\,\gamma\,cos\,\omega + cos\,\delta\,sin\,\beta\,sin\,\gamma\,sin\,\omega \end{bmatrix} \tag{5}$$

where δ is the solar declination angle, ω is the hour angle, φ is the latitude and β is the slope of the module (the angle between the photovoltaic panel surface and the horizontal surface). The effective angle of incidence for diffuse and ground reflected radiation were calculated as:

$$\theta_{eff,d} = 59.567 - 9.123x10^{-2}\beta - 5.424x10^{-4}\beta^2 + 3.216x10^{-5}\beta^3 - 1.7x10^{-7}\beta^4 \quad (6)$$

$$\theta_{eff,gnd} = 90.032 - 6.615x10^{-1}\beta - 4.796x10^{-3}\beta^2 + 1.543x10^{-5}\beta^3 - 2.000x10^{-}\beta^4 \quad (7)$$

The cell temperature affects the power output of the PV module negatively. This effect was modelled by the following equation:

$$I_o = I_{o,ref} x (\frac{T_c}{T_{c,ref}})^3 \quad (8)$$

is the diode reverse saturation current at reference conditions, T_c is the module temperature and $T_{c,ref}$ is the module temperature at reference condition (25°C). The cell temperature depends on incident radiation (G_T), the ambient temperature (taken from climate data), the module efficiency (η_c), the transmittance-absorptance product ($\tau\alpha$), the normal operating cell temperature ($T_{c,NOCT}$), the ambient temperature ($T_{a,NOCT}$=20°C) and solar radiation ($G_{T',NOCT}$=800 W/m^2) at normal operating conditions.

In order to calculate the power output of a PV module by the four-parameter equivalent circuit model, the four module constants ($I_{L,ref}$, $I_{0,ref}$, R_s and γ) that cannot be determined by physical measurements were calculated by the Newton method based the open curcuit potential (V_{oc}), the short curcuit current (I_{sc}), the current at maximum power point (I_{mpp}), the voltage at maximum power point (V_{mpp}), temperature coefficient of I_{sc} and V_{oc} taken from manufacturer's technical sheets. In this study, Jinko Tiger Pro 525 Wp PV panel was selected, and the related parameters of the PV panel are listed in Table 3.

Table 3. Technical Parameters of the PV Panel (Jinko Tiger Pro 525 Wp)

Parameters	Values
V_{oc}	49.42 V
I_{sc}	13.63 A
V_{mpp}	40.80 V
I_{mpp}	12.87 A
α_{Isc}	0.032 A/K
α_{Voc}	-0.28 V/K

3.1.2 Simple Lead Acid Battery Modeling

For the modelling of lead acid battery Type47 module was used in TRNSYS software, which determines how the state of charge of the battery changes over time depending on the rate of charge or discharge. The model works based on the Shepherd formula (Keelialafreniere, 2018), which relates the battery current and voltage to battery state of charge. The I-V relation was determined by Shepherd formula at discharge mode (I < 0) (Eqn 9) and charge mode (I > 0) (Eqn 10) as follows:

$$V = e_{qd} - g_d H + I r_{qd} \left(1 + \frac{m_d H}{\frac{Q_d}{Q_m} - H} \right) \tag{9}$$

$$V = e_{qc} - g_c H + I r_{qc} \left(1 + \frac{m_c H}{\frac{Q_c}{Q_m} - H} \right) \tag{10}$$

where and are open circuit voltage at full charge and discharge, H is the depth of discharge, and gc are battery coefficients, and internal resistances at full discharge and charge, m_d and m_c are cell type parameters, and are capacity parameters for discharge and charge and is rated capacity of the cell (Keelialafreniere, 2018). Power was given as input in this model, which works with Type 48 regulator-inverter used to regulate the power and to provide AC/DC conversion. The power withdrawal and release were calculated by multiplying the power of a single unit with the number of units in series and parallel. The input parameters of the model such as cell energy capacity, charging efficiency, the maximum charging and discharging current, the maximum charging voltage and discharge cutoff voltage are listed in Table 4, which were determined based on the selected battery for this study (SUNLIGHT RES OPzV-2V 26 RES POzV 4535). Li-ion battery was not modelled in TRNSYS, but it was included in the study to determine the effect of the battery type on the number of batteries required and the economic performance of the considered scenarios. The number of Li-ion batteries used in the system was calculated based on the battery capacity given at the same C-rate (i.e., discharge rate) with the lead acid battery and the battery charging efficiency (Table 3). In addition, the economic performance of the Li-ion containing scenarios was evaluated considering the lifetime of Li-ion battery, which is also shown in Table 3. The selection of battery models for both lead-acid and Li-ion batteries was made based on the availability of large capacity batteries in the market.

Table 4. Technical Parameters of Batteries

Parameters	Lead Acid (Sunlight RES 4535)	Li-Ion (Huawei Luna2000)
C_{10}	3996 Ah	320 Ah
V_{nom}	2 V	51.2 V
E	7.99 kWh	16.38 kWh
η_{ch}	90%	99.0%
$I_{max,ch}$	424.8 A	320 A
$I_{max,dis}$	-424.8 A	-320 A
V_{max}	2.45 V	3.50 V
V_c	1.80 V	2.70 V
Lifetime	2500 cycle (at 60% DOD)	3600 cycle (100% DOD)

3.1.3 Regulator-Inverter Modeling

Type 48 regulator-inverter model in TRNSYS software was used for power regulation and AC/DC conversion. This model simply regulates the power between the load, PV array and batteries and does the related power conversion. For the energy analysis campus buildings inverters with different powers were selected since each building has a different installed power capacity. The selected inverters and their powers are seen in Table 5. Depending on these inverter models and MPPT inputs, the series-parallel connections of the panels were determined.

Table 5. The Selected Inverters and Their Power Values

Inverter Model	Power (W)
Huawei Inverter SUN200-12KTL	12,000
Huawei Inverter SUN200-17KTL	17,000
Huawei Inverter SUN200-30KTL	30,000
Huawei Inverter SUN200-33KTL	33,000
Huawei Inverter SUN200-36KTL	36,000
Huawei Inverter SUN200-40KTL	40,000
Huawei Inverter SUN200-50KTL	50,000
Huawei Inverter SUN200-105KTL	105,000
Huawei Inverter SUN200-110KTL	110,000
Huawei Inverter SUN200-185KTL	185,000

3.2 PVSOL Modeling

The design of the rooftop PV panel was made by the PV*SOL software, which requires an analysis of roof structures and meteorological data. The design of each building was made separately and for each installation the solar radiation data was taken from the METEONORM database. Rooftop panel system design varies according to roof area and type. The roof types of buildings at the IZTECH campus are inclined and flat. In sloping roofs, elevation is given based on the slope of the roof by performing a 3-dimensional layout. The heights and roof slopes of IZTECH campus buildings were not known. Therefore, the average roof height for pitched roofs (between 6-10 degrees) was used in this study (Bilgili & Dağtekin, 2019; Atılgan, 2019). The orientation of the panels on pitched roofs varies depending on the building design. Figure 4 shows an example of a pitched roof panel installation.

Figure 4. Pitched Roof Panel Installation

In flat roofs, there are specific parameters when the 3D layout is done. These parameters are panel slope, azimuth angle, shading, and distance between panels. The solar radiation that a photovoltaic module can receive depends on the module's direction. The panel slope and the azimuth angle are the factors that determine the orientation of the module (Prakash, 2020). Since IZTECH campus building locates in the northern hemisphere, they were taken as pointing to the south, so the azimuth angle was taken as 0° while the optimum panel slope was

determined as 38.4° based on the annual average solar radiation and directions (Yıldız, 2017). This angle was used in the TRNSYS modelling of PV modules.

In photovoltaic system designs, even a tiny amount of shadow cast on the panels can significantly reduce the output current. For this reason, it is essential to choose as much shadow-free area as possible for the photovoltaic system design to be installed. The shadow falls on the photovoltaic panel systems installed on the building due to an obstacle calculated as follows (PVSOL, 2023):

$$L > \frac{H}{tan\,\alpha} \tag{11}$$

If the distance (L) between the obstacle and the module is greater than the value of H/tanα, shadow formation will not occur due to the obstruction. Since the installation was considered on the rooftops of the campus buildings and there are no high-rise buildings, trees, or any other obstacles near to the buildings, the external shading on the photovoltaic modules were excluded. The only shadow effect can be seen due to the successive panel alignment. To prevent this effect, the optimum inter-row spacing needs to be determined. The safe distance between the two modules was calculated as follows:

$$d = w * (\frac{sin\,\beta}{tan\,\gamma} + cos\,\beta) \tag{12}$$

where w is the panel length, γ is the shadow angle and β is the panel slope. Based on the formula and solar data, the optimum inter row spacing was calculated as 2.75 m.

The PV array design was made by entering the calculated parameters into the PV*SOL program and the maximum allowable rooftop PV panel was determined for each building. Figure 5 shows an exemplary flat roof panel setup installed.

Figure 5. Flat Roof PV Panel Installation by PV-Sol Software

3.3 Economic Analysis

Economic feasibility is the main concern for the realization of renewable energy systems. In this study, the economic performance of all PV-battery scenarios was evaluated by Levelized Cost of Energy (LCOE) and Net Present Value (NPV) analysis.

3.3.1 Levelized Cost of Energy (LCOE)

The levelized cost of energy (LCOE) indicates the average cost per kWh of electricity produced by the system during the system lifetime. LCOE was calculated as follows:

$$LCOE = \frac{\sum_{t=0}^{n} \frac{I_t + M_t + Re_t}{(1+i)^t}}{\sum_{t=1}^{n} \frac{E_t}{(1+i)^t}} \quad (13)$$

where t is the number of time period, is the investment cost in the year t, is the operations and maintenance cost (O&M Cost) in the year t, Re_t is the replacement cost in the year t, is the electrical energy generated in the year t, is the interest rate, n is the expected lifetime of the system (Park C. S., 2016). The initial investment cost, operation and maintenance costs and lifetime for each component of the PV-battery system are shown in Table 6. The interest rate was taken as 5% (İçöz, 2022). The analysis was made for the system's lifetime of 25 years.

3.3.2 Net Present Value (NPV)

Net Present Value (NPV) analysis shows the difference between the present value of cash inflow and outflow, and it is an indication for the profitability of the project in the system lifetime. NPV value of systems were calculated by the following formula (Altun, 2021; Saray, 2019; Acakpovi, Adjei, Nwulu, & Asabere, 2020; Gokcol & Dursun, 2013):

$$NPV(i,N) = \sum_{t=1}^{N} \frac{R_t}{(1+i)^t} - R_0 \tag{14}$$

where is the net cash flow, R_0 is the total initial investment cost, is the interest rate, t is the time of cash flow, and N is the project lifetime (Park C. S., 2016). The net cash flow was determined by taking the difference between the annual money saved due to self-electricity generation and the annual O&M Cost while the total investment cost was calculated based on costs of components listed in Table 6. The installation cost of 25,000$/MW was also included in the calculation of total investment cost for all scenarios. The electricity price was taken 0.153 $/kWh in 2019. The analysis was made for the system's lifetime of 25 years and the replacement costs of batteries were also included in the analysis for related years.

Table 6. Investment Cost, O&M Cost, Replacement Cost, Lifetime of the PV-battery system components

Equipment	**Investment Cost**	**O&M Cost**	**Replacement Cost**	**Lifetime**
Jinko 525Wp PV Panel	180$	- 0 for 1st-5th years (warranty period) - 0,5% of the initial investment cost for 5th-10th years - 1% of the initial investment cost for 10th-25th years (Girgin, 2011; Ozcan, 2009)	100%	25 years

Huawei Inverter	2.000-3.300$ for 12-50 kW, 5.600-6.700$ for 100-185 kW (Europe Solar Store, 2023)	- 0 for 1st-5th years (warranty period) - 0,5% of the initial investment cost for 5th-10th years - 1% of the initial investment cost for 10th-25th years (Girgin, 2011; Ozcan, 2009)	100%	25 years
Sunlight RES 4535 Lead Acid Battery 7.99 kWh	1,044$ (Sunlight RES OpzV, 2023)	20 $/kW.year (NREL, 2023)	100%	7 years
Huawei Luna2000 Li-ion Battery 16.38 kWh	5,766$ (MG Solar Shop, 2023)	10$/kW.year (NREL, 2023)	100%	10 years

4. Result and Discussions

Four off-grid renewable energy scenarios were evaluated to meet the electricity consumption of the faculty buildings in the IZTECH Campus. For each scenario, the annual electricity consumption of each building and the annual electricity generation by PV array were determined on an hourly basis and the number of required batteries to cover the mismatch between the load and generation were calculated. The dynamic simulation was made by TRNSYS to confirm that a continuous power supply is sustained throughout the year. Based on the number of PV panels and batteries, LCOE and NPV analysis were made, and economic performances of systems were evaluated comparatively.

4.1 Electricity Load Profile of the Campus

The total annual electricity consumption and the hourly load profile of each building in the campus were analyzed to determine the scale of PV and battery systems. The annual electricity consumption of each building was determined based on the electricity consumption of the whole campus and the share of buildings in total electricity consumption (see section 2.2) and listed in Table 7. As seen from the table the annual electricity consumption of buildings var-

ies between 3.08 and 719.387 MWh. The level of consumption is high for the buildings housing a high population and requiring strict air-conditioning control. To observe the change in electricity consumption of buildings throughout the year the daily electricity consumption of each building in the campus was also determined. The daily load profiles of buildings have almost the same trend. Therefore, the load profile of each building was not shown separately here, but the load profile of the whole campus is presented instead to indicate the level of change. Figure 6 shows the daily consumption of the whole campus starting from 1st January to 31st December. As seen from the Figure, the daily load is between 8000-17000 kWh due to the mild climate conditions of spring and autumn seasons while it varies between 12000-27000 kWh and 10000-27000 kWh for winter and summer seasons, respectively. The load observed in spring and autumn seasons is mainly related to lighting and electrical equipment whereas the additional consumption observed in winter and summer seasons is caused by electricity-driven HVAC systems. The total electricity load in summer is higher than that in winter since part of heating requirements in winter is met by fossil fuel powered heating systems. Figure 6 also shows that there is an exceptional power outage (i.e., zero load) for a certain period (ca. 4 days) at the beginning of September. This is related to the planned maintenance-repair work done by the relevant distribution company.

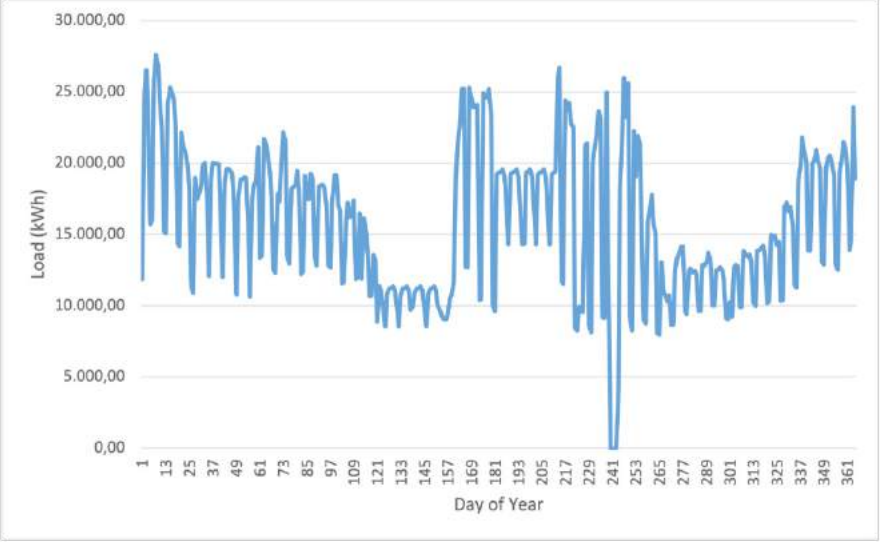

Figure 6. Daily load profile of the IZTECH Campus throughout the year

The hourly load profile of the campus for the day with a peak load was also analyzed. Figure 7 shows hourly load profile of the whole campus for the day (8th

January) with the highest daily consumption (27,207 kWh). The figure indicates that the hourly electricity consumption increases at the working hours from the base load to the daily maximum and drops to the base load at the end of the working day.

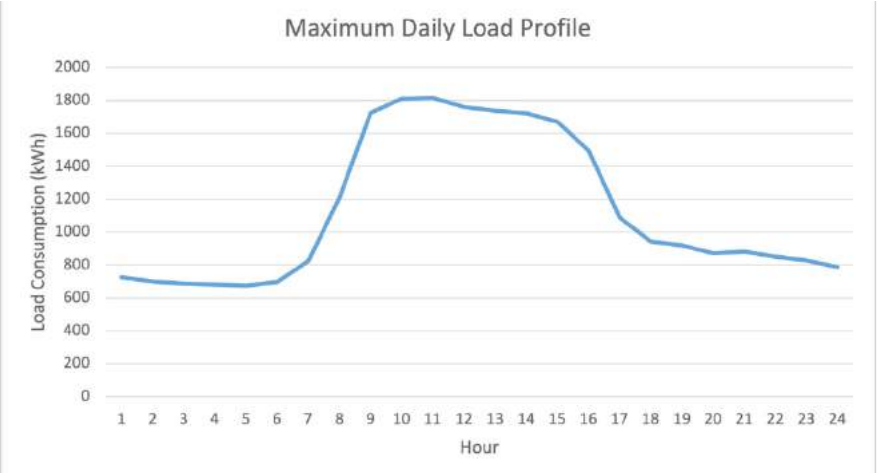

Figure 7. The Hourly Load Profile of the IZTECH Campus for the Day With A Peak Load (8th January)

4.2 Determination of Numbers of PV Panels And Battery

For the MPVB and MPVC scenarios, the maximum amount of PV panels that can be installed on the roof of each building was calculated by PV-SOL software. The results are shown in Table 7 and Table 8 along with total annual electricity generation by PV panels, electricity consumption and coverage ratios. The coverage ratio indicates what percentage of electricity is met by PV panels. As seen from Table 6, the coverage ratio is less than 100% for some buildings while it is above 100% for some of them. The coverage ratio of <100% indicates that some of the buildings don't have sufficient roof area for PV installation to cover their annual electricity consumptions. For buildings with a coverage ratio of >100%, batteries were considered to prevent the daily and seasonal mismatch between the load and generation and the number of batteries were determined based on the maximum cumulative energy deficiency in a year (Table 7). On the other hand, for buildings with a coverage ratio <100% the number of batteries were determined to compensate the electricity deficiency throughout the year to sustain off-grid system design. Due to this reason, the number of batteries for buildings with a coverage ratio <100% were found to be significantly higher than those for self-sufficient buildings. The calculations were made for both lead-acid and Li-ion batteries for all buildings. The number of Li-ion batteries were found to be less than the number

lead-acid batteries as expected due to higher energy storage capacity and depth of discharge of Li-ion batteries (see Table 4). The results show that the total number of PV panels installed on the available rooftop area of each building is 9108 and the total amount of energy produced by those PV panels is 4,319,266 kWh annually. This corresponds to the coverage ratio of 75%, which leads to the significant amount of battery utilization (N_{PbA}: 522,406, $N_{Li\text{-}ion}$: 202,705) to compensate for the energy deficiency. To reduce the number of batteries, buildings can be energetically connected or an additional area other than rooftop can be used for more PV installation, which are discussed in the following parts.

Table 7. The Number of PV Panels and Batteries, The Annual Electricity Consumption and Generation for the MPVB Scenario

NPVB		# of Panel	# of Lead-Acid B.	# of Li-ion B.	# of additional PV Panels	Area required for additional PV installation (m^2)	PV Output
		Quantity	Quantity	Quantity	Quantity	Area	kWh
GENERAL CULTURE BUILDING		54	530	293	-26	-	24,149
RECTORATE		448	2,19	1,167	344	910	210,729
HEAD OF DEPARTMENT		400	4,5	1,02	112	300	188,387
FACULTY OF SCIENCE	A BLOCK	376	3,658	1,848	24	60	177,084
	B BLOCK	576	4,38	1,618	216	560	271,278
	C BLOCK	287	2,45	1,142	-153	-	135,168
	CLASSROOM B.	90	860	517	-132	-	42,387
	PHYSICS BUILD.	676	4,926	2,25	280	730	318,375
	MATHS BUILD	187	1,32	714	99	226	88,071
	BIOLOGY BUILD	1.605	13,221	4,686	1.345	3,500	755,904
FOREIGN BUILDING	F. ADMINISTRATE	96	830	374	-108	-	45,213
	F. A BLOCK	34	540	212	-94	-	16,013
	F. B BLOCK	582	6,17	1,892	120	320	274,104
	F. ENERGY S.E.	66	800	158	-222	-	31,084
	CENTERAL W.	60	466	348	-228	-	28,258
MECHANICAL ENG.		1.120	7,651	5,712	724	1,880	527,485
FACULTY OF ARCHITECTURE	A BLOCK	273	3,555	1,146	-87	-	128,574
	B BLOCK	208	3,254	744	-212	-	97,961
	C BLOCK	39	87	64	-37	-	18,368
	D BLOCK	4	20	6	-126	-	1,884
	E BLOCK	64	640	220	-140	-	30,142
CHEMISTRY ENG		1.456	11,9	5,996	1.120	2,900	685,73
COMPUTER ENG		385	3,76	2,084	-31	-	181,323
LIBRARY		882	6,826	5,098	477	1,250	415,394
GYM CENTER		252	3,923	2,928	-432	-	118,684
POOL		456	4,33	1,568	252	670	214,762
CAFE		188	2,58	514	-40	-	88,542
CIVIL ENG		470	4,274	3,164	-70	-	221,355
ELECTRIC ELECTRONIC ENG		302	4,01	3,424	-114	-	195,923
INTEGRATED RESEARCH		945	8	4,358	612	1,580	445,065
TOTAL		**12,581**	**111,651**	**55,265**	**3,473**	**14,886**	**5,977.396**

Table 8. The Number of PV Panels and Batteries, The Annual Electricity Consumption and Generation for the MPVC Scenario

	Load (kWh)	Number of Panel	Number of Lead Acid Battery	Number of Li-ion Battery	PV Output (kWh)	Coverage Ratio (%)
MPVC	5,748,700	9,108	226,200	107,482	4,321,136	75.16

The MPVB scenario takes each building as a single unit and excludes energy transfer between the buildings. This leads to the utilization of a significant number of batteries. To prevent this situation and to observe how much improvement can be obtained in the number of batteries, the same analysis was made for MPVC scenario, which takes buildings as energetically interconnected. The results in Table 8 show that the number of batteries decreases almost 2-fold (N_{PbA}: 226,200, $N_{Li\text{-}ion}$: 107,482) indicating that a significant cost saving can be obtained by this strategy as seen in Section 4.3.

MPVB and MPVC scenarios show that the available roof areas for PV installation are not adequate to meet the total annual electricity consumption of the campus. This leads to excessive battery utilization and poor economic performance considering the high cost of batteries in the current market. In this respect NPVB and NPVC scenarios were also evaluated to determine the effect of additional PV installation on the required number of battery and on the system economy for each building and the whole campus, respectively. For the NPVB scenario, Table 9 shows the amount PV panels required to cover the annual electricity consumption of each building, the additional number of PV compared to the MPVB scenario, and the land area required for the installation of these additional PV panels. As seen from the Table, the total additional PV panels for the whole campus and the required land area 3,473 and 14,886 , respectively. With the installation of these PV panels the required number of batteries decreases by ca. 4 to 5-fold compared to the MPVB scenario, which provides significant cost savings. When buildings are considered to transfer energy between each other (NPVC scenario), further improvements were obtained, i.e., the number of batteries drops to 56,180 and 38,981 for lead-acid and Li-ion batteries, respectively (Table 10).

Table 9. The Number of PV Panels And Batteries, the Additional PV Panels, and the Corresponding Land Area for the NPVB Scenario

NPVB		# of Panel	# of Lead-Acid B.	# of Li-ion B.	# of additional PV Panels	Area required for additional PV installation (m^2)	PV Output
		Quantity	Quantity	Quantity	Quantity	Area	kWh
GENERAL CULTURE BUILDING		54	530	293	-26	-	24,149
RECTORATE		448	2,19	1,167	344	910	210,729
HEAD OF DEPARTMENT		400	4,5	1,02	112	300	188,387
FACULTY OF SCIENCE	A BLOCK	376	3,658	1,848	24	60	177,084
	B BLOCK	576	4,38	1,618	216	560	271,278
	C BLOCK	287	2,45	1,142	-153	-	135,168
	CLASSROOM B.	90	860	517	-132	-	42,387
	PHYSICS BUILD.	676	4,926	2,25	280	730	318,375
	MATHS BUILD	187	1,32	714	99	226	88,071
	BIOLOGY BUILD	1.605	13,221	4,686	1.345	3,500	755,904
FOREIGN BUILDING	F. ADMINISTRATE	96	830	374	-108	-	45,213
	F. A BLOCK	34	540	212	-94	-	16,013
	F. B BLOCK	582	6,17	1,892	120	320	274,104
	F. ENERGY S.E.	66	800	158	-222	-	31,084
	CENTERAL W.	60	466	348	-228	-	28,258
MECHANICAL ENG.		1.120	7,651	5,712	724	1,880	527,485
FACULTY OF ARCHITECTURE	A BLOCK	273	3,555	1,146	-87	-	128,574
	B BLOCK	208	3,254	744	-212	-	97,961
	C BLOCK	39	87	64	-37	-	18,368
	D BLOCK	4	20	6	-126	-	1,884
	E BLOCK	64	640	220	-140	-	30,142
CHEMISTRY ENG		1.456	11,9	5,996	1.120	2,900	685,73
COMPUTER ENG		385	3,76	2,084	-31	-	181,323
LIBRARY		882	6,826	5,098	477	1,250	415,394
GYM CENTER		252	3,923	2,928	-432	-	118,684
POOL		456	4,33	1,568	252	670	214,762
CAFE		188	2,58	514	-40	-	88,542
CIVIL ENG		470	4,274	3,164	-70	-	221,355
ELECTRIC ELECTRONIC ENG		302	4,01	3,424	-114	-	195,923
INTEGRATED RESEARCH		945	8	4,358	612	1,580	445,065
TOTAL		**12,581**	**111,651**	**55,265**	**3,473**	**14,886**	**5,977.396**

Table 10. The number of PV panels and batteries, the additional PV panels, and the corresponding land area for the NPVC scenario

	Panel	Number of Lead Acid Battery	Number ofLi-ion Battery	Number of additional PV Panels	Area required for additonal PV installation (m^2)	PV Output (kWh)
NPVC	12,581	56,180	38,981	3,473	14,886	5,977.396

For all scenarios the dynamic system simulation was made on TRSNYS and the continuous power supply by PV-battery combination was controlled throughout the year. Figure 8 shows the change of electricity demand, electricity generation and battery utilization in time throughout the year for the best scenario (NPVC). Figure clearly indicates that the battery charge/discharge properly compensates the mismatch between the load and electricity generation by PV array and does not allow any power cut.

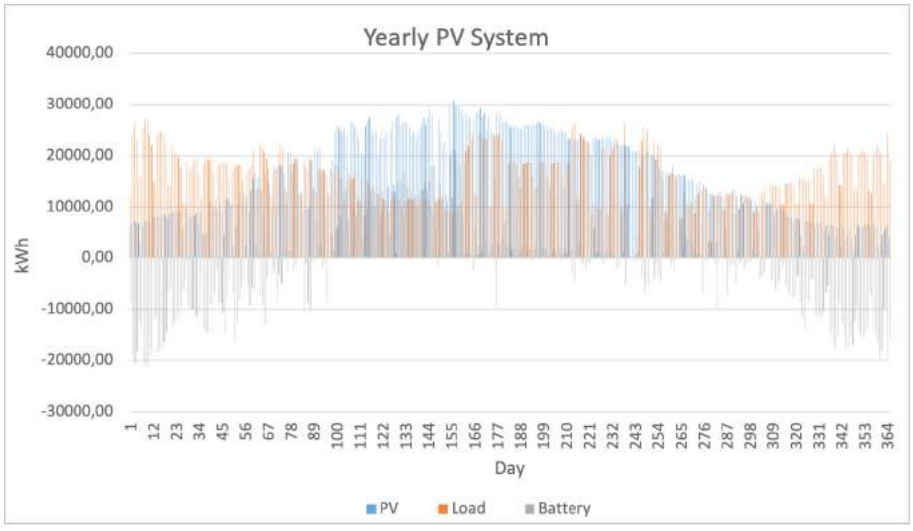

Figure 8. The Daily Change Of Electricity Demand, Electricity Generation And Battery Utilization for the NPVC Scenario

4.3 Economic Analysis

The economic feasibility of off-grid scenarios was evaluated by LCOE and NPV analyses. The initial investment costs were calculated based on the number of

PV panels, battery and inverter calculated in Section 3.2 and cost items shown in Table 6. The cost details of the investment cost for all scenarios are shown in Table 11 and 12. According to the related cost items and yearly expenses including O&M cost and replacement cost, LCOE and NPV values were determined and listed in Table 13 and 14 for lead-acid battery and Li-ion battery, respectively. The results show that the highest NPV and the lowest LCOE values were obtained for the NPVC scenario where the lowest number of batteries is employed. Since the total battery cost accounts for almost 99% of total investment cost and batteries needs to be replaced in the project lifetime, scenarios with a higher number of batteries yield lower NPV and higher LCOE values and any reduction in battery number results in a significant improvement in the system economy. This suggests that the battery utilization needs to be minimized for improving the economic viability of the system, which can be achieved by increasing the number of PV and by allowing energy transfer between campus buildings. The effect of the former is clearly seen in the comparison of MPVB and NPVB or MPVC and NPVC scenarios, i.e., a ca. 40% increase in the number of PV results in a 4-7-fold decrease in the LCOE value. A significant reduction in the number of batteries and the corresponding improvement in LCOE values was also obtained by energy transfer between campus buildings. This effect results in a 1.5-2.5-fold decrease in the LCOE value indicating the importance of energetically interconnected buildings.

Table 11. Cost and Percentage Values for all Lead Acid Batteries Including Scenarios

	Initial Investment				
	Cost Item	Quantity	Price ($/ unit)	Price ($)	%
MPVB-Lead Acid	PV Panel	9,108	180	$1,639,440	0.30
	Pb-acid battery	522,406	1,044	$545,391,864	99.63
	Inverter	89	-	$305,481	0.06
	Infrastructure	-	-	$100,000	0.02
		Total		$547,436,785	100

	Cost Item	Quantity	Price ($/ unit)	Price ($)	%
MPVC-Lead Acid	PV Panel	9,108	180	$1,639,440	0.69
	Pb-acid battery	226,200	1,044	$236,152,800	99.19
	Inverter	26	7,402	$192,452	0.08
	Infrastructure	-	-	$100,000	0.04
	Total			$238,084,692	100
	Cost Item	Quantity	Price ($/ unit)	Price ($)	%
NPVB-Lead Acid	PV Panel	12,581	180	$2,264,580	1.90
	Pb-acid battery	111,651	1.044	$116,563,644	97.66
	Inverter	379	-	$263,506	0,22
	Infrastructure	-	-	$260,000	0,22
	Total			$119,351,730	100
	Cost Item	Quantity	Price ($/ unit)	Price ($)	%
NPVC-Lead Acid	PV Panel	12,581	180	$2,264,580	3.69
	Pb-acid battery	56,180	1,044	$58,651,920	95.46
	Inverter	35	7,402	$263,506	0.43
	Infrastructure	-	-	$260,000	0.42
	Total			$61,440,006	100
	Cost Item	Quantity	Price ($/ unit)	Price ($)	%
MB-Lead Acid	PV Panel	114,340	180	$20,581,200	75.66
	Pb-acid battery	3,790	1,044	$3,956,760	14.54
	Inverter	325	7,402	$2,405,650	8.84
	Infrastructure	-	-	$260,000	0.96
	Total			$27,203,610	100

Table 12. Cost and Percentage Values for All Li-Ion Batteries Including Scenarios

	Initial Investment				
	Cost Item	Quantity	Price ($/ unit)	Price ($)	%
MPVB-Li-ion	PV Panel	9,108	180	$1,639,440	0.14
	Pb-acid battery	202,705	5,766	$1,168,797,030	99.80
	Inverter	194	-	$656,089	0.06
	Infrastructure	-	-	$100,000	0.01
	Total			$1,171,192,559	100
	Cost Item	Quantity	Price ($/ unit)	Price ($)	%
MPVC-Li-ion	PV Panel	9,108	180	$1,639,440	0.26
	Pb-acid battery	107,482	5,766	$619,741,212	99.69
	Inverter	26	7,402	$192,452	0.03
	Infrastructure	-	-	$100,000	0.02
	Total			$621,673,104	100
	Cost Item	Quantity	Price ($/ unit)	Price ($)	%
NPVB-Li-ion	PV Panel	12,581	180	$2,264,580	0.70
	Pb-acid battery	55,265	5,766	$318,657,990	99.12
	Inverter	62	-	$316,686	0.10
	Infrastructure	-	-	$260,000	0.08
	Total			$321,499,256	100

	Cost Item	Quantity	Price ($/ unit)	Price ($)	%
NPVC-Li-ion	PV Panel	12,581	180	$2,264,580	0.99
	Pb-acid battery	38,981	5,766	$224,764,446	97.85
	Inverter	325	7,402	$2,405,650	1.05
	Infrastructure	-	-	$260,000	0.11
	Total			$229,694,676	100
	Cost Item	Quantity	Price ($/ unit)	Price ($)	%
MB-Li-ion	PV Panel	114,340	180	$20,581,200	59.09
	Pb-acid battery	2,009	5,766	$11,583,894	33.26
	Inverter	325	7,402	$2,405,650	6.91
	Infrastructure	-	-	$260,000	0.75
	Total			$34,830,744	100

Table 13. LCOE and NPV Values For All Lead-Acid Battery Including Scenarios (interest rate=%5)

Scenario	Quantity of Panel	Quantity of Lead-Acid B.	NPV ($)	LCOE ($/ kWh)
MPVB	9,108	522,406	-1,146,214,817.20	19.3
MPVC	9,108	226,200	-489,590,710.92	8.4
NPVB	12,581	111,651	-231,322,607.67	3.0
NPVC	12,581	56,180	-108,380,325.16	1.5
MB	114,340	3,790	138,814,908.59	0.044

Table 14. LCOE and NPV Values for All Li-Ion Battery Including Scenarios. (interest rate=%5)

Scenario	Quantity of Panel	Quantity of Li-ion Battery	NPV ($)	LCOE ($/kWh)
MPVB	9,108	202,705	-1,804,518,099.77	30.4
MPVC	9,108	107,482	-951,037,639.58	16.1
NPVB	12,581	55,265	-484,966,477.54	6.0
NPVC	12,581	38,981	-335,278,616.50	4.3
MB	114,340	2,009	129,218,972.21	0.057

For each scenario the economic performance of two battery options were also evaluated separately to determine the effect of battery selection on the LCOE and NPV values. The comparison between Table 13 and 14 clearly shows that the utilization of lead-acid battery is economically more favorable than that of Li-ion battery for the considered scenarios. This is attributed to the high cost of Li-ion battery that is 3-fold higher than that of lead-acid battery per kWh. Even if Li-ion battery has a higher energy capacity, depth of discharge and lifetime, the high cost of Li-ion battery makes itself unfavorable for the considered system size.

Economic analyses show that all considered scenarios yield negative NPV values suggesting that the total investment cannot be restored within the project lifetime. This is mainly associated with the high cost of batteries in the market. To make the related system economically feasible, the number of batteries needs to be minimized. Based on these findings, a new scenario called minimum battery (MB) scenario was also considered and its economic feasibility was evaluated. In the MB scenario, campus buildings were taken as energetically connected and the number of batteries was decreased to the limit where the off-grid system was still maintained with a minimum number of batteries. The required numbers of lead-acid and Li-ion batteries for the related scenario are 3790 and 2009, respectively (Table 13 and 14). This significant reduction in the battery numbers is related to excessive PV utilization (114,340 PV panels) and the resulting electricity generation (53,850,540 kWh/year), which allows to prevent power deficiency even in wintertime where solar radiation is relatively low due to the overlap between the period of PV-sourced electricity generation and consumption (Figure 7). NPV and LCOE values for the MB scenario were calculated as 138,814,908.59$ and 0.044$/kWh for lead-acid battery and 129,218,972.21$ and 0.057$/kWh for Li-ion battery. Even if NPV values of the MB scenario are positive and LCOE values are close to those reported in the literature for on-grid renewable energy

system designed for university campus, the excessive electricity generation (ca. 10-fold higher than the consumption) makes this scenario unfeasible.

To assess the relative economic performance of off-grid systems in comparison to on-grid systems, LCOE values of the NPVC scenario in off-grid and on-grid mode were compared. As seen from Table 15, the LCOE value of the on-grid system is 0.04$/kWh, which is >3 times less than the lead-acid battery containing off-grid system. This indicates that off-grid systems are economically less feasible than on-grid systems for IZTECH campus. This is mainly related to the high cost of batteries. To make off-grid system compete with on-grid system, the prices of lead-acid and Li-ion batteries needs to be decreased by more than 50 and 100 folds, respectively, or their lifetime must increase significantly, which depends on R&D activities in the coming decades.

Table 15. LCOE and NPV Calculated For All Scenarios NPVC - On Grid

Scenario	Quantity of Panel	NPV	LCOE
NPVC-ON	12,581	2,987,268.97$	0.04$/kWh

For all calculation explained above the interest rate was taken as 5%, which has shown significant variations for Turkey recently. To address this issue, the effect of interest rate on LCOE values for MB and NPVC scenarios was also investigated for various interest rates considering both lead acid and Li-ion batteries as energy storage units. As shown from Figure 9, the interest rate has a significant effect on LCOE values for both scenarios, i.e., more than 2-fold reduction was observed when the rate decreases from 12% to 1%. For the NPVC scenario the minimum LCOE value (3.3 $/kWh) obtained for 1% interest rate is still way above the LCOE value of the on-grid scenario while for the MB scenario the LCOE value goes below the value obtained for the on-grid scenario when the interest rate is below 4%. This suggests that the NPVC scenario can not compete with the on-grid scenario even at very low interest rate whereas the MB scenario can be more favorable compared to the on-grid scenario based on the interest rate.

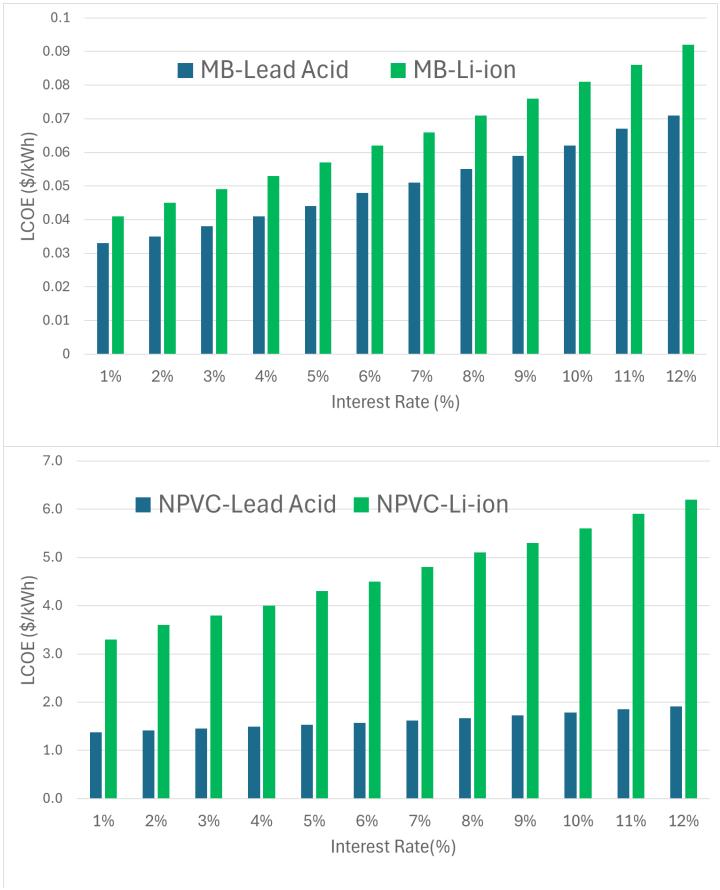

Figure 9. LCOE Values At Different Interest Rates for MB (left panel) and NPVC (right panel) Scenarios Considering Both Lead Acid and Li-Ion Batteries As Energy Storage Units

5.Conclusions

Technoeconomic analyses of standalone PV-Battery systems were conducted for the campus buildings of Izmir Institute of Technology (IZTECH) located in Izmir, Turkey. This study aims to assess the viability of self-sustaining university campuses powered by renewable sources. Given the advantageous solar radiation potential at the campus location, photovoltaic (PV) technology emerged as a suitable renewable option and its integration with battery technologies was evaluated to explore the technoeconomic feasibility of grid-independent campus. Four different off-grid scenarios were evaluated: (i) maximum PV installation for each building of the campus (MPVB), (ii) maximum PV installation on the whole cam-

pus (MPVC), (iii) necessary PV installation for self-sufficiency of each building of the campus (NPVB), and (iv) necessary PV installation for self-sufficiency of the whole campus (NPVC). In all scenarios, two types of batteries were considered: lead-acid and Li-ion batteries. Main conclusions are as follows:

- The NPVC scenario showed the highest NPV and the lowest LCOE values due to the significant reduction in battery utilization compared to other scenarios by enabling higher PV installation and facilitating energy transfer between buildings.
- Lead-acid battery-containing scenarios were found to be more economically feasible compared to Li-ion battery-containing scenarios.
- Off-grid renewable energy systems are less economically viable than on-grid counterparts due to the high price of batteries.
- Battery prices need to be reduced significantly or their lifetime must be improved drastically to make off-grid system feasible.

6. Declaration of Competing Interest

The work described in this paper has been neither copyrighted, classified, published, nor is being considered for publication in any other journals. The authors declare that this study adhered to research and publication ethics. There is no conflict of interest among the authors.

Acknowledgements

This research was not financially supported by any funding agencies in the public, commercial, or not-for-profit sectors. The authors gratefully acknowledge Dr. Hüseyin Günhan Özcan from Bahcesehir University Energy Systems Engineering Department for the support in TRNSYS modelling.

List Of Symbols

β Slope of PV array (°)

γ The azimuth angle of the inclined plane (°)

θ The latitude of the location

ω Hour Angle (°)

δ Declination Angle (°)

α Obstacle angle (°)

θ Angle of incidence for solar radiation (°)

$\theta_{eff,diff}$ Diffuse of incidence for solar radiation (°)

θ_{gnd} Ground-reflected of incidence for solar radiation (°)

τa_{normal} Module transmittance-absorptance product at normal incidence

η_{ch} Efficiency

C Capacity (Ah)

d Module row distance (m)

E Power (kWh)

E_t Electrical energy generated

e_{qc}, e_{qd} Open circuit voltages at full charge, extrapolated from V vs I curves on charge; discharge

H Obstacle Height (m)

H_d Depth of discharge

L Distance between the obstacle (m)

G_T Total radiation incident on PV array (W/m^2)

$G_{T,beam}$ Beam component of incident radiation (W/m^2)

$G_{T,diff}$ Diffuse component of incident radiation (W/m^2)

$G_{T,gnd}$ Ground-reflected component of incident radiation (W/m^2)

$G_{T,ref}$ Incident radiation at reference conditions (W/m^2)

g_c, g_d Small-valued coefficients of H in voltage-current-state of charge formulas (W/m^2)

I Current (A)

I_L Module photocurrent

$I_{L,ref}$ Module photocurrent at reference conditions

I_0 Diode reverse saturation current

$I_{0,ref}$ Diode reverse saturation current at reference conditions

I_{sc} Short-circuit current

I_{max} Current at maximum power point along IV curve

$I_{max,ch}$ Maximum Battery Charge (A)

I_t Investment expenditures

I_{AM} Dimensionless incidence angle modifier

i Discount rate

k Boltzmann constant [J/K]

m_c, m_d Cell-type parameters which determine the shapes of the I-V-Q character-

	istics
M_T	Operations and maintenance expenditures
N	Project Lifetime
N_p	Number of modules in parallel in array
N_S	Dimensionless incidence angle modifier
P	PV output power
R_0	Total Initial Investment Cost
Re_t	Net cash flow
R_s	Module series resistance [Ω]
r_{qc}, r_{qd}	Internal resistances at full charge when charging; discharging
T_c	Module temperature [K]
$T_{c,ref}$	Module temperature at reference condition (25°C)
t	Time of cash flow
w	Panel Length (m)
V	Voltage
V_c	
V_{max}	Voltage at maximum power point along IV curve
V_{OC}	Open-circuit voltage
V_{nom}	Nominal Voltage
q	Electron Charge (1.6x10-19 C)
Q_m	Rated capacity of cell
Q_c, Q_d	Capacity parameters on charge; discharge

References

Acakpovi, A., Adjei, P., Nwulu, N., & Asabere, N. Y. (2020). Optimal Hybrid Renewable Energy System: A Comparative Study of Wind/Hydrogen/Fuel-Cell and Wind/Battery Storage. *Journal Electrical Computer Engineering,* 64, 249-57. http://doi: 10.1155/2020/1756503.

Altun, A. F. (2021). *Şebekeden Bağımsız, Güneş ve Rüzgar Kaynaklı, Batarya ve Hidrojen Depolamalı Hibrit Enerji Sistemlerinin Dinamik Modellemesi, Enerji, Ekserji ve Seviyelendirilmiş Maliyet Analizi.* (Master Thesis). Bursa Uludağ Üniversitesi Fen Bilimleri Enstitüsü, Bursa.

Atılgan, F. (2019). Balıkesir İlindeki PV Sistemlerinin Analizi. (Master Thesis).

Balıkesir Üniversitesi Fen Bilimleri Enstitüsü Elektrik-Elektronik Mühendisliği Anabilim Dalı. Balıkesir.

Aykut, E., & Terzi, K. (2020). Techno-Economic and Environmental Analysis Off-Grid Connected Hybrid Wind/Photovoltaic/Biomass System for Marmara University Goztepe Campus. *International Journal of Green Energy,* 15, 1036-1043. https://doi.org/10.1080/15435075.2020.1821691.

Bilgili, M. E., & Dağtekin, M. (2019). Supplying the Electricity for the Broiler Poultry Houses from Photovoltaic Solar Panels in the Adana Conditions. *Çukurova II.Uluslararası Multidisipliner Çalışmalar Kongresi,* 793-805, Adana.

Chedid, R., Sawwas, A., & Fares, D. (2020). Optimal Design of a University Campus Micro-Grid Operating under Unreliable Grid Considering PV and Battery Storage. *Energy* 200, 117510. https://doi.org/10.1016/j.energy.2020.117510.

Dursun, B. (2012). Determination of the optimum hybrid renewable power generating systems for Kavakli campus of Kirklareli University, Turkey. *Renewable and Sustainable Energy Review, Elsevier,* 6183-6190. http://doi.org/10.1016/j.rser.2012.07.017.

Europe Solar Store. (2023). Huawei Inverters https://www.europe-solarstore.com/instantsearchplus/result/?q=huawei%2050%20ktl.

Fernando, W., Gupta, N., Özveren, S. C., & Linn, H. H. (2018). Design of Optimum Configuration of a Hybrid Power System for Abertay University Campus. *IEEE Conference of Russian Young Researchers in Electrical and Electronic Engineering.* https://doi.org/10.1109/EIConRus.2018.8317454.

Günerhan, S. A., & Günerhan, H. (2016). *Türkiye için Sürdürülebilir Üniversite Modeli.* 57(682), 54-62.

Girgin, M. H. (2011). *Bir Fotovoltaik Güneş Enerjisi Santralinin Fizibilitesi Karaman Bölgesinde 5 MW'lık Güneş Enerjisi Santrali için Enerji Üretim Değerlendirmesi ve Ekonomik Analizi.* (Master Thesis), İstanbul Teknik Üniversitesi Enerji Enstitüsü, Istanbul.

Gokcol, C., & Dursun, B. (2013). A Comprehensive Economical and Environmental Analysis of the Renewable Power Generating Systems for Kırklareli University, Turkey. *Energy and Buildings,* 64, 249-57. https://doi: 10.1016/j.enbuild.2013.05.005.

İçöz, D. (2022). *Design and Techno-economic Analysis of a Smart Solar GreenHouse.* (Master Thesis). Izmir Institute of Technology Faculty of Engineering, Izmir.

John, D. A., & Beckham, W. A. (1991). *Solar Enginnering of Thermal Processes.* New York: John Wiley& Sons, Inc.

Klein, S. A., Beckman, W. A., Mitchell, J. W., Duffie, J. A., Duffie, N. A., Freeman, Mitchell, J. C., Braun, J. E. Keelialafreniere, K. L. (2018). *TRNSYS 18 a Transient System Simulation Program, Volume 4, Mathematical Reference.*

Khan, K. S., Ullah, Z., Khan, B., Sami, İ., Ali, S., & Mehmood, C. A. (2017). Assessment of Hybrid Off-Grid Wind Photovoltaic System: A Case Study of University Campus. *International Conference on Energy Conversation Effienciency Proceedings,* 16-21. https://doi: 10.1109/ECE.2017.8248822.

MG Solar Shop (2023). Huawei Battery Storage. https://www.mg-solar-shop.com/pv-battery-systems/storages-solar-batteries/huawei-battery-storage/.

NREL. (2023). 2023 Electricity ATB Technologies and Data Overview. https://atb.nrel.gov/electricity/2023/index.

Oymen, G. (2020). Yenilenebilir Enerjinin Sürdürülebilirlik Üzerindeki Rolü. *İstanbul Ticaret Üniversitesi Sosyal Bilimler Dergisi,* 1069-1087. https://doi: 10.46928/iticusbe.769022.

Ozcan, H. (2009, Ocak). *Bir Hibrid Enerji Sistemin Modellenmesi ve Analizi.* İstanbul Teknik Üniversitesi Fen Bilimleri Enstitüsü Elektrik Mühendisliği, 2, 1-8.

Park, C. S. (2016). *Contemporary Engineering Economics.* Harlow, UK: Pearson.

Park, E., & Kwon, J. (2016). Solutions for Optimizing Renewable Power Generation Systems at Kyung-Hee University's Global Campus, South Korea. *Renewable and Sustainable Energy Review,* 58:439-449. doi: 10.1016/j.rser.2015.12.245.

Prakash, C. (2020). *What are the site related and most sensitive parameters to optimiza a large-scale PV installation at Stavanger airport?* (Master Thesis). University of Scavenger Faculty of Science and Technology, Scavenger.

PVSOL (2023). https://help.valentin-software.com/pvsol/en/calculation/

Saray, E. (2019). *Yenilenebilir Enerji Üretim ve Yatırım Maliyetleri Karşılaştırması: Ege Bölgesi Örneği.* Pamukkale Üniversitesi Sosyal Bilimler Enstitüsü İşletme Anabilim Dalı. Denizli.

Sava, G. N., Ionescu, G., Necula, H., Scripcariu, M., Duong, M. Q., Leva, S., & Mussetta, M. (2017). Efficiency Analysis of a Hybrid Power System for a Campus in Romania. *IEEE International Conference on Environment and Electrical Engineering and 2017 1st IEEE Industrial and Commercial Power Systems Europe, EEEIC.* https://doi.org/10.1109/EEEIC.2017.7977527.

Sevilgen, G. (2008). Yenilenebilir Enerji Kaynakları Sürdürülebilirlik Endeksi. *Uludağ Üniversitesi Mühendislik-Mimarlık Fakültesi Dergisi,* 479-492.

Sunlight RES OpzV (2023). (n.d.). Retrieved from https://www.the-sunlight-group.com/en/global/products/res-opzv/.

TEİAŞ. (2020). *2020 Yılı Elektrik Üretim-Tüketim Raporu-TEİAŞ.* https://www.tei-as.gov.tr/turkiye-elektrik-uretim-iletim-istatistikleri.

TMMOB. (2020). *Enerji Politikaları; Yerli, Yeni ve Yenilenebilir Enerji Kaynakları.* https://www.emo.org.tr/ekler/98024cb5e21d749_ek.pdf.

World Energy Council. (2016). E-storage: Shifting from cost to value, wind and solar applications. https://www.worldenergy.org/publications/entry/e-storage-shifting-from-cost-to-value-2016.

Yıldız, M. (2017, March). *Hybrid Energy Capacity of Turkey for Small and Micro Scale Energy Production.* Izmir Institute of Technology Faculty of Engineering, Izmir.

Mühendis ve Makina / Engineer and Machinery
https://dergipark.org.tr/tr/pub/muhendismakina

OPTIMIZATION OF A THERMOELECTRIC COOLER FOR A TURBOCHARGED TRACTOR

Ali Kürşad ARICIOĞLU[1], Gülay YAKAR[2*], Ali GÜRCAN[3]

[1] Akdeniz Üniversitesi, Mühendislik Fakültesi, Makine Mühendisliği Bölümü, Antalya
ORCID No : http://orcid.org/0000-0001-6293-4237

[2] Pamukkale Üniversitesi, Mühendislik Fakültesi, Makine Mühendisliği Bölümü, Denizli
ORCID No : http://orcid.org/0000-0002-1865-7815

[3] İstanbul Gelişim Üniversitesi, İstanbul Gelişim Meslek Yüksekokulu, Makine Bölümü, İstanbul, ORCID No : http://orcid.org/0000-0002-2745-1413

Keywords

Thermoelectric, cooler, electric, power input

Abstract

This work covers a numerical analysis of the design and optimization of a thermoelectric cooler (TEC) operated by a thermoelectric generator (TEG). The aim of the work was to design the optimum mini refrigerator for tractors and also to provide cooling using the energy produced in the TEG used in the tractor. Thanks to the TEC powered with the TEG system, farmers will be able to preserve their food during working hours without additional fuel consumption. When the literature is examined, no study has been found in which cooling is done by using the compressor air of turbocharged systems. Therefore, this work will make an important contribution to the literature. According to the numerical results obtained, while the electrical power requirement was 34.78 W at an outdoor temperature of 30 °C, it was 26.54 W at an outdoor temperature of 15 °C. In other words, while the coefficient of performance was obtained as 0.301 at 15 °C, it was determined as 0.219 at 30 °C. In addition, while the electrical power value produced by the TEG system used in the tractor for an outdoor temperature of 15 °C was 50.71 W, it was 38.84 W at an outdoor temperature of 30 °C.

* gyakar@pau.edu.tr
doi : 10.46399/muhendismakina.1427599

TURBOŞARJLI BİR TRAKTÖR İÇİN BİR TERMOELEKTRİK SOĞUTUCUNUN OPTİMİZASYONU

Anahtar Kelimeler

Termoelektrik, soğutucu, elektrik, güç girişi

Öz

Bu çalışma, bir termoelektrik jeneratör (TEJ) tarafından çalıştırılan bir termoelektrik soğutucunun (TES) tasarımı ve optimizasyonunun sayısal bir analizini kapsamaktadır. Çalışmada, traktörler için optimum mini buzdolabının dizayn edilmesi ve aynı zamanda traktörde kullanılan TEJ'de üretilen enerji ile soğutmanın sağlanması amaçlandı. TEJ sistemi ile çalıştırılan TES sayesinde çiftçiler, ek yakıt tüketimine gerek kalmadan, mesai saatleri içerisinde gıdalarını muhafaza edebilecekler. Literatür incelendiğinde, turboşarjlı sistemlerin kompresör havası kullanılarak soğutmanın yapıldığı herhangi bir çalışmaya rastlanmamıştır. Dolayısıyla bu çalışma, literatüre önemli bir katkı sağlayacaktır. Elde edilen sayısal sonuçlara göre, elektrik gücü ihtiyacı 30 °C dış sıcaklıkta 34,78 W iken, 15 °C dış sıcaklıkta 26,54 W olarak elde edilmiştir. Yani performans katsayısı 15 °C'de 0,301 olarak elde edilirken, 30 °C'de 0,219 olarak belirlendi. Ayrıca traktörde kullanılan TEJ sisteminin, 15 °C dış ortam sıcaklığında ürettiği elektrik gücü değeri 50,71 W iken, 30 °C dış ortam sıcaklığında 38,84 W olmuştur.

Araştırma Makalesi
Başvuru Tarihi : 29.01.2024
Kabul Tarihi : 15.03.2024

Research Article
Submission Date : 29.01.2024
Accepted Date : 15.03.2024

1. Introduction

Today, advances in technology and a growing interest in comfort conditions mean that the need for proper cooling is increasing daily. Systems that use thermoelectric (TE) modules are widely employed for the purposes of heating, cooling and generating electricity. Such systems are simple and relatively maintenance-free. If they are used to generate electricity, they are given the name TEGs, while they are referred to as TECs when used for cooling. Cheng and Lin (2005) emphasized that both the coefficient of performance and the cooling capacity of TEC modules are highly important. They suggested a method to optimize the dimensions of the TEC legs using genetic algorithms, in order to maximize the cooling capacity. Their results showed that optimizing the dimensions of the TEC module can enhance the cooling capacity. Khattab and El Shenawy (2006) conducted a study on the optimal operating conditions of a small TEC driven by a solar TEG. They determined that five thermocouples of the TEG could drive one thermocouple of the TEC. In other words, their results indicated that 10 TEG modules would be needed to operate the TEC used at optimum performance for most of the year.

Meng, Chen and Sun (2010) used non-equilibrium thermodynamic theory to analyze the extreme operating temperature difference of a combined TE system consisting of a TEC or a heat pump driven by a TEG. Their results indicated that a 60 K temperature difference for cooling or 200 K for heating can be obtained if a TEG actuates under a temperature difference of 150 K. Chen, Meng and Sun (2012) suggested a TE refrigerator model with external heat transfer driven by a TEG. They investigated the effects of the allocation of the thermoelement and heat transfer area using numerical examples that were highly detailed. They were able to obtain an optimum operating electric current with regard to the maximum cooling load and coefficient of performance, with different total numbers of thermoelements and a different total heat transfer area. Chen, Wang and Hung (2014) numerically analyzed a geometrically designed integrated TEG-cooling system by means of a finite element technique. The maximum reduction percentages of system performance that they obtained were 12.45% and 18.67%, when the TEG and TEC lengths were altered. Attar, Lee and Weera (2015) experimentally validated the optimum design required for an automotive air-to-air TE air conditioner. The optimum design of the TE air conditioner was obtained with a new method using the recently developed dimensional analysis. Hasani and Rahbar (2015) experimentally studied the recovery of TE waste heat from a PEM fuel cell. Their results indicated that the use of TECs was a viable method for the recovery of such heat from a PEM fuel cell. In addition, the overall efficiency of the system decreased as the leaving water temperature increased.

Manikandan and Kaushik (2015) proposed and analyzed a combined system

using the technique of maximum power point tracking in order to achieve the greatest possible cooling power alongside overall efficiency. They demonstrated the impact of the source temperature of the TEG and TEC, and the heat transfer area on how the combined system performed. Their results found that the external irreversibilities reduced cooling power of the combined system and the overall efficiency by 36.49% and 16.9%, respectively. Zhang, Kong, Dong, Xu, Chen and Ni (2017) proposed an innovative hybrid system consisting primarily of a TEG, a TEC and solid oxide fuel cells used in the recovery of waste heat from the latter for in order to enhance performance. Their work took full account of the thermodynamic and electrochemical irreversible losses from every specific component. They also detailed the equivalent power output and efficiency for the hybrid system under differently operating regions of current density. They found that the power density and efficiency of the system proposed were 2.3% and 4.6% larger respectively than those of the stand-alone solid oxide fuel cells. Feng, Chen, Meng and Sun (2018) established a thermodynamic model for a TEC powered by a TEG device, taking into account the Thomson effect, analyzing and optimizing its performance. Their conclusions indicated that the Thomson effect reduced the productivity of the TEC-TEG, in that it decreased the cooling capacity by 27 %, as well as decreasing the coefficient of performance by 19 %.

Nemati, Nami, Yari and Ranjbar (2018) carried out exergy and exergoeconomic analyses of an electrically separated two-stage TEC. They found that the optimal first-stage current was lower than that of second-stage current, and, in addition, that the maximum exergy efficiency was obtained with currents at lower values compared to the minimum cooling cost. Lin, Zhang, Liu, Meng, Chen and Wang (2019) improved and extensively investigated single-stage and two-stage TEC-TEG systems. They proposed a fresh design for combined TEC-TEG systems using two single-stage TEGs to power the hot stage and the cold stage of the TEC separately. They found that the new design both increased the system's cooling capacity and increased the maximum temperature drop in the TEC. Kishore, Nozariasbmarz, Poudel, Sanghadasa and Priya (2019) studied in combination the effect of heat sink thermal resistances and TE material properties on TEC performance. Their results showed that efficient TECs are able to bring human skin down to a temperature 8.2 °C beneath the ambient temperature. That is, their modules achieved a 70% higher cooling than commercial modules. Sun, Liu, Shen, Chen, Yao and Jin (2019) intended to construct a model high-power light-emitting diode package integrated with a micro-TEC and to examine its performance with regard to several different interfacial and size effects. They determined that the best cooling performance was found in a micro-TEC with 6×6 TE elements for the driving power of a micro-TEC that was less than 0.85 W.

Sadighi Dizaji, Jafarmadar, Khalilarya and Pourhedayat (2019) experimentally

examined the impact of a number of parameters on exergy destruction and the performance of the second law through a TE air cooler. Their study explained the consequences of flow and thermodynamic parameters, among them DC voltage/ampere, incoming water temperature, water flow rate, incoming air temperature, and air flow rate on exergetic characteristics. They obtained a critical DC voltage value where the second law performance obtained minimum/maximum values. Lu, Li, Zhang, Ning and Niu (2020) built a three-dimensional trapezoidal TEC model at full scale in order to test its mechanical reliability and cooling performance through finite element simulation. Their results function as a helpful guide for designing trapezoidal TECs. Gonzalez-Hernandez (2020) studied the energetic analysis of a TEC, with optimization criteria being unified through the "x" variable. He suggested new modes of operation for both cooler and heater. Shen, Zhang, Liu, Tu, Lu, Chen and Huang (2020) proposed a segmented TEC for the purpose of enhancing cooling performance while not increasing the overall figure of merit. They developed the governing equations and physical model of the segmented TE element with regard to internal heat distribution and transport. Their results indicated that the segment number had a higher sensitivity to the thermal conductivity of the TE material, while the temperature difference and maximum cooling capacity of the segmented TE element were greater than those the conventional TE element.

Tian, Asaadi, Moria, Kaood, Pourhedayat and Jermsittiparsert (2020) examined the geometric characteristics of a tubular TEC as an air cooler, which have not been reported before. They found that a tubular TEC can be used for the purpose in question if the thermal and geometric parameters chosen are within the desired range. Qiu and Shi (2020) constructed a model with the aim of determining the factors influencing the cooling capacity of a TEC qualitatively and quantitatively utilizing finite element analysis. Their results indicated that there was a 35.73% and 21.59% improvement in the cooling capacity and the coefficient of performance of an optimized TEC with a non-constant cross-section, respectively, in comparison to a constant cross-section TEC. Kwan, Gao, Zhao, Ren, Hu, Dabwan and Pei (2021) analyzed whether it was feasible to integrate the radiative sky cooling capability of common photovoltaic cells into the photovoltaic-TEC in order to increase the space cooling energy density to a further extent. Huang, Chen and Ding (2021) examined a new two-stage TEC in a configuration that was electrically parallel. They detected that the thermocouple ratio between the two stages, the area-to-length ratio of the legs, and the cold side temperature had a significant impact on some important performance characteristics. Chen, Shi, Zou and Chen (2022) comprehensively reviewed the progress of cutting-edge on-chip TECs and outlined the relevant fundamentals, materials, designs, and system logic.

Sun, Shen, Niu, Gao, Zhou, Tang … Yang (2022) developed a numerical model with three dimensions in order to explore the micro-TEC's potential to reduce the negative impact of the fluctuating hot spot arising from thermal shock. Their results showed that the micro-TEC was able to check the temperature fluctuation seen in the chip subjected to thermal shock in an effective manner. Gürcan and Yakar (2022) analyzed the power output of a TEG located in a turbocharged tractor between the compressor and intercooler. They emphasized that this system's power output could be employed for electrically powered devices, such as a TEC refrigerator, the electrical power need of which could be met through the use of the TEG system. Gürcan and Yakar (2022) examined the impact of widths of thermocouples on the conversion from thermal to electric energy. According to their results, the increase in current was 14.67% at = 0.75; 15.4% at = 1; 15.95% at = 1.25, and 16.2% at = 1.5 for the TGM-199-1.6-2.0, when compared to the TGM-199-1.4-2.0.

The aim of the present study is to optimize a TEC for a turbocharged tractor. Moreover, the electrical energy need of this TEC is supplied by a TEG system that obtains power by using the air leaving the compressor of the turbocharged tractor (the literature generally discusses TEG systems that use the exhaust gas). Thanks to the TEC powered by this TEG system, farmers working in the field for long periods of time will be able to preserve the food and the cold beverages they need easily, especially in summer. In addition, the power requirement of this system is supplied by the TEG system on the same tractor, so it is possible to operate the mini refrigerator without additional fuel consumption. This means that the tractor owner can achieve these comfort conditions at no additional cost.

When the literature is examined, no study has been found in which cooling is done by using the compressor air of turbocharged systems. However, this work uses the compressor air to cool the refrigerator. This is the innovative aspect of the work.

2. Design of Mini Refrigerator With TEC

The mini refrigerator with TEC was designed to fit inside a turbocharged tractor (Arıcıoğlu, 2021). It was planned that the refrigerator door would open from above in order to save the volume inside the tractor (Figure 1). The electrical energy need of this TEC was supplied by a TEG system that could obtain electrical power using the air leaving the compressor of the turbocharged tractor (Gürcan, 2019). In the literature TEG systems generally use the exhaust gas. Thanks to this TEC mini refrigerator powered by the TEG system, farmers will be able to preserve their food and cool their drinks during working hours, especially in summer, without any additional fuel consumption.

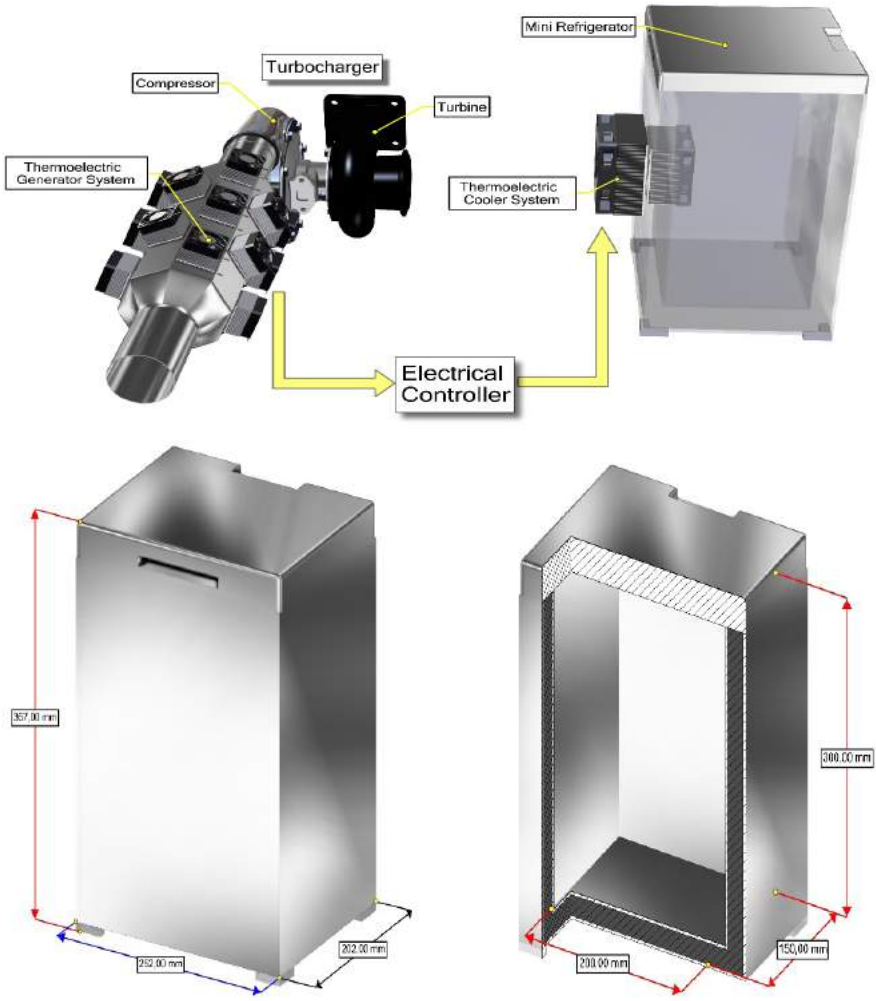

Figure 1. (a) The Mini Refrigerator with TEC Powered by TEG (b) External View and Dimensions (c) Internal Volume and Dimensions

30 mm thick polyurethane foam insulation material was used on the upper surface, while a 20 mm thick layer of the same material was used on all other surfaces of the mini refrigerator. Thus, the amount of heat gain from the warmer outdoor environment was reduced. In addition, 3 mm thick Acrylonitrile Butadiene Styrene plastic material was used to cover the interior and exterior of this refrigerator. The interior volume of the refrigerator was designed to be 9 liters and the internal volume was kept at a constant temperature of 5°C. A TB-127-1.0-1.3 commercial TEC module was used in the mini refrigerator; where TB – TE battery; 127 – number of thermocouples; 1.0 – width of thermoelement, mm;

1.3 – leg length of thermoelement, mm. To detect how seasonal temperatures affected the numerical conclusions of this present work, analyses were performed with regard to specific outdoor temperatures (15, 20, 25, 30, 35, 40 and 45 °C).

Figure 2 shows a single thermocouple (a) and a TEC with two finned surfaces (b). In addition, Figure 3 provides an illustration of three-dimensional model of the TEC module.

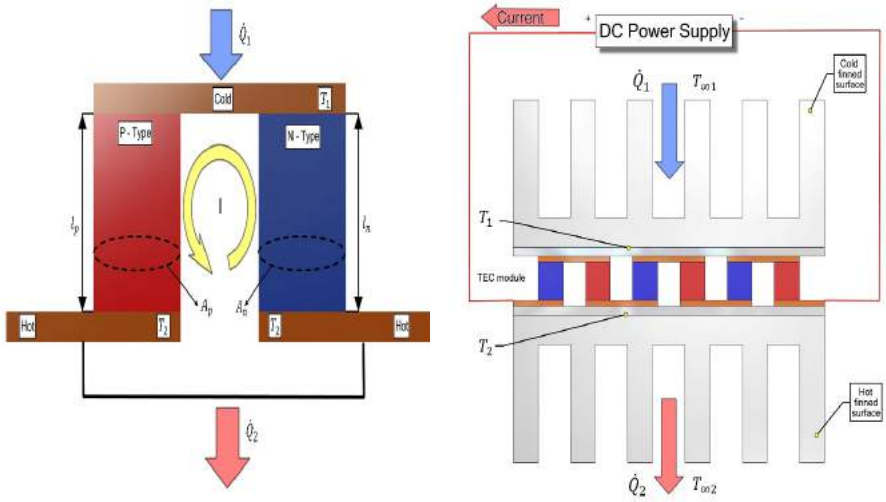

Figure 2. (a) A Thermocouple for a TEC (b) A TEC Module with Two Finned Surfaces

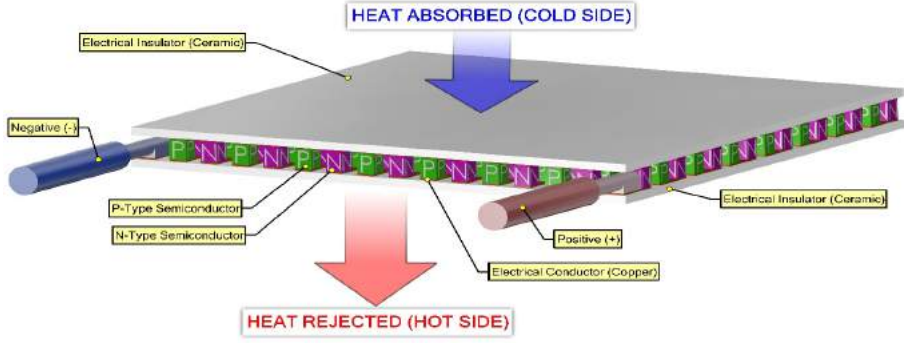

Figure 3. A TEC Module

As seen Figure 2b, when a DC voltage is applied to the TEC module or power is consumed, due to the properties of the thermocouple materials inside the mod-

ule -heat is drawn onto one surface of the module and cooling occurs depending on the direction and magnitude of the applied voltage.

A TE module is formed of series of thermocouples that consists of p-type and n-type thermoelements. Furthermore, these thermocouples are electrically connected in series and thermally connected in parallel. The thermoelement's leg length and cross-sectional area were and respectively. There were 127 thermocouples.

Research and publication ethics were complied with in this study.

3. Mathematical Expression of a TEC

The effective rejection or absorption of thermal energy through the use extended surfaces, such as fins is important. TEC modules largely deploy finned structures (heat sinks) for this reason. In the present study, the heat sink shown in Figure 4 was used.

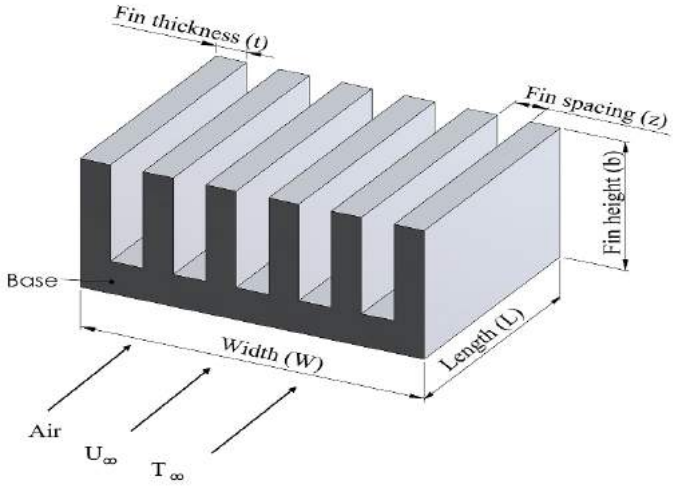

Figure 4. The Heat Sink Used This Study

The volume of the heat sink is fixed (Figure 4). For this reason, it is important to detect the optimum fin thickness (Lee, 2010). The fins used in the study were made of aluminum. The number of fins used in this study:

$$n_f = \frac{W}{z_{opt}+t} \tag{1}$$

where w is the finned structure width. In this equation, fin thickness is denoted

by t and optimum fin spacing is denoted by $_{zopt}$.

Equation (2) shows the fin efficiency:

$$\eta_f = \frac{tanh(\beta)}{\beta} \tag{2}$$

where

$$\beta = b\left(\frac{2h}{k_{al}t}\right) \tag{3}$$

where fin height is denoted as b, h represents the heat convective coefficient, and the thermal conductivity of the fin material is denoted by $_{kal}$.

A_f is the area of the fin:

$$A_f = 2\ (L+t)\ b \tag{4}$$

A_t is the sum finned surface area:

$$A_t = n_f\ (A_f + Lz_{opt}) \tag{5}$$

where the length of the finned structure is denoted as L. η is the efficiency of the overall finned surface:

$$\eta = 1 - n_f \frac{A_f}{A_t}\left(1 - \eta_f\right) \tag{6}$$

$\dot{Q}_t$ is the sum heat transfer rate:

$$\dot{Q}_t = \eta A_t h\ (T_{Base} - T_\infty) \tag{7}$$

where the finned structure base temperature is shown as T_{Base}, and the air temperature is denoted as T_∞.

The optimum fin spacing (z_{opt}) is written as follows (Lee, 2010):

$$z_{opt} = L_c 3.24 Re^{-1/2} Pr^{-1/4} \tag{8}$$

where the Reynolds number represents $Re\ (Re = \frac{U_\infty L_c}{\nu})$, Pr indicates the Prandtl number, the kinematic viscosity is denoted as ν, L_c, shows the characteristic length of flow, and U_∞ represents the velocity of air flow.

$$h = \frac{k_{air}}{L_c} 0.664 Re^{1/2} Pr^{1/3} \tag{9}$$

where the thermal conductivity of air is shown by k_{air}.

The MATLAB^R software was used with Equations (1) to (9) inclusive to determine the productivity of the finned structure for every thickness of fin, as well as to establish the optimum thickness of fin. Figure 5 illustrates the flow chart for the optimal values.

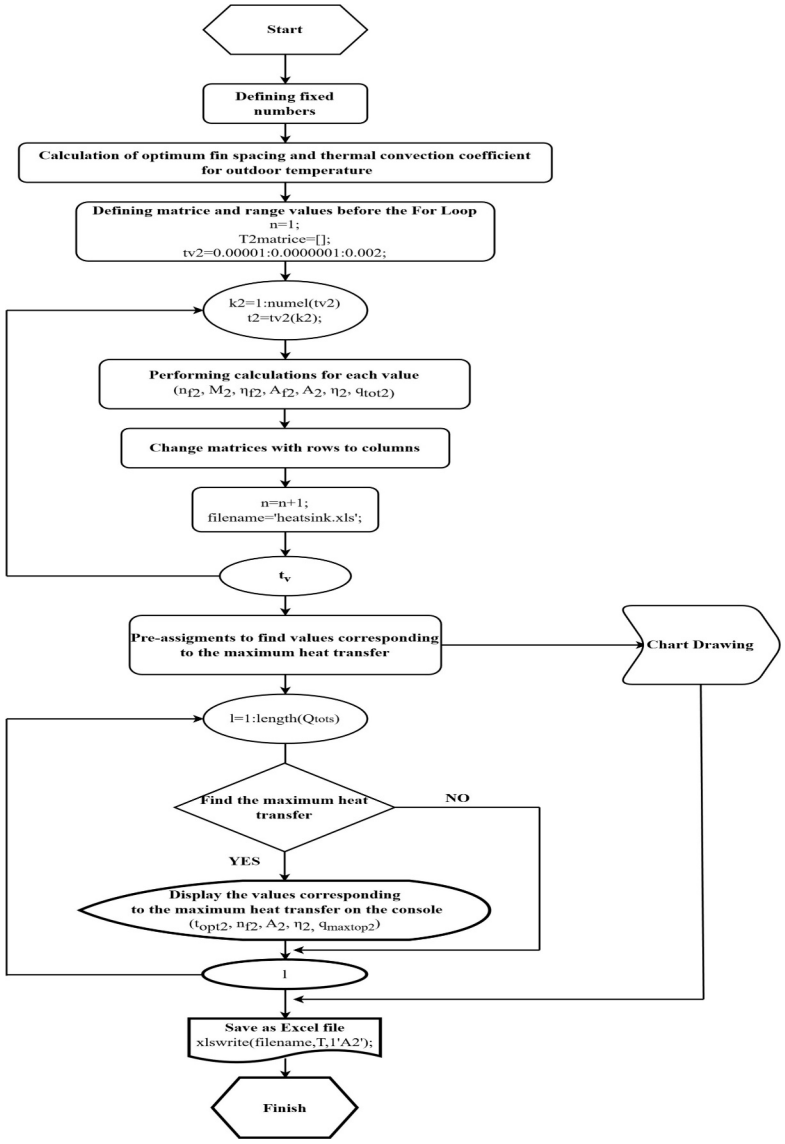

Figure 5. MATLAB^R Flow Chart for Optimal Values of Finned Structure on Hot Surface

The TE properties of the modules are not temperature dependent (Lee, 2017).

Numerical analyses were performed using the basic equations. These equations were formulated as following:

$\dot{Q}_1$ is the rate of heat absorbed at the cold side:

$$\dot{Q}_1 = n\left[\alpha I T_1 - \frac{1}{2}I^2R - K(T_2 - T_1)\right] \tag{10}$$

$$\dot{Q}_1 = \eta_1 h_1 A_{t1}(T_{\infty 1} - T_1) \tag{11}$$

$\dot{Q}_2$ is the rate of heat liberated at the hot side:

$$\dot{Q}_2 = n\left[\alpha I T_2 + \frac{1}{2}I^2R - K(T_2 - T_1)\right] \tag{12}$$

$$\dot{Q}_2 = \eta_2 h_2 A_{t2}(T_2 - T_{\infty 2}) \tag{13}$$

where the number of thermocouples of the module is shown by n, the cold surface temperature of the TEC module is denoted as T_1, the hot surface temperature of TEC module is shown as T_2, the cold ambient temperature is shown by $T_{\infty 1}$, the outdoor temperature is denoted by $T_{\infty 2}$ and electrical current is shown as I. Also, α, R, , and K are defined as follows, respectively:

$$\alpha = \alpha_p - \alpha_n \tag{14}$$

$$R = \frac{\rho_p l_p}{A_p} + \frac{\rho_n l_n}{A_n} \tag{15}$$

$$K = \frac{k_p A_p}{l_p} + \frac{k_n A_n}{l_n} \tag{16}$$

The internal electrical resistance is denoted by R and K indicates the thermal conductance. It is $R = \rho l/A$ and $K = kA/l$, $\rho = \rho_p + \rho_n$ and $k = k_p + k_n$. Moreover, shows the Seebeck coefficient, the thermal conductivity is shown by k, the electrical resistivity is denoted by , the leg length of the thermocouples is shown by l and the cross-sectional area of the thermocouples is shown as A (Lee, 2017).

According to $\dot{W} = \dot{Q}_2 - \dot{Q}_1$, power input required for the TEC can be defined as follows:

$$\dot{W} = n[\alpha I(T_2 - T_1) + I^2R] \tag{17}$$

Since the electrical power input is $\dot{W} = IV$, the voltage across the TEC module can be defined as

$$V = n[\alpha(T_2 - T_1) + IR] \tag{18}$$

The coefficient of performance is written by

$$COP = \frac{\dot{Q}_1}{\dot{W}} = \frac{n\left[\alpha T_1 I - \frac{1}{2} I^2 R - K(T_2 - T_1)\right]}{n[\alpha I(T_2 - T_1) + I^2 R]} \tag{19}$$

The study aimed to simulate how the TEC module would perform by employing these ideal Equations (10) to (19). TEC producers provide maximum parameter values $(I_{max}, V_{max}, \dot{Q}_{max} \text{ and } \Delta T_{max})$ (and) in their catalogs of products. However, the α, and k are not provided. Lee (2017) thus detailed the effective material properties. These properties need to be halved because TE material properties contain both thermoelements. indicates the effective figure of merit:

$$Z^* = \frac{2\Delta T_{max}}{(T_2 - \Delta T_{max})^2} \tag{20}$$

The effective Seebeck coefficient:

$$\alpha^* = \frac{2\dot{Q}_{1max}}{nI_{max}(T_2 + \Delta T_{max})} \tag{21}$$

The effective electrical resistivity is:

$$\rho^* = \frac{\alpha^*(T_2 - \Delta T_{max})A/l}{I_{max}} \tag{22}$$

The effective thermal conductivity:

$$k^* = \frac{(\alpha^*)^2}{\rho^* Z^*} \tag{23}$$

Novel dimensionless groups have been determined to represent the significant parameters of TECs. It is necessary, in particular, to use the convection conductance of a fluid in the denominators of the dimensionless parameters. Thus, the determination of the optimum thermoelements number or optimal thermal conductance is provided (Lee, 2017).

N_k is the dimensionless thermal conductance:

$$N_k = \frac{n(Ak/l)}{\eta_2 h_2 A_{t2}} \tag{24}$$

N_h is the dimensionless convection:

$$N_h = \frac{\eta_1 h_1 A_{t1}}{\eta_2 h_2 A_{t2}} \tag{25}$$

NI is the dimensionless current:

$$N_I = \frac{\alpha I}{Ak/l} \tag{26}$$

The dimensionless temperatures can be defined by

$$T_1^* = \frac{T_1}{T_{\infty 2}} \tag{27}$$

$$T_2^* = \frac{T_2}{T_{\infty 2}} \tag{28}$$

$$T_\infty^* = \frac{T_{\infty 1}}{T_{\infty 2}} \tag{29}$$

The dimensionless cooling power is:

$$Q_1^* = \frac{\dot{Q}_1}{\eta_2 h_2 A_{t2} T_{\infty 2}} \tag{30}$$

The dimensionless rate of heat liberated is:

$$Q_2^* = \frac{\dot{Q}_2}{\eta_2 h_2 A_{t2} T_{\infty 2}} \tag{31}$$

*W** is the dimensionless electrical power input:

$$W^* = \frac{\dot{W}}{\eta_2 h_2 A_{t2} T_{\infty 2}} \tag{32}$$

Utilizing the novel dimensionless groups expressed in Equations (24) through (29), Equations (10) through (13) reduce to two correlations:

$$\frac{N_h (T_\infty^* - T_1^*)}{N_k} = N_I T_1^* - \frac{(N_I)^2}{2ZT_{\infty 2}} + (T_1^* - T_2^*) \tag{33}$$

$$\frac{T_2^* - 1}{N_k} = N_I T_2^* + \frac{(N_I)^2}{2ZT_{\infty 2}} + (T_1^* - T_2^*) \tag{34}$$

where $Z=\alpha^2/\rho k$ (the figure of merit). Equations (33) and (34) can be solved for T_1^* and T_2^*. Dimensionless temperatures depend on five independent dimensionless parameters:

$$T_1^* = f(N_k, N_h, N_I, T_\infty^*, ZT_{\infty 2}) \tag{35}$$

$$T_2^* = f(N_k, N_h, N_I, T_\infty^*, ZT_{\infty 2}) \tag{36}$$

T_∞^* is the input and $ZT_{\infty 2}$ is the material property with the input. Both of these are given in the first instance. It is thus only possible to conduct optimization using, N_k , N_h and N_I parameters. After T_1^* and T_2^* have been calculated, the dimensionless heat transfer rates are found:

$$Q_1^* = N_h(T_\infty^* - T_1^*) \tag{37}$$

$$Q_2^* = T_2^* - 1 \tag{38}$$

Then, the dimensionless power input can be given by

$$W^* = Q_2^* - Q_1^* \tag{39}$$

Accordingly, the coefficient of performance can be written as

$$COP = \frac{Q_1^*}{W^*} \tag{40}$$

the dimensionless voltage is defined as

$$N_V = \frac{V}{n\alpha T_{\infty 2}} \tag{41}$$

and, dimensionless voltage is obtained by

$$N_V = \frac{W^*}{N_I N_k} \tag{42}$$

Placing the values calculated in Equations (33) and (34) leads to the formation of two equations with four unknowns. If T_1^* and T_2^* are to be determined on the basis of these equations, values must be known for N_I and N_k. These are thus entered as incremental values in the MATLAB^R. Optimum values were determined according to maximum cooling power. In this manner, T_1^*, T_2^* were obtained. Figure 6 presents the flow chart in relation to values obtained for the maximum cooling power, while Figure 7 presents the flow chart with regard to the optimization of these values for the optimum design. Table 1 shows the dimensionless values from the analysis using the MATLAB^R program for the seven specific outdoor temperatures according to the flow charts in Figures 6 and 7.

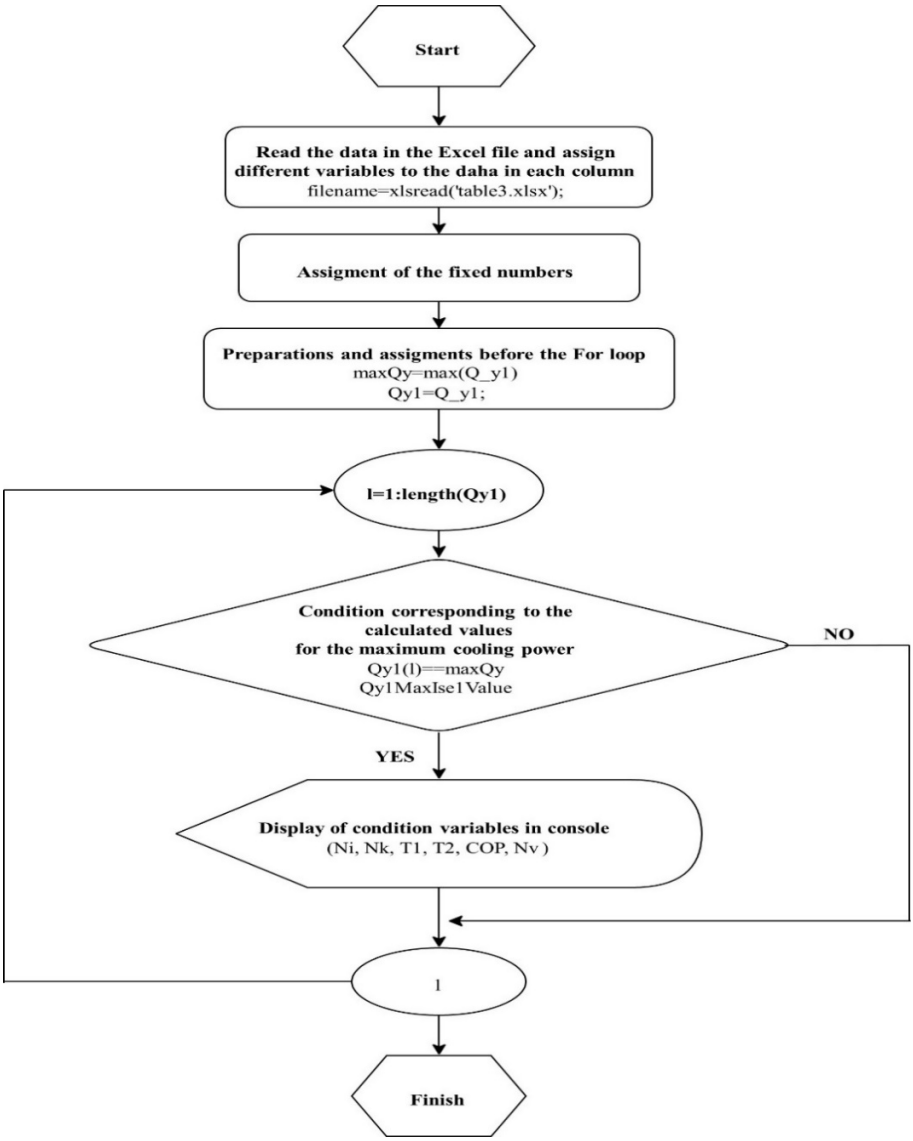

Figure 6. MATLAB^{R} Flow Chart in Relation to Values Obtained for Maximum Cooling Power

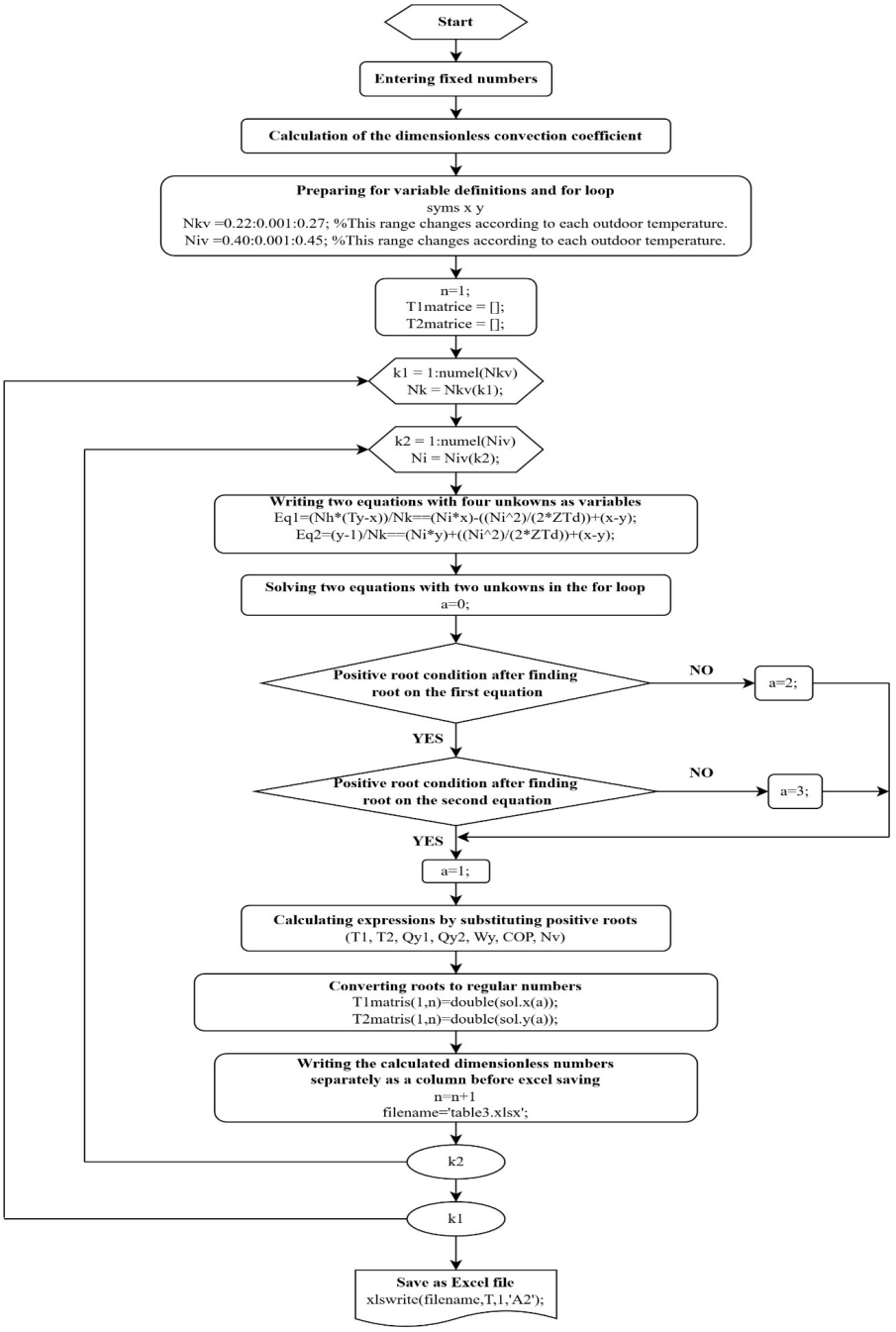

Figure 7. MATLAB[R] Flow Chart with regard to Solution of Optimization Values

Table 1. Optimal Dimensionless Parameters for the TB-127-1.0-1.3

$T_{\infty 2}$ (K)	T_{∞}^{*}	T_1^*	T_2^*	N_h	N_k	N_I	N_v	Q_1^*	COP
318	0.874	0.858	1.073	0.642	0.145	0.522	0.843	0.0099	0.156
313	0.888	0.869	1.079	0.635	0.162	0.503	0.824	0.0118	0.176
308	0.902	0.880	1.084	0.626	0.180	0.485	0.806	0.0138	0.197
303	0.917	0.891	1.089	0.618	0.199	0.467	0.787	0.0160	0.219
298	0.932	0.902	1.094	0.609	0.220	0.448	0.766	0.0184	0.244
293	0.948	0.913	1.098	0.599	0.243	0.429	0.745	0.0210	0.271
288	0.965	0.925	1.103	0.593	0.269	0.409	0.721	0.0239	0.301

4. Validation of the Numerical Solution

In order to verify the numerical solution, the performance values found by way of the use of the MATLAB^{R} software for the TB-127-1.0-1.3 were compared with the performance values informed in the company catalog (Kryotherm, 2018). Table 2 compares the performance values found by the company through experimentation with the performance values obtained with the MATLAB^{R} software.

Table 2. Verification of the Numerical Solution

Performance values	I (A)	ΔT (K)	$\dot{Q}_1$ (W)	V (V)
Company catalog (Experimentally)	3.6	69	34.5	15.7
Present study (Numerically)	3.6401	68.31	34.082	15.567
Relative error	1.11%	0.99%	1.21%	0.84%

The numerical conclusions of the present study were in accord with the conclusions obtained through experimentation in the company catalogue (Table 2).

5. The Numerical Analysis Results

In this study, a TEC mini refrigerator was designed to fit inside a turbocharged tractor. The electrical energy need of this TEC was supplied by a TEG system that could generate electrical power by utilizing the air compressed by the tractor's compressor. Thanks to this mini refrigeration with a TEC working with a TEG system, farmers will be able to preserve their food and cool their drinks during working hours, especially in summer, without any additional fuel consumption. Analyses were carried out for the seven specific outdoor temperatures to detect what effect different summer and winter conditions would have. The analysis

results using the MATLAB[R] software were found for a single TB-127-1.0-1.3. However, as the outdoor temperature increased, a single TEC module was not sufficient at outdoor temperatures above approximately 30 °C, as seen in Figure 12, and two TEC modules were needed.

5.1 Results Concerning Performance Analysis

Figure 8 shows the alterations in the cooling power and the coefficient of performance for seven different outdoor temperatures.

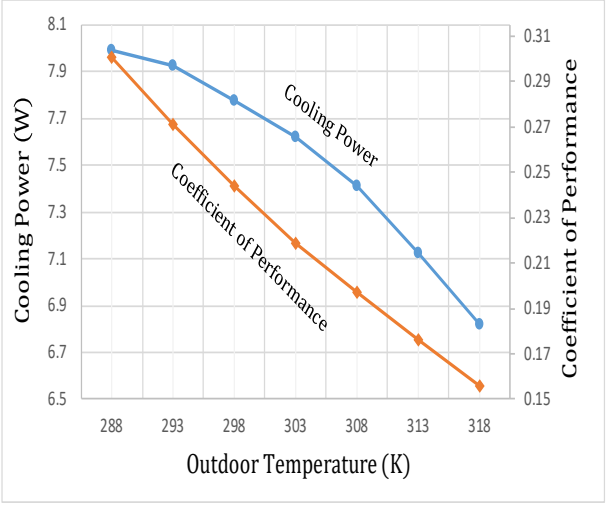

Figure 8. Variation of Cooling Power and Coefficient of Performance of TEC Module with Different Outdoor Temperatures

The cooling power decreased with increasing outdoor temperature (Figure 8). This is because as the outdoor temperature increases, the temperature difference between hot and cold surfaces increases. In other words, the maximum cooling power in TECs is obtained at = 0 K (Lee, 2017). In addition, the surface temperature of the cold side increased with an increment in the outdoor temperature. This means less heat is absorbed from the volume to be cooled at the constant cold ambient temperature. As a result, for a single TEC module, the highest cooling power was obtained as 7.989 W at 288 K outdoor temperature and the lowest cooling power was 6.818 W at 318 K outdoor temperature.

Figure 8 shows that the coefficient of performance also decreased with increasing outdoor temperatures. This situation is observed in all cooling systems. The same is also openly seen in the coefficient of performance of the reversed Carnot cycle. Accordingly, it was determined that the maximum coefficient of perfor-

mance value was 0.301 at 288 K outdoor temperature and the lowest coefficient of performance value was 0.156 at 318 K (Figure 8).

Figure 9 illustrates voltage and power input values at different current values.

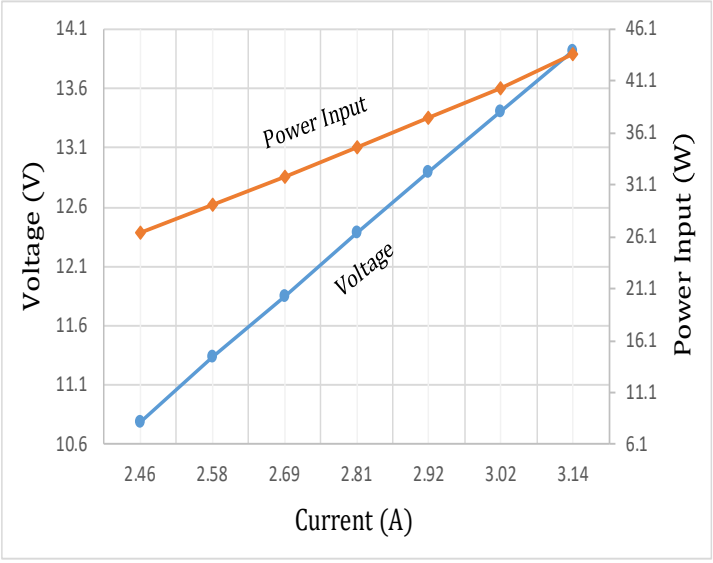

Figure 9. Voltage and Power Input for the TEC Module at Different Electrical Current

As seen in Figure 9, The voltage and the power input also increased with the electrical current. That is, the voltage and the power input were increased with the outdoor temperature. It was observed that the slope of the voltage curve was steeper than the slope of the power input curve. In addition, both voltage and power input curves showed a linear behavior (Figure 9). The highest power input required was around 43.70 W, and the highest voltage was 13.92 V.

Figure 10 shows the variation of the power input and the coefficient of performance with different outdoor temperatures.

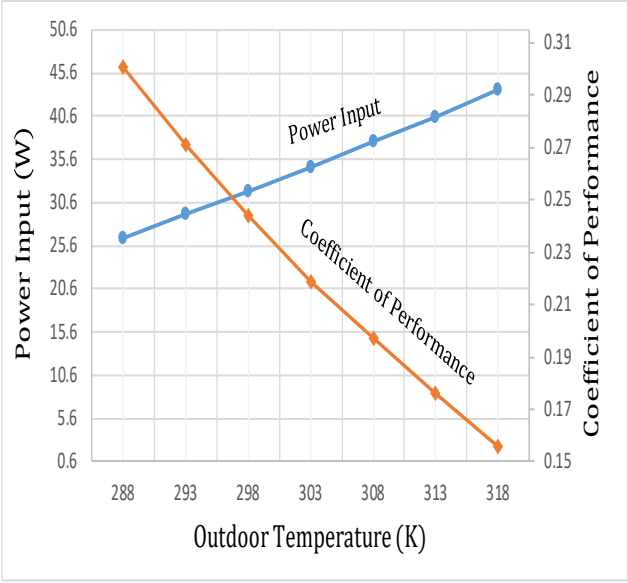

Figure 10. Power Input and Coefficient of Performance of the TEC Module at Different Outdoor Temperatures

As the outdoor temperature increased, the amount of heat gain of the volume desired to be cooled increased (Figure 10). Therefore, the cooling power absorbed by the module decreased. In this case, the required electrical energy increased as the outdoor temperature increased. As a result, the TEC required further electrical energy in summer months. Moreover, Figure 10 shows that the variation of the power input and the coefficient of performance at different outdoor temperatures was inversely proportional to each other. That is, an increasing outdoor temperature was accompanied by an increasing power input of the TEC module, but the coefficient of performance decreased. This is an expected result for the refrigeration cycle.

Figure 11 shows the variation in current and voltage for different outdoor temperatures.

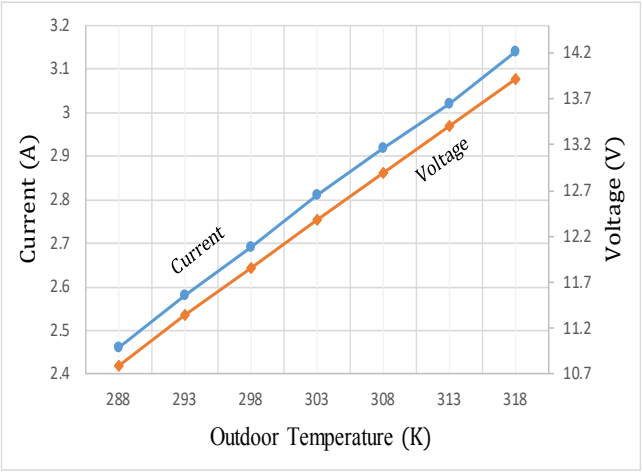

Figure 11. Current and Voltage for the TEC Module at Seven Different Outdoor Temperatures

As shown in Figure 11, the current required of the module increased with increasing outdoor temperature. This was because, as the outdoor temperature increased, the heat gain of the environment to be cooled increased. In TE cooling systems, it is known that the medium that carries the heat from the cold environment to the warm environment is the current. Therefore, as the outdoor temperature increases, the current circulating in the system is expected to increase. As a result, it was determined that the maximum current value was 3.14 A at 318 K outdoor temperature and the minimum current value was 2.46 A at 288 K (Figure 11).

As seen in Figure 11, as the outdoor temperature increased, so the voltage also had a tendency to increase. This behavior is expected in TECs. An increase in power input and current in the TEC module signifies an increase in voltage. In summary, an increase was required in the electromotive forces in these conditions. Accordingly, the maximum voltage was 13.92 V at 318 K while the minimum voltage was 10.79 V at 288 K.

Figure 12 illustrates the change in the number of TEC modules according to different outdoor temperatures.

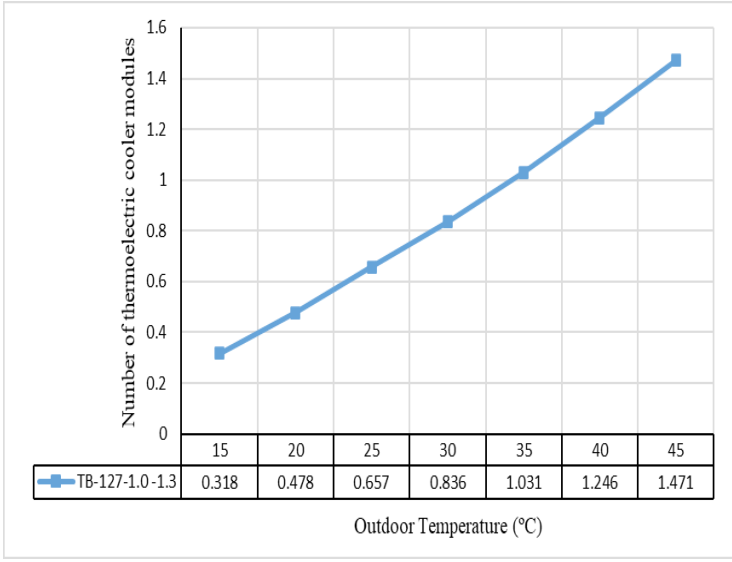

Figure 12. Number of the TEC Modules for Different Outdoor Temperatures

As the outdoor temperature increased, the number of TEC modules that required to be used in the mini refrigerator increased (Figure 12). The number of TEC modules was more than one at outdoor temperatures above about 30 °C. In other words, a single TEC module was insufficient for outdoor temperatures above approximately 30 °C, and two TEC modules were required.

5.2 Results Concerning Dimensionless Parameters

In this section, the changes in Q_1^*, W^*, COP, T_1^* and T_2^* and according to the incrementally entered and values of the optimized TB-127-1.0-1.3 are shown in Figure 13a–c, respectively.

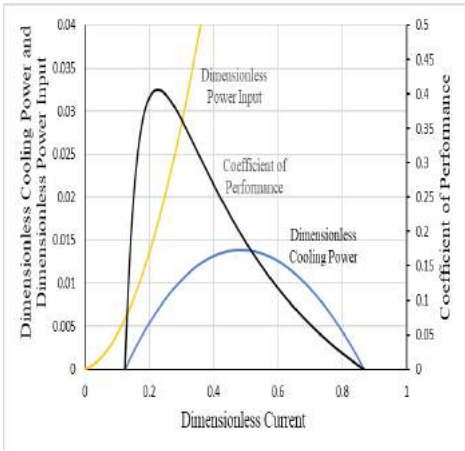

(a)

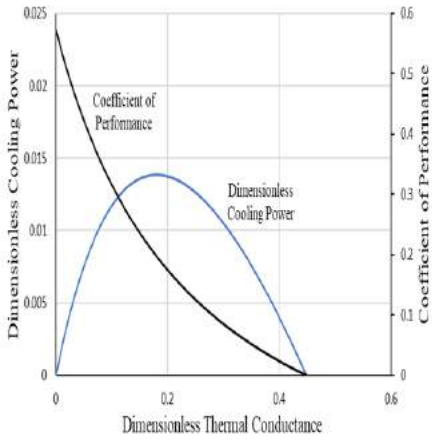

(b)

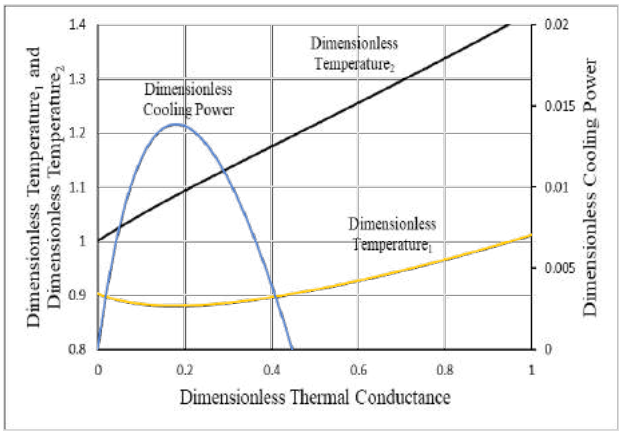

(c)

Figure 13. (a) Change of Dimensionless Cooling Power, Power Input, and Coefficient of Performance according to Dimensionless Current (b) Change of Dimensionless Cooling Power and Coefficient of Performance with Dimensionless Thermal Conductance (c) Effect of Dimensionless Thermal Conductance on Dimensionless Temperatures and Dimensionless Cooling Power

These graphs were created according to the optimum values N_k = 0.18, N_l = 0.485, N_h = 0.626, T_∞^* = 0.902 and $ZT_{\infty 2}$ = 0.805 for outdoor temperature $T_{\infty 2}$ = 35°C. *It can be seen that the optimum design parameter curves in Figure 13 and the optimum design parameter curves shown in the Reference (Lee, 2017) are in agreement.* For the outdoor temperature of 35 °C, it was observed that with the increase of the dimensionless current (N_l), there was no cooling up to 0.137 of the

(N_I), and the cooling started when the value reached 0.137 (Figure 13a). This may be due to the fact that the electrical power consumed by the module was not sufficient for the required cooling power until it reached N_I = 0.137. It can also be seen in Figure 13a that the value of dimensionless cooling power is not the maximum at the maximum coefficient of performance value. This is an expected result in TEC modules. This is because, as seen in Figure 13a, it is known that the cooling power is ineffective at the point where the coefficient of performance value is at the maximum and in some cases it is almost negligible (Lee, 2017). In addition, the maximum coefficient of performance value was obtained when the dimensionless power input and dimensionless cooling power curves were closest to each other (Figure 13a).

In TECs, it is known that the optimum cooling power is a function of the current. However, there is no information in the literature that there is an optimal dimensionless thermal conductance (N_k) value in TE cooling systems (Lee, 2017). As seen in Figure 13b, when the value is higher than 0.48, the cooling power reaches zero. That is, when N_k is greater than 0.48, there is no cooling.

It is known that the lowest dimensionless temperature T_1^* value occurs not at the highest coefficient of performance, but at the highest dimensionless cooling power (Lee, 2017). Figure 13c also shows that, at the point where T_1^* value is minimum, dimensionless cooling power reaches its maximum value. In addition, for a specific outdoor temperature, the surface temperature of the cold side of the TEC takes the lowest value at the minimum value of T_1^* . This situation can be easily seen in Equation (27). In this case, considering that the $T_{\infty 1}$ (the cold ambient temperature) value is always constant and 5 °C, it can be concluded that the maximum heat is absorbed when the cold surface temperature is at a minimum.

5.3 Results Concerning Variation of the Performance of the TB-127-1.0-1.3 with Fin Thickness and Spacing

Figure 14 illustrates the change of the performance of the TB-127-1.0-1.3 with the fin thickness.

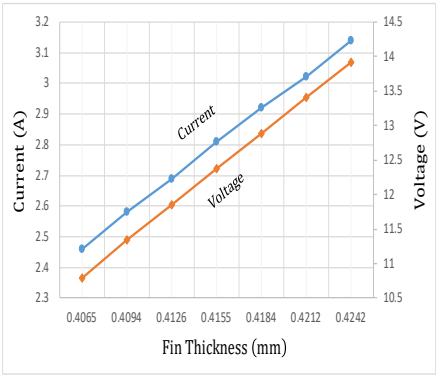

(a)

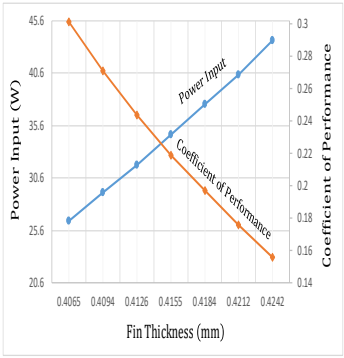

(b)

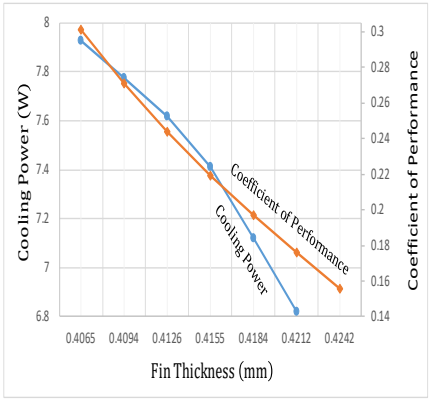

(c)

Figure 14. Effect of the Fin Thickness on Performance of TEC Module: (a) Current and Voltage (b) Power Input and Coefficient of Performance (c) Cooling Power and Coefficient of Performance

Current, voltage and power input increased with an increasing fin thickness, but cooling power and coefficient of performance decreased (Figure 14). That is, as the fin thickness increased, the temperature difference (ΔT) between the cold (T_1) and hot (T_2) surface of the module increased. Therefore, the cooling power absorbed by the module decreased. In addition, a linear behavior was observed in the changes of current, voltage, power input and coefficient of performance with fin thickness. However, this linear behavior was not observed for cooling power. The change of cooling power with fin thickness was slower up to 0.4155 mm fin thickness, and quicker after 0.4155 mm fin thickness.

The change of the performance of the TEC module with the fin spacing is also illustrated in Figure 15.

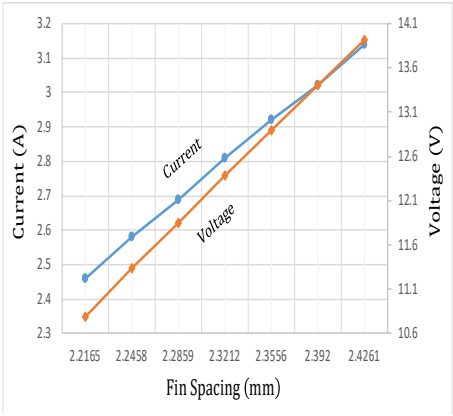

(a)

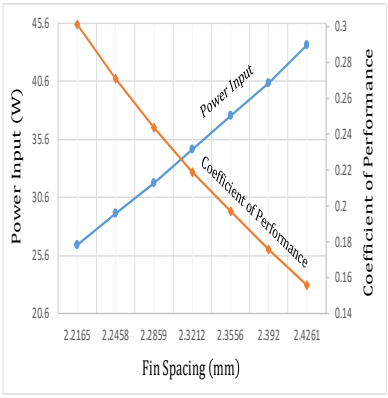

(b)

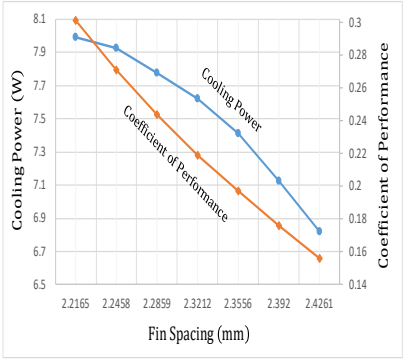

(c)

Figure 15. Effect of the Fin Spacing on Performance of TEC Module: (a) Current and Voltage (b) Power Input and Coefficient of Performance (c) Cooling Power and Coefficient of Performance

As with the fin thickness, the current, voltage and power input increased with the increasing fin spacing, but the cooling power and performance coefficient decreased (Figure 15). In other words, the productivity of the TEC decreased with increasing fin thickness and spacing. This is because, as the fin thickness and spacing increased, the temperature difference between the cold and hot sur-

face of the module increased. In addition, a linear behavior was observed in the changes of current, voltage, power input and coefficient of performance with fin spacing. However, this linear behavior was not observed for cooling power.

5.4 Results on the TEG's Capacity to Operate the TEC in the Turbocharged Tractor

In his numerical study, Gürcan (2019) obtained electrical power from a TEG in a turbocharged tractor. For the same tractor and environmental conditions, it was determined that the power input required for the TEC, which was optimized in the present work, can be met by this TEG system. This situation is illustrated in Table 3.

Table 3. Providing the Power Input Required for the TEC Using a TEG System

(K)	Power input (W) (Present study)	Power output (W) (Gürcan, 2019)	Capacity to power (%)
288	26.54	50.71	191.07
293	29.25	46.56	159.18
298	31.87	42.62	133.73
303	34.78	38.84	111.67

The sum power output values of the TEG system illustrated in Table 3 were obtained for the 1 value of dimensionless electrical resistance.

The power input of the TEC at different outdoor temperatures can be smoothly met by the TEG system (Table 3). This means that the TEC with a TEG can be used without additional fuel consumption.

6. Conclusions

The present study performed optimization of a TEC, which was driven by a TEG system. The conclusions obtained in this numeric study are summarized below:

1) The TEC performance decreased during the summer. This is an expected result for cooling systems.
2) The maximum cooling power was obtained as 7.989 W at 288 K outdoor temperature and the minimum cooling power was 6.818 W at 318 K outdoor temperature (for a single TEC module).
3) The maximum coefficient of performance value was 0.301 at 288 K outdoor temperature and the lowest coefficient of performance value was 0.156 at 318 K.
4) The voltage and the power input increased with an increase in the electrical current.

5) The maximum current value was 3.14 A at 318 K outdoor temperature and the minimum current value was 2.46 A at 288 K.
6) With increasing outdoor temperature, the voltage increased, and the maximum voltage was 13.92 V at 318 K while the minimum voltage was 10.79 V at 288 K.
7) With increasing fin thickness and spacing, current, voltage and power input increased, but cooling power and coefficient of performance decreased.
8) The power input of the TEC at different outdoor temperatures was easily met by the TEG system.

List of Symbols

A	Cross-sectional area of thermoelements (m^2)
A_t	Sum finned surface area (m^2)
A_f	Area of the fin (m^2)
b	Fin height (m)
COP	Coefficient of performance
h	Heat convective coefficient (W/m^2K)
I	Electrical current (A)
I_{max}	Maximum electrical current (A)
k	Thermal conductivity of thermoelements (W/mK)
K	Thermal conductance (W/K)
k_{al}	Thermal conductivity of fin material (aluminum) (W/mK)
k_{air}	Thermal conductivity of air (W/mK)
k^*	Effective thermal conductivity (W/mK)
l	Leg length of thermoelements (m)
L	Length of finned structure (m)
L_c	Characteristic length of flow (m)
n	Number of thermocouples of TEC
n_f	Number of fins
N	Number of TEC modules
N_k	Dimensionless thermal conductance
N_h	Dimensionless convection
N_I	Dimensionless current
N_V	Dimensionless voltage

P_r	Prandtl number
$\dot{Q}_{1max}$	Maximum cooling power (W)
$\dot{Q}_1$	Cooling power of TEC module (W)
Q_1^*	Dimensionless rate of heat transfer on cold side
$\dot{Q}_2$	Heat liberated at the hot surface (W)
Q_2^*	Dimensionless rate of heat transfer on hot side
$\dot{Q}_t$	Sum heat transfer rate of finned structure (W)
R	Internal electrical resistance (Ω)
R_e	Reynolds number
t	Fin thickness (m)
T_1	Cold surface temperature of TEC module (K)
T_1^*	Dimensionless temperature on cold side
T_2	Hot surface temperature of TEC module (K)
T_2^*	Dimensionless temperature on hot side
$T_{\infty 1}$	Cold ambient temperature (K)
$T_{\infty 2}$	Outdoor temperature (K)
T_∞^*	Dimensionless temperature
T_{Base}	Base temperature of finned structure (K)
U_∞	Velocity of air flow (m/s)
V	Voltage (V)
V_{max}	Maximum voltage (V)
w	Width of finned structure (m)
$\dot{W}$	Power input (W)
W^*	Dimensionless power input
Z	Figure of merit (1/K)
z	Fin spacing (m)
z_{opt}	Optimum fin spacing (m)
Z^*	Effective figure of merit (1/K)

Greek symbols

α	Seebeck coefficient (V/K)
α^*	Effective Seebeck coefficient (V/K)
ΔT	Temperature difference between cold and hot surface of TEC module (K)
ΔT_{max}	Maximum temperature difference (K)

η	Overall finned surface efficiency (%)
η_f	Fin efficiency (%)
ν	Kinematic viscosity (m^2/s)
ρ	Electrical resistivity (Ωm)
ρ^*	Effective electrical resistivity (Ωm)

Subscripts

1	Cold side
2	Hot side
n	n-type TE element
p	p-type TE element

Acknowledgements

The authors are thankful to the Pamukkale University Scientific Research Projects Council (Report No. 2018FEBE035) for providing financial support to conduct Gürcan (2019)'s Master Thesis.

Conflict of Interest

No conflict of interest is declared by the authors.

Contribution of Researchers

Author 1 carried out the necessary numerical analyses according to the purpose of the study. In addition, according to the results obtained, graphs showing the relationships between important parameters were created and interpreted by Author 1. Author2 created the design and operating conditions of the system and identified the important parameters that should be found. She also enabled the creation of graphs between important parameters and made scientific interpretations and scenarios of the resulting changes. Author 3 performed the necessary numerical analysis and determined the results regarding important parameters.

References

Attar, A., Lee, H., & Weera, S. (2015). Experimental Validation of the Optimum Design of an Automotive Air-to-Air Thermoelectric Air Conditioner (TEAC). *Journal of Electronic Materials,* 44, 2177–2185. Doi: https://doi.org/10.1007/s11664-015-3750-4

Arıcıoğlu, A. K. (2021). *The use of electric energy obtained from thermoelectric gen-*

erator in thermoelectric coolers of different sizes (M.Sc. dissertation). Department of Mechanical Engineering, Pamukkale University, Denizli, Turkey.

Cheng, Y.-H., & Lin, W.-K. (2005). Geometric optimization of thermoelectric coolers in a confined volume using genetic algorithms. *Applied Thermal Engineering,* 25, 2983–2997. Doi: https://doi.org/10.1016/j.applthermaleng.2005.03.007

Chen, L., Meng, F., & Sun, F. (2012). Effect of heat transfer on the performance of thermoelectric generator-driven thermoelectric refrigerator system. *Cryogenics,* 52, 58-65. Doi: https://doi.org/10.1016/j.cryogenics.2011.10.007

Chen, W.-H., Wang, C.-C., & Hung, C.-I. (2014). Geometric effect on cooling power and performance of an integrated thermoelectric generation-cooling system. *Energy Conversion and Management,* 87, 566–575. Doi: https://doi.org/10.1016/j.enconman.2014.07.054

Chen, W.-Y., Shi, X.-L., Zou, J., & Chen, Z.-G. (2022). Thermoelectric coolers for on-chip thermal management: Materials, design, and optimization. *Materials Science & Engineering R-Reports,* 151, 100700. Doi: https://doi.org/10.1016/j.mser.2022.100700

Feng, Y., Chen, L., Meng, F., & Sun, F. (2018). Thermodynamic Analysis of TEG-TEC Device Including Influence of Thomson Effect. *Journal of Non-Equilibrium Thermodynamics,* 43, 75–86. Doi: https://doi.org/10.1515/jnet-2017-0029

Gonzalez-Hernandez, S. (2020). Unification of optimization criteria and energetic analysis of a thermoelectric cooler and heater. *Physica A: Statistical Mechanics and Its Applications,* 555, 124700. Doi: https://doi.org/10.1016/j.physa.2020.124700

Gürcan, A., & Yakar, G. (2022). Investigation of the performance of a thermoelectric generator system utilizing the thermal energy of air compressed in a compressor. *Journal of the Korean Physical Society,* 80, 467–483. Doi: https://doi.org/10.1007/s40042-022-00425-x

Gürcan, A., & Yakar, G. (2022). Improving the performance of a thermoelectric generator system utilizing the thermal energy of air compressed in the compressor of a turbocharged tractor based on different-sized modules. *Journal of the Brazilian Society of Mechanical Sciences and Engineering,* 44, 360. Doi: https://doi.org/10.1007/s40430-022-03656-y

Gürcan, A. (2019). Recovery of exhaust heat energy using thermoelectric generators in different sizes (M.Sc. dissertation). Department of Mechanical Engineering, *Pamukkale University,* Denizli, Turkey.

Hasani, M., & Rahbar, N. (2015). Application of thermoelectric cooler as a power generator in waste heat recovery from a PEM fuel cell – An experimental study. *International Journal of Hydrogen Energy,* 40, 15040–15051. Doi: https://doi.org/10.1016/j.ijhydene.2015.09.023

Huang, Y., Chen, Z., & Ding, H. (2021). Performance optimization of a two-stage parallel thermoelectric cooler with inhomogeneous electrical conductivity. *Applied Thermal Engineering,* 192, 116696. Doi: https://doi.org/10.1016/j.applthermaleng.2021.116696

Khattab, N. M., & El Shenawy, E. T. (2006). Optimal operation of thermoelectric cooler driven by solar thermoelectric generator. *Energy Conversion and Management,* 47, 407-426. Doi: https://doi.org/10.1016/j.enconman.2005.04.011

Kishore, R. A., Nozariasbmarz, A., Poudel, B., Sanghadasa, M., & Priya, S. (2019). Ultra-high performance wearable thermoelectric coolers with less materials. *Nature Communications,* 10, 1765. Doi: https://doi.org/10.1038/s41467-019-09707-8

Kwan, T. H., Gao, D., Zhao, B., Ren, X., Hu, T., Dabwan, Y. N., & Pei, G. (2021). Integration of radiative sky cooling to the photovoltaic and thermoelectric system for improved space cooling. *Applied Thermal Engineering,* 196, 117230. Doi: https://doi.org/10.1016/j.applthermaleng.2021.117230

Kryotherm, (2018). Access address: http://kryothermtec.com/catalogs.html.

Lin, L., Zhang, Y.-F., Liu, H.-B., Meng, J.-H., Chen, W.-H., & Wang, X.-D. (2019). A new configuration design of thermoelectric cooler driven by thermoelectric generator. *Applied Thermal Engineering,* 160, 114087. Doi: https://doi.org/10.1016/j.applthermaleng.2019.114087

Lu, T., Li, Y., Zhang, J., Ning, P., & Niu, P. (2020). Cooling and Mechanical Performance Analysis of a Trapezoidal Thermoelectric Cooler with Variable Cross-Section. *Energies,* 13, 6070. Doi: https://doi.org/10.3390/en13226070

Lee, H. S. (2010). *Thermal design: heat sinks, thermoelectrics, heat pipes, compact heat exchangers, and solar cells.* Hoboken, NJ: Wiley.

Lee, H. S. (2017). *Thermoelectrics: design and materials.* Chichester: Wiley.

Meng, F. K., Chen, L. G., & Sun, F. R. (2010). Extreme working temperature differences for thermoelectric refrigerating and heat pumping devices driven by thermoelectric generator. *Journal of Energy Institute,* 83, 108-113. Doi: https://doi.org/10.1016/10.1179/014426010x12682307291506

Manikandan, S., & Kaushik, S. C. (2015). Thermodynamic studies and max-

imum power point tracking in thermoelectric generator–thermoelectric cooler combined system. *Cryogenics,* 67, 52–62. Doi: https://doi.org/10.1016/10.1016/j.cryogenics.2015.01.008

Nemati, A., Nami, H., Yari, M., & Ranjbar, F. (2018) Effect of geometry and applied currents on the exergy and exergoeconomic performance of a two-stage cascaded thermoelectric cooler. *International Journal of Refrigeration,* 85, 1–12. Doi: https://doi.org/10.1016/10.1016/j.ijrefrig.2017.09.006

Qiu, C., & Shi, W. (2020). Comprehensive modeling for optimized design of a thermoelectric cooler with non-constant cross-section: Theoretical considerations. *Applied Thermal Engineering,* 176, 115384. Doi: https://doi.org/10.1016/10.1016/j.applthermaleng.2020.115384

Sun, D., Liu, G., Shen, L., Chen, H., Yao, Y., & Jin, S. (2019). Modeling of high power light-emitting diode package integrated with micro-thermoelectric cooler under various interfacial and size effects. *Energy Conversion and Management,* 179, 81–90. Doi: https://doi.org/10.1016/j.enconman.2018.10.063

Sadighi Dizaji, H., Jafarmadar, S., Khalilarya, S., & Pourhedayat, S. (2019). A comprehensive exergy analysis of a prototype Peltier air-cooler; experimental investigation. *Renewable Energy,* 131, 308–317. Doi: https://doi.org/10.1016/j.renene.2018.07.056

Shen, L., Zhang, W., Liu, G., Tu, Z., Lu, Q., Chen, H., & Huang, Q. (2020). Performance enhancement investigation of thermoelectric cooler with segmented configuration. *Applied Thermal Engineering,* 168, 114852. Doi: https://doi.org/10.1016/j.applthermaleng.2019.114852

Sun, D., Shen, L., Niu, B., Gao, C., Zhou, P., Tang, J., … Yang, L. (2022). Active thermal management of hotspot under thermal shock based on micro-thermoelectric cooler and bi-objective optimization. *Energy Conversion and Management,* 252, 115044. Doi: https://doi.org/10.1016/j.enconman.2021.115044

Tian, X.-X., Asaadi, S., Moria, H., Kaood, A., Pourhedayat, S., & Jermsittiparsert, K. (2020). Proposing tube-bundle arrangement of tubular thermoelectric module as a novel air cooler. *Energy,* 208, 118428. Doi: https://doi.org/10.1016/j.energy.2020.118428

Zhang, H., Kong, W., Dong, F., Xu, H., Chen, B., & Ni, M. (2017). Application of cascading thermoelectric generator and cooler for waste heat recovery from solid oxide fuel cells. *Energy Conversion and Management,* 148, 1382–1390. Doi: https://doi.org/10.1016/j.enconman.2017.06.089

Mühendis ve Makina / Engineer and Machinery
https://dergipark.org.tr/tr/pub/muhendismakina

BİR MOBİL SİLAH PLATFORMUNDA SÜSPANSİYON SİSTEMİNİN ATIŞ KALİTESİNE ETKİSİNİN DEĞERLENDİRİLMESİ

Cem ONAT[1*], Berk TOPÇUOĞLU[2], Umut ARDA[3], Mustafa AKTEMUR[4]

[1] Adıyaman Üniversitesi, Mühendislik Fakültesi, Makine Mühendisliği Bölümü, Adıyaman ORCID No : http://orcid.org/0000-0002-4295-4860

[2] HEMA Endüstri A.Ş. ARGE Merkezi, Gazi Osman Paşa Mah., 4. Cad., No:5, Çerkezköy/ Tekirdağ, ORCID No : http://orcid.org/0009-0002-1514-0914

[3] HEMA Endüstri A.Ş. ARGE Merkezi, Gazi Osman Paşa Mah., 4. Cad., No:5, Çerkezköy/ Tekirdağ, ORCID No : http://orcid.org/0009-0009-1164-5414

[4] HEMA Endüstri A.Ş. ARGE Merkezi, Gazi Osman Paşa Mah., 4. Cad., No:5, 59500, Çerkezköy/Tekirdağ, ORCID No : http://orcid.org/0009-0009-2025-2479

Anahtar Kelimeler

Süspansiyon sistemi, titreşim, tam taşıt modeli, doğrusal olmayan model

Öz

Bu çalışmada, üzerinde seri atış yapabilen bir silah taşıyan 6X6 silah platformunda süspansiyon sisteminin atış kalitesine etkisi incelenmiştir. Bu amaçla, gövdesine rijit olarak bağlanmış bir silah bulunan askeri aracın atış sırasında oluşan geri tepme kuvvetlerini de kapsayan dokuz serbestlik dereceli tam taşıt modeli kurulmuştur. Operasyon sırasında cephane ve yakıt tüketimine bağlı olarak aracın kütle değerinin ve ağırlık merkezinin yerinin değişmesi modelde hesaba katılmıştır. Farklı atış senaryolarında yapılan simülasyonlar ile birim zamanda yapılabilecek maksimum atış sayısı tespit edilmiştir.

* conat@adiyaman.edu.tr
doi : 10.46399/muhendismakina.1422802

EVALUATION ON THE EFFECT OF SUSPENSION SYSTEM TO POINTING QUALITY IN A MOBİL WEAPON PLATFORM

Keywords

Suspension system, vibration, full car model, nonlinear modelling

Abstract

In this study, the effect of the suspension system on the shooting quality of the 6X6 gun platform carrying a gun has been examined. For this purpose, a nine-degree-of-freedom full vehicle model was established, which also includes the recoil forces that occur during firing of a military vehicle with a cannon rigidly attached to its body. The change in mass value and center of gravity of the vehicle due to ammunition and fuel consumption during operation is taken into account in the model. The maximum number of shots that can be fired per unit time was determined through simulations made in different shooting scenarios.

Araştırma Makalesi			Research Article		
Başvuru Tarihi	:	20.01.2024	Submission Date	:	20.01.2024
Kabul Tarihi	:	26.03.2024	Accepted Date	:	26.03.2024

Extended Abstract

It is no doubt, vehicles with a good suspension system provide superior performance in different road and operating conditions. Suspension systems in civilian vehicles are designed to offer an appropriate trade-off between roadholding and comfort performance indicators. In addition to these two main performances, the suspension deflection performance indicator, which is a constructive constraint, is another indicator that should be taken into consideration by engineers. In military vehicles intended for personnel-material transfer, comfort performance is ignored and designs focused on handling performance are in question. However, if there is a weapon system on the body of the military vehicle, the suspension system must be designed by taking into account the vehicle body vibrations. Even if the vehicle is stationary, the recoil forces resulting from the shots will cause vibrations in the vehicle body. The resulting body vibrations will also negatively affect the rapid shooting quality.

In this study, the suspension system of a 6x6 unmanned ground vehicle carrying a rapid-firing weapon system on its body was designed. This study differs from the 6x6 full vehicle model previously examined in the literature in two different aspects. First, a model based on fuel and ammunition consumption was used. The second is to integrate the recoil force and related reaction moments during firing of the weapon system into the model and examine the effect of the suspension system on the shooting quality.

The weapon system can move around the vertical axis in the range of [0o 360o] and around the horizontal axis in the range of [-20o 40o]. In the study, firstly, a full vehicle model with nine degrees of freedom was established. In the model, the body mass, mass moments of inertia and the change in the center of gravity of the vehicle when fuel and ammunition are fully loaded and empty are taken into account. The recoil force resulting from gun shots and the resulting reaction moments are also taken into account in the model.

The system model was built on the physical model created by considering that each wheel-axle assembly moves only vertically, and the vehicle body makes a total of three movements: vertical, heading and yawing. Nine interconnected differential equations forming the system model were solved with the analysis block created in the Matlab-Simulink environment. Simulations were made in two different categories. In the first category of simulations, the vehicle was passed through a sinusoidal bump. Thus, the performance of the suspension system is demonstrated. In the second category of simulations, the shooting error due to the recoil force of the weapon system in different firing situations was revealed. Suspension performance is revealed through the vertical displacement of the vehicle body (x1), suspension deflection of the front right wheel (sd1) and wheel deformation (td1). Accordingly, the bump road response of the vehicle in empty condition is given in Figure 3.

There is no lower limit for the shooting period. The operator can set the firing period any way below the upper limit. The reaction force resulting from each shot is 10 kN and the reaction time is 0.1 s. The situations to be used in the simulation set are given in Table 3. Accordingly, this simulation category will consist of a total of 36 simulation sets. Numbering of the simulation sets was done using row and column numbers, respectively.

The main factor that will determine the quality of the shot will be the vehicle body vibrations that will occur due to the recoil force during the shots. For this purpose, considering simulation sets 22 and 34 will be sufficient for the purpose of the study. The body vibrations in simulation set number 22 are given in Figure 7. In this case, since the barrel is in the direction of vehicle advancement, the recoil force does not cause wobbling. In this respect, the ϒ=180o position is a suitable position for aiming quality. However, head impact vibrations adversely affect the aiming quality and cause errors.

As a result of the study, the shooting quality capacity of the vehicle in 36 different situations was revealed. Accordingly, the shooting quality is completely dependable depending on the suspension system. Moreover, and more importantly, the error can be predicted through the suspension system model in response to the number of shots per unit time parameter. Aiming assistant systems can be developed for this purpose. Another conclusion from the article is that in order to achieve a full hit from the current platform, a shot must be fired every 4 seconds at most. Systems that aim at moving targets may be studied in future studies.

1. Giriş

Şüphesiz ki iyi bir süspansiyon sistemine sahip taşıtlar farklı yol ve işletme şartlarında üstün performans sağlarlar. Şimdiye kadar pasif, yarı-aktif ve aktif süspansiyon sistemleri için birçok tasarım ve uygulama çalışması yapılmıştır (Ozbek, Burkan ve Yagiz 2020; Yagiz, 2004). Bu çalışmalar aktif ya da yarı-aktif kontrol mimarisi için kontrolcü tasarımına yöneliktir ve taşıt titreşimlerinin etüdüne yönelik araştırmacılar için oldukça kıymetlidir. Sivil amaçlı taşıtlarda süspansiyon sistemi yol tutuş ve konfor performans göstergeleri arasında uygun bir ödünleşme sunacak şekilde tasarlanırlar (Onat, Küçükdemiral, Sivrioğlu ve Yüksek, 2007; Onat, Küçükdemiral, Sivrioğlu, Yüksek ve Cansever, 2009; Ping, Wang ve Zhang, 2018). Bu iki ana performansın yanında konstrüktif bir kısıt olan süspansiyon sapması performans göstergesi de yine mühendisler için göz önüne alınması gereken bir başka göstergedir (Nguyen ve Nguyen, 2023). Personel-malzeme intikali amaçlı askeri araçlarda konfor performansı göz ardı edilerek yol tutuş performansı odaklı tasarımlar söz konusu olmaktadır (Demir, 2003). Ancak askeri aracın gövdesi üzerinde bir silah sistemi mevcutsa taşıt gövde titreşimlerinin de mutlaka göz önüne alınarak süspansiyon sisteminin tasarlanması gerekir. Zira taşıt duruyor olsa bile atışlardan kaynaklanan geri tepme kuvvetleri taşıt gövdesinde titreşimlere sebep olacaktır. Oluşan gövde titreşimleri de seri atış kalitesini olumsuz yönde etkileyecektir.

Bu çalışmada, gövdesi üzerinde seri atış yapabilen bir silah sistemi taşıyan 6x6 mobil silah platformunun süspansiyon sistemi tasarlanmıştır. Demir, taşıtın seyir ve atış durumlarındaki dinamik ve gerilme analizleri teorik ve deneysel olarak yapmıştır (Demir, 2003). Ancak ele alınan askeri taşıt havan topu taşıdığından herhangi bir şekilde atış kalitesine ilişkin hesaba yer verilmemiştir. Zira havan topu seri atış yapmaz ve kaba olarak hedef gözetir. Seri atış yapabilen ve havan topuna göre oldukça düşük çaplı silahlarda iyi bir nişan kalitesi beklenir. Literatürde daha önce incelenmiş 6x6 tam taşıt modelinden üç farklı hususta bu çalışma ayrılmaktadır. Bunlardan birincisi yakıt ve cephane tüketimine bağlı bir model kullanılmıştır. İkincisi, taşıt üzerinde seri halde atış yapabilen silah sistemi taşımaktadır. Sonuncusu ise silah sisteminin atışı sırasında geri tepme kuvveti ve buna bağlı tepki momentlerinin de modele entegre edilmesi ve süspansiyon sisteminin atış kalitesine etkisinin incelenmesidir.

Silah sistemi düşey eksen etrafında [0^o 360^o], yatay eksen etrafında [-20^o 40^o] aralığında hareket edebilmektedir. Çalışmada, ilk olarak, dokuz serbestlik dereceli tam taşıt modeli kurulmuştur. Modelde taşıtın yakıt ve cephane tam dolu ve boş durumlarındaki gövde kütlesi, kütlesel atalet momentleri ve ağırlık merkezinin değişimi hesaba katılmıştır. Silah atışlarından kaynaklı geri tepme kuvveti ve buna bağlı ortaya çıkan tepki momentleri de modelde göz önüne alınmıştı.

2. Modelleme

Sistem modeli her bir tekerlek-aks aksamının sadece düşey hareket yaptığı, taşıt gövdesinin de düşey, kafa vurma ve yalpalama olmak üzere toplam üç hareket yaptığı düşünülerek oluşturulan fiziksel model üzerinden kurulmuştur. Tam taşıt modeli Şekil 1'de verilmektedir. Burada kullanılan semboller ve anlamları Tablo 1'de sunulan adlar dizininde verilmektedir. Ayrıca belirtilmesi gerekir ki "bu çalışmada araştırma ve yayın etiğine uyulmuştur".

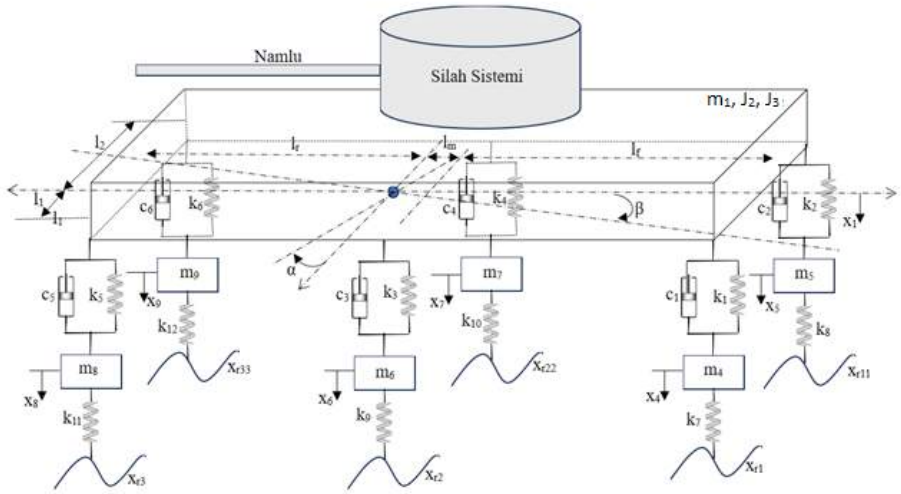

Şekil 1. Mobil Platformun Fiziksel Modeli

Tablo 1. Adlar Dizini

Sembol	Ad
m_1	Gövde kütlesi
J_2	Kafa vurma hareketi için kütlesel atalet
J_3	Yalpalama hareketi için kütlesel atalet
x_1, α, β, x_4, x_5, x_6, x_7, x_8, x_9	Sistem durum değişkenleri (deplasmanlar)
x_{r1}, x_{r11}, x_{r2}, x_{r22}, x_{r3}, x_{r33}	Yol girişleri
k_1, k_2, k_3, k_4, k_5, k_6	Süspansiyon yay katsayıları
k_7, k_8, k_9, k_{10}, k_{11}, k_{12}	Tekerlek rijitlik katsayıları
c_1, c_2, c_3, c_4, c_5, c_6	Süspansiyon sönüm katsayıları
F_t, F_{tx}, F_{ty}, F_{tz}	Tepki kuvveti ve bileşenleri
M_t, M_{tx}, M_{ty}, M_{tz}	Tepki momenti ve bileşenleri

l_1	Sol tekerlek izine ağırlık merkezinin dik uzaklığı
l_2	Sağ tekerlek izine ağırlık merkezinin dik uzaklığı
l_f	Ön aksın ağırlık merkezine dik uzaklığı
l_r	Arka aksın ağırlık merkezine dik uzaklığı
l_m	Orta aksın ağırlık merkezine dik uzaklığı
θ	Silah namlusunun yere göre açısı [-20° +40°]
Υ	Silah namlusunun tarama açısı [0° 360°]
r_x, r_y, r_z	Tepki noktasının taşıt gövdesi ağırlık merkezine göre yer vektörünün bileşenleri
T_A	Atış periyodu
L_A	Etkili menzil
E_A	Atış hatası

Altı adet tekerlek-aks sistemi düşey hareketi ve üç adet de gövde hareketi olmak üzere sistem dokuz serbestlik derecelidir. Sistemin diferansiyel denklemleri D'Alembert prensibi ile elde edilmiştir ve Denklem 1-9'da verilmektedirler. Değişkenlerin üzerindeki her bir noktanın zamana göre bir türevi ifade ettiğine dikkat ediniz.

$$
\begin{aligned}
&m_1\ddot{x}_1 + k_2\left(x_1 + l_f\sin(\beta) + l_2\sin(\alpha) - x_5\right) + c_2\left(\dot{x}_1 + l_f\,\dot{\beta}\cos(\beta) + l_2\dot{\alpha}\cos(\alpha) - \dot{x}_5\right) + \\
&k_4(x_1 + l_m\sin(\beta) + l_2\sin(\alpha) - x_7) + c_4\left(\dot{x}_1 + l_m\,\dot{\beta}\cos(\beta) + l_2\dot{\alpha}\cos(\alpha) - \dot{x}_7\right) + \\
&k_6(x_1 - l_r\sin(\beta) + l_2\sin(\alpha) - x_9) + c_6\left(\dot{x}_1 - l_r\,\dot{\beta}\cos(\beta) + l_2\dot{\alpha}\cos(\alpha) - \dot{x}_9\right) + \\
&k_1\left(x_1 + l_f\sin(\beta) - l_1\sin(\alpha) - x_4\right) + c_1\left(\dot{x}_1 + l_f\,\dot{\beta}\cos(\beta) - l_1\dot{\alpha}\cos(\alpha) - \dot{x}_4\right) + \\
&k_3(x_1 + l_m\sin(\beta) - l_1\sin(\alpha) - x_6) + c_3\left(\dot{x}_1 + l_m\,\dot{\beta}\cos(\beta) - l_1\dot{\alpha}\cos(\alpha) - \dot{x}_6\right) + \\
&k_5(x_1 - l_r\sin(\beta) - l_1\sin(\alpha) - x_8) + c_5\left(\dot{x}_1 - l_r\,\dot{\beta}\cos(\beta) - l_1\dot{\alpha}\cos(\alpha) - \dot{x}_8\right) + F_{ty} = 0
\end{aligned}
\tag{1}
$$

$$
\begin{aligned}
&J_2\ddot{\beta} + l_f k_2\left(x_1 + l_f\sin(\beta) + l_2\sin(\alpha) - x_5\right) + l_f c_2\left(\dot{x}_1 + l_f\,\dot{\beta}\cos(\beta) + l_2\dot{\alpha}\cos(\alpha) - \dot{x}_5\right) + \\
&l_m k_4(x_1 + l_m\sin(\beta) + l_2\sin(\alpha) - x_7) + l_m c_4\left(\dot{x}_1 + l_m\,\dot{\beta}\cos(\beta) + l_2\dot{\alpha}\cos(\alpha) - \dot{x}_7\right) - \\
&l_r k_6(x_1 - l_r\sin(\beta) + l_2\sin(\alpha) - x_9) - l_r c_6\left(\dot{x}_1 - l_r\,\dot{\beta}\cos(\beta) + l_2\dot{\alpha}\cos(\alpha) - \dot{x}_9\right) + l_f k_1 \\
&\left(x_1 + l_f\sin(\beta) - l_1\sin(\alpha) - x_4\right) + l_f c_1\left(\dot{x}_1 + l_f\,\dot{\beta}\cos(\beta) - l_1\dot{\alpha}\cos(\alpha) - \dot{x}_4\right) + l_m k_3 \\
&(x_1 + l_m\sin(\beta) - l_1\sin(\alpha) - x_6) + l_m c_3\left(\dot{x}_1 + l_m\,\dot{\beta}\cos(\beta) - l_1\dot{\alpha}\cos(\alpha) - \dot{x}_6\right) - \\
&l_r k_5(x_1 - l_r\sin(\beta) - l_1\sin(\alpha) - x_8) - l_r c_5\left(\dot{x}_1 - l_r\,\dot{\beta}\cos(\beta) - l_1\dot{\alpha}\cos(\alpha) - \dot{x}_8\right) + M_{tz} = 0
\end{aligned}
\tag{2}
$$

$$J_3\ddot{\alpha} + l_2k_2\left(x_1 + l_f\sin(\beta) + l_2\sin(\alpha) - x_5\right) + l_2c_2\left(\dot{x}_1 + l_f\dot{\beta}\cos(\beta) + l_2\dot{\alpha}\cos(\alpha) - \dot{x}_5\right) +$$
$$l_2k_4(x_1 + l_m\sin(\beta) + l_2\sin(\alpha) - x_7) + l_2c_4\left(\dot{x}_1 + l_m\dot{\beta}\cos(\beta) + l_2\dot{\alpha}\cos(\alpha) - \dot{x}_7\right) +$$
$$l_2k_6(x_1 - l_r\sin(\beta) + l_2\sin(\alpha) - x_9) + l_2c_6\left(\dot{x}_1 - l_r\dot{\beta}\cos(\beta) + l_2\dot{\alpha}\cos(\alpha) - \dot{x}_9\right) - \quad (3)$$
$$l_1k_1\left(x_1 + l_f\sin(\beta) - l_1\sin(\alpha) - x_4\right) - l_1c_1\left(\dot{x}_1 + l_f\dot{\beta}\cos(\beta) - l_1\dot{\alpha}\cos(\alpha) - \dot{x}_4\right) -$$
$$l_1k_3(x_1 + l_m\sin(\beta) - l_1\sin(\alpha) - x_6) - l_1c_3\left(\dot{x}_1 + l_m\dot{\beta}\cos(\beta) - l_1\dot{\alpha}\cos(\alpha) - \dot{x}_6\right) -$$
$$l_1k_5(x_1 - l_r\sin(\beta) - l_1\sin(\alpha) - x_8) - l_1c_5\left(\dot{x}_1 - l_r\dot{\beta}\cos(\beta) - l_1\dot{\alpha}\cos(\alpha) - \dot{x}_8\right) + M_{tx} = 0$$

$$m_4\ddot{x}_4 - k_1\left(x_1 + l_f\sin(\beta) - l_1\sin(\alpha) - x_4\right) - c_1\left(\dot{x}_1 + l_f\dot{\beta}\cos(\beta) - l_1\dot{\alpha}\cos(\alpha) - \dot{x}_4\right) + k_7(x_4 - x_{r1}) = 0 \quad (4)$$

$$m_5\ddot{x}_5 - k_2\left(x_1 + l_f\sin(\beta) + l_2\sin(\alpha) - x_5\right) - c_2\left(\dot{x}_1 + l_f\dot{\beta}\cos(\beta) + l_2\dot{\alpha}\cos(\alpha) - \dot{x}_5\right) + k_8(x_5 - x_{r11}) = 0 \quad (5)$$

$$m_6\ddot{x}_6 - k_3(x_1 + l_m\sin(\beta) - l_1\sin(\alpha) - x_6) - c_3\left(\dot{x}_1 + l_m\dot{\beta}\cos(\beta) - l_1\dot{\alpha}\cos(\alpha) - \dot{x}_6\right) + k_9(x_6 - x_{r2}) = 0 \quad (6)$$

$$m_7\ddot{x}_7 - k_4(x_1 + l_m\sin(\beta) + l_2\sin(\alpha) - x_7) - c_4\left(\dot{x}_1 + l_m\dot{\beta}\cos(\beta) + l_2\dot{\alpha}\cos(\alpha) - \dot{x}_7\right) + k_{10}(x_7 - x_{r22}) = 0 \quad (7)$$

$$m_8\ddot{x}_8 - k_5(x_1 - l_r\sin(\beta) - l_1\sin(\alpha) - x_8) - c_5\left(\dot{x}_1 - l_r\dot{\beta}\cos(\beta) - l_1\dot{\alpha}\cos(\alpha) - \dot{x}_8\right) + k_{11}(x_8 - x_{r3}) = 0 \quad (8)$$

$$m_9\ddot{x}_9 - k_6(x_1 - l_r\sin(\beta) + l_2\sin(\alpha) - x_9) - c_6\left(\dot{x}_1 - l_r\dot{\beta}\cos(\beta) + l_2\dot{\alpha}\cos(\alpha) - \dot{x}_9\right) + k_{12}(x_9 - x_{r33}) = 0 \quad (9)$$

Silah atışlarından kaynaklanan tepki kuvveti (F_t) bileşenlerinin silah sisteminin iki adet konum parametresine bağlı olarak ifadeleri Denklem 10-12' de verilmektedir.

$$F_{ty} = -\left|\vec{F}_t\right|\sin(\theta) \quad (10)$$

$$F_{tx} = \left|\vec{F}_t\right|\cos(\theta)\cos(\gamma) \quad (11)$$

$$F_{tz} = -\left|\vec{F}_t\right|\cos(\theta)\sin(\gamma) \quad (12)$$

Tepki kuvvetinin uygulama noktasının gövde ağırlık merkezine göre konumunu gösteren yer vektörünün bileşenleri r_x, r_y ve r_z olmak üzere tepki kuvvetinin taşıt gövdesi ağırlık merkezinde oluşturduğu moment ifadesi Denklem 13'de verildiği gibi olacaktır.

$$\vec{M}_t = (r_y F_{tz} - r_z F_{ty})\vec{i} + (r_z F_{tx} - r_x F_{tz})\vec{j} + (r_x F_{ty} - r_y F_{tx})\vec{k} \quad (13)$$

Buradan M_t tepki momentinin bileşenleri denklem 14-16'da verilmektedir.

$$M_{tx} = r_y F_{tz} - r_z F_{ty} \quad (14)$$

$$M_{ty} = r_z F_{tx} - r_x F_{tz} \quad (15)$$

$$M_{tz} = r_x F_{ty} - r_y F_{tx} \quad (16)$$

3. Simülasyonlar

Sistem modelini oluşturan birbirine bağlı dokuz adet diferansiyel denklem Matlab-Simulink ortamında oluşturulan analiz bloğu ile çözülmüştür. Analiz bloğunda, çözümler değişken adım aralığında ODE45 çözücüsüyle gerçekleştirilmiştir. Simülasyonlar iki farklı kategoride yapılmıştır. Birinci kategoride, taşıt süspansiyon sisteminin genel performansını değerlendirmek için Şekil 2'de verilen 5 cm genliğinde sinüzoidal formda bir kasis üzerinden boş ve dolu durumlarında geçirilmiştir. Bu simülasyon kategorisinde askeri taşıt atış halinde değildir. Simülasyon parametreleri Tablo 2'de verilmektedir.

Tablo 2. Simülasyon Parametreleri

Parametre	Boş durum	Dolu durum
m_1	2041,2 kg	2494,8 kg
J_2	2165,18 kgm^2	2646 kgm^2
J_3	493,67 kgm^2	603,29 kgm^2
k_1, k_2, k_3, k_4, k_5, k_6	45,36 kN/m	45,36 kN/m
k_7, k_8, k_9, k_{10}, k_{11}, k_{12}	189 kN/m	189 kN/m
c_1, c_2, c_3, c_4, c_5, c_6	1890 Ns/m	1360,8 Ns/m
l_1	0,71 m	0,78 m
l_2	0,71 m	0,64m

l_f	0,94 m	0,85 m
l_r	1,03m	1,12 m
l_m	0,45 m	0,36 m
r_x	0,25 m	0,3 m
r_y	0,81 m	0,83 m
r_z	0,0 m	0,0 m
L_A	500 m	500 m

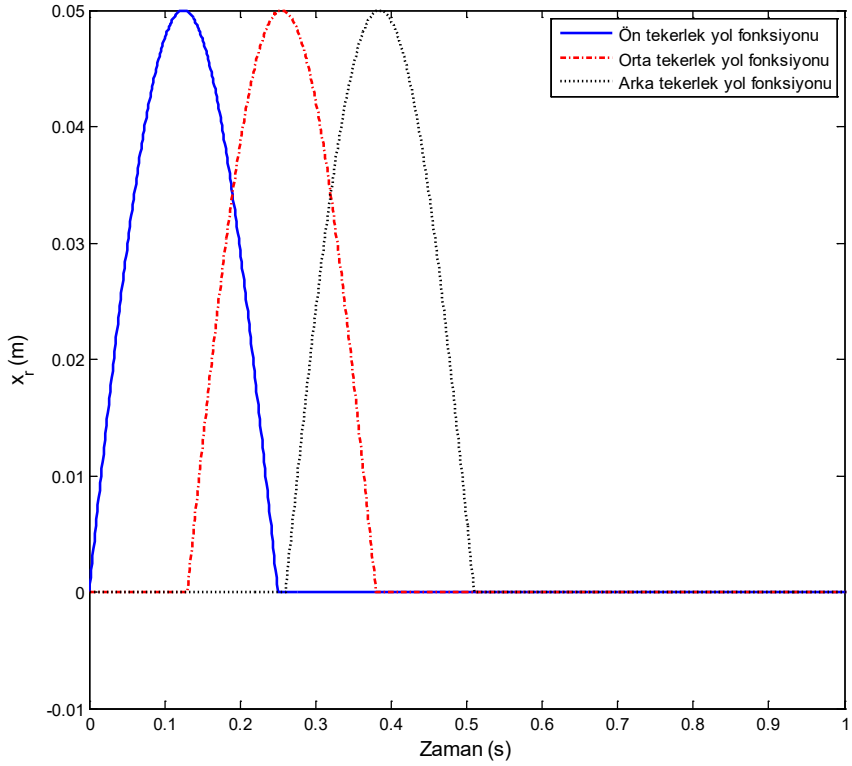

Şekil 2. Yol Fonksiyonu

Süspansiyon performansı, taşıt gövdesinin düşey deplasmanı (x_1) ön sağ tekerleğin süspansiyon sapması (sd_1) ve tekerlek deformasyonu (td_1) göstergeleri üzerinden ortaya konulmuştur. Buna göre taşıtın boş durumdaki kasis yol cevabı Şekil 3'de verilmektedir.

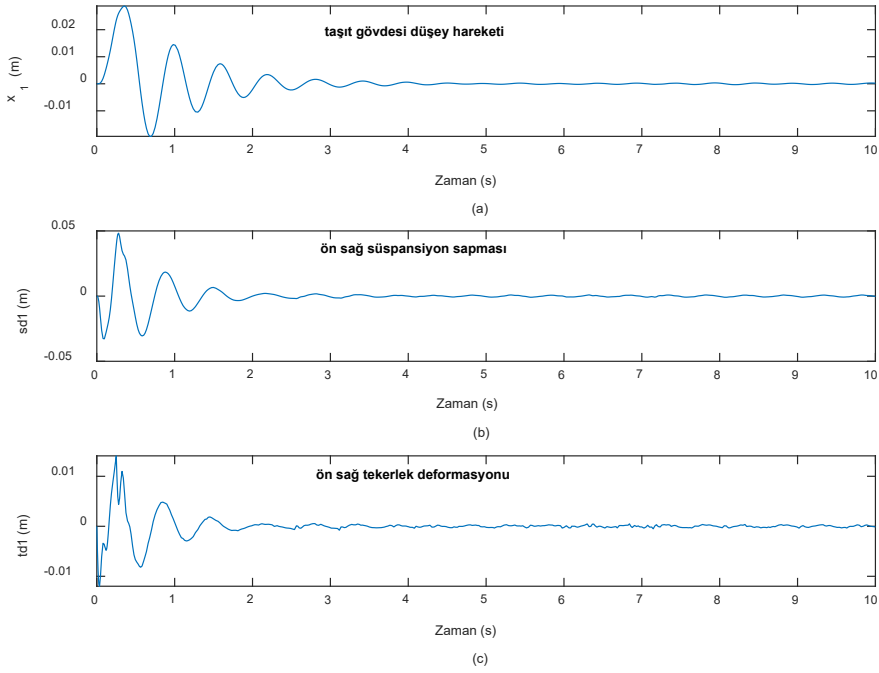

Şekil 3. Boş Durumda Kasis Yol Performansları (a) Gövde Düşey Hareketi, (b) Süspansiyon Sapması, (c) Tekerlek Deformasyonu

Şekil 3 (a)'dan, taşıt gövdesinin en fazla 2,7 cm hareket edip 4 saniye içinde titreşimli hareketinin sönümlendiği görülmektedir. Şekil 3 (b)'den, süspansiyon sapmasının maksimum değerinin 4,6 cm olduğu görülmektedir. Ortalama bir süspansiyon stroğunun ±8 cm olduğu düşünüldüğünde süspansiyon sapması makul değer aralığında kalmıştır. Şekil 3 (c)'de ise ön sağ tekerleğin deformasyonu verilmektedir. Tekerlek maksimum deformasyonunun 1,4 cm olduğu görülmektedir. Tekerleğin 1,4 cm'lik deformasyonu da yol ile temasının kesilmediğine işaret etmektedir.

Şekil 4'de taşıtın tam dolu durumunda kasisli yol cevabı verilmektedir.

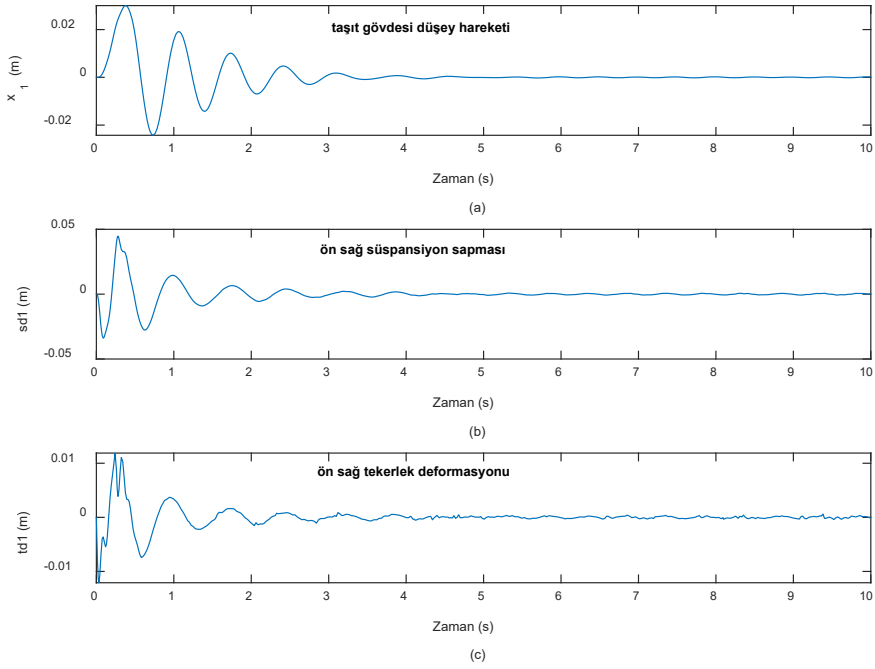

Şekil 4. Dolu Durumda Kasis Yol Performansları (a) Gövde Düşey Hareketi, (b) Süspansiyon Sapması, (c) Tekerlek Deformasyonu

Şekil 4 (a)'dan, taşıtın tam dolu durumunda, 5 cm'lik kasisten geçerken taşıt gövdesinin en fazla 2,9 cm hareket edip 4,2 saniye içinde titreşimli hareketinin sönümlendiği görülmektedir. Şekil 4 (b)'de, ön sağ süspansiyon sapması verilmektedir. Buradan, süspansiyon sapması maksimum değerinin 4,3 cm olduğu görülmektedir. Şekil 4 (c)'den, tekerlek deformasyonunun maksimum değerinin 1,4 cm olduğu görülmektedir. Söz konusu performanslar boş durumdakine yakın değerlerdedir. Ancak gövde titreşiminin boş duruma göre kötüleştiği görülmektedir.

İkinci kategori simülasyonlarda ise taşıt durağan halde atış yapmaktadır. Şekil 5'de silah sisteminin şematik üst ve yan görünüşü verilmektedir. Simülasyonlar sistemin altı farklı pozisyonunda üç farklı atış periyodu (T_A) için boş ve dolu durumlarında yapılmıştır.

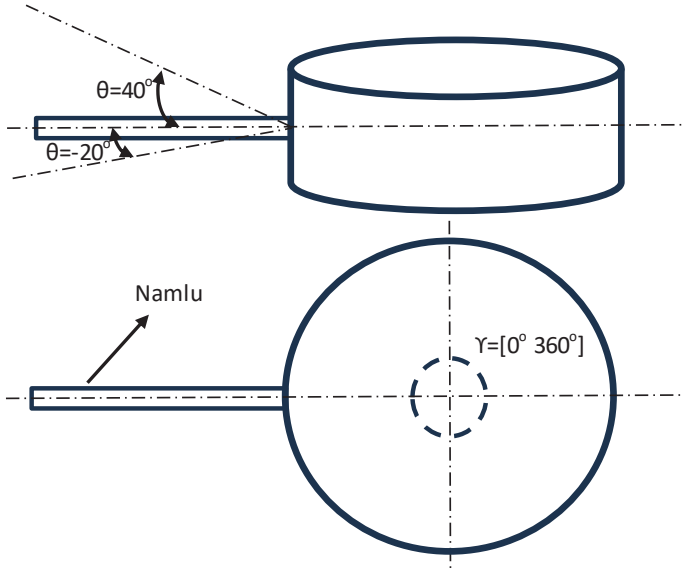

Şekil 5. Silah Sisteminin Genel Görünüşü

Atışlar seri halde en fazla saniyede iki tane olmaktadır. Şekil 6'da saniyede bir atış durumunda oluşan tepki kuvveti gösterilmektedir.

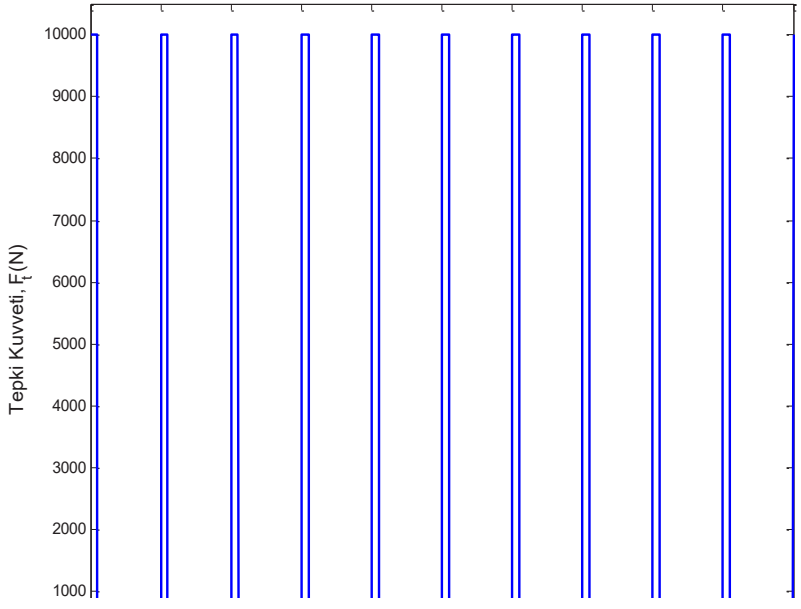

Şekil 6. 1 Atış/s Periyodu İçin Tepki Kuvveti

Atış periyodunun alt sınırı bulunmamaktadır. Operatör atış periyodunu üst sınırın altında herhangi bir şekilde belirleyebilmektedir. Her bir atıştan kaynaklı tepki kuvveti 10 kN'dır ve tepkinin süresi 0,1 s'dir. Simülasyon setinde kullanılacak durumlar Tablo 3'de verilmektedir. Buna göre bu simülasyon kategorisi toplam 36 simülasyon setinden oluşacaktır. Simülasyon setlerinin numaralandırılması sırasıyla satır ve sütun numaraları kullanılarak yapılmıştır. Örneğin 34 numaralı simülasyon seti 3. satır, 4. sütundaki namlu pozisyonu (θ=-20° Υ=225°), atış periyodu (T_A=1 Atış/s) ve yükleme durumunu (dolu) göstermektedir.

Tablo 3. Atış Kalitesi Simülasyon Seti

	1	2	3	4	5	6
1	θ=-20° Υ=180° T_A=2 Atış/s Boş durum	θ=-20° Υ=180° T_A=1 Atış/s Boş durum	θ=-20° Υ=180° T_A=0.5 Atış/s Boş durum	θ=-20° Υ=180° T_A=2 Atış/s Dolu durum	θ=-20° Υ=180° T_A=1 Atış/s Dolu durum	θ=-20° Υ=180° T_A=0.5 Atış/s Dolu durum
2	θ=40° Υ=180° T_A=2 Atış/s Boş durum	θ=40° Υ=180° T_A=1 Atış/s Boş durum	θ=40° Υ=180° T_A=0.5 Atış/s Boş durum	θ=40° Υ=180° T_A=2 Atış/s Dolu durum	θ=40° Υ=180° T_A=1 Atış/s Dolu durum	θ=40° Υ=180° T_A=0.5 Atış/s Dolu durum
3	θ=-20° Υ=225° T_A=2 Atış/s Boş durum	θ=-20° Υ=225° T_A=1 Atış/s Boş durum	θ=-20° Υ=225° T_A=0.5 Atış/s Boş durum	θ=-20° Υ=225° T_A=2 Atış/s Dolu durum	θ=-20° Υ=225° T_A=1 Atış/s Dolu durum	θ=-20° Υ=225° T_A=0.5 Atış/s Dolu durum
4	θ=40° Υ=225° T_A=2 Atış/s Boş durum	θ=40° Υ=225° T_A=1 Atış/s Boş durum	θ=40° Υ=225° T_A=0.5 Atış/s Boş durum	θ=40° Υ=225° T_A=2 Atış/s Dolu durum	θ=40° Υ=225° T_A=1 Atış/s Dolu durum	θ=40° Υ=225° T_A=0.5 Atış/s Dolu durum
5	θ=-20° Υ=270° T_A=2 Atış/s Boş durum	θ=-20° Υ=270° T_A=1 Atış/s Boş durum	θ=-20° Υ=270° T_A=0.5 Atış/s Boş durum	θ=-20° Υ=270° T_A=2 Atış/s Dolu durum	θ=-20° Υ=270° T_A=1 Atış/s Dolu durum	θ=-20° Υ=270° T_A=0.5 Atış/s Dolu durum
6	θ=40° Υ=270° T_A=2 Atış/s Boş durum	θ=40° Υ=270° T_A=1 Atış/s Boş durum	θ=40° Υ=270° T_A=0.5 Atış/s Boş durum	θ=40° Υ=270° T_A=2 Atış/s Dolu durum	θ=40° Υ=270° T_A=1 Atış/s Dolu durum	θ=40° Υ=270° T_A=0.5 Atış/s Dolu durum

Atış kalitesini belirleyecek ana faktör atışlar sırasında geri tepme kuvvetine bağlı oluşacak taşıt gövde titreşimleri olacaktır. Bu amaçla 22 ve 34 numaralı simülasyon setlerini göz önüne almak çalışmanın amacı bakımından yeterli olacaktır. 22 numaralı simülasyon setinde gövde titreşimleri Şekil 7'de verilmektedir. Şekil 7 (a)'da verilen saniyede bir seri atış durumuna karşılık gövdenin düşey, kafa vurma ve yalpalama hareketleri sırasıyla Şekil 7 (b), (c) ve (d)'de verilmektedir. Şekil 7 (b) ve (c)'de gövde düşey hareketi ve kafa vurma hareketinin yaklaşık 4 saniye kadar geçici rejim karakteristiklerinin görüldüğü ardından sürekli rejime oturduğu görülmektedir. Bu simülasyon seti durumunda, namlu taşıt ilerleme yönünde olduğundan tepme kuvveti yalpalamaya sebep olmamaktadır. Bu durum, yapılan simülasyon ve modelleme çalışmalarının doğruluğuna referans teşkil ettiği için de önemlidir. Υ=180° pozisyonu bu bakımdan nişan kalitesi için elverişli bir pozisyondur. Ancak oluşan kafa vurma titreşimleri nişan kalitesini kötü yönde etkileyerek hataya sebep olacaktır.

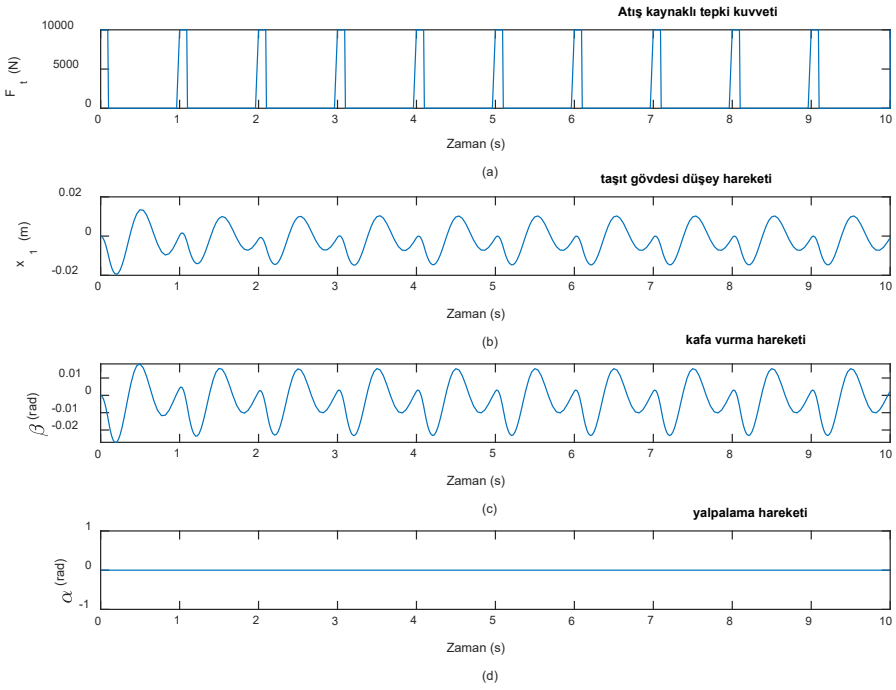

Şekil 7. 22 Numaralı Simülasyon Seti İçin (a) Tepki Kuvveti, (b) Gövde Düşey Hareketi (c) Kafa Vurma Hareketi (d) Yalpalama Hareketi

34 numaralı simülasyon seti için taşıt gövde titreşimleri Şekil 8'de verilmektedir. Bu durumda silah sistemi saniyede 2 adet atış yapmaktadır. Simülasyon süresince toplam 20 adet atış kaydedilmiştir. 34 numaralı simülasyon setinde gövde titreşimleri Şekil 8'de verilmektedir. Şekil 8 (a)'da verilen saniyede iki seri atış durumuna karşılık gövdenin düşey, kafa vurma ve yalpalama hareketleri sırasıyla Şekil 8 (b), (c) ve (d)'de verilmektedir. Namlunun açısından dolayı bu durumda yalpalama hareketi de meydana gelmektedir. Şekil 8'den, tüm gövde hareketlerinde yaklaşık 8 saniye kadar geçici rejim gözlenmektedir.

22 ve 34 numaralı simülasyon seti sonuçları taşıtın dolu ve boş durumlarda atış kalitesinin karşılaştırılmasına yönelik ikincil bir imkan da sağlamaktadır. Buna göre taşıt boş durumdayken gövde titreşimlerinin sürekli rejime girmesi daha erken olmaktadır. Bu da boş durumda daha kaliteli atış yapılabileceğini göstermektedir.

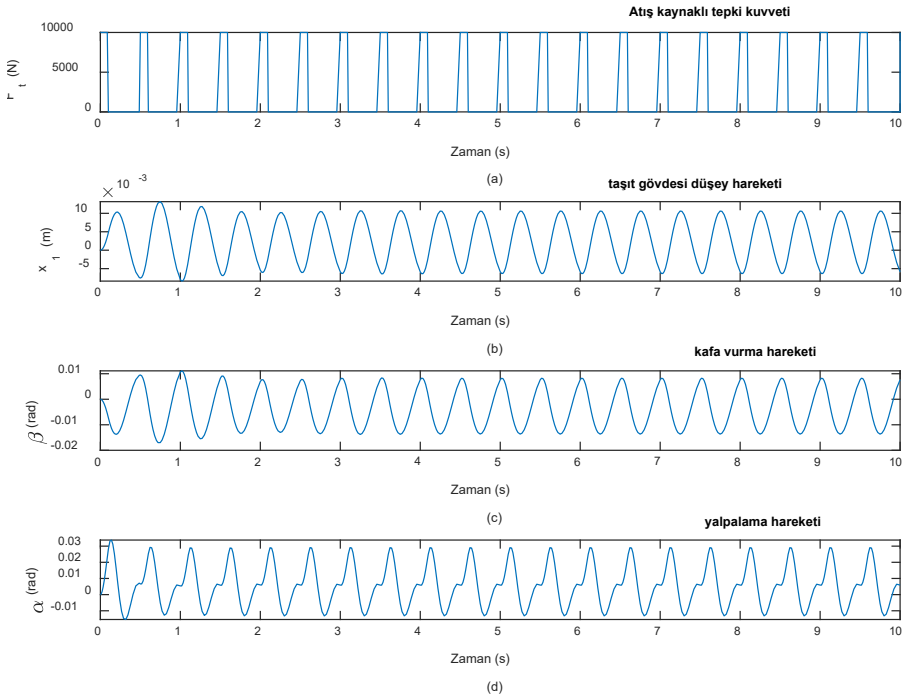

Şekil 8. 34 Numaralı Simülasyon Seti İçin (a) Tepki Kuvveti, (b) Gövde Düşey Hareketi (c) Kafa Vurma Hareketi (d) Yalpalama Hareketi

Şekil 7 ve 8'den atış periyodu T_A'nın oldukça önemli bir parametre olduğu görülmektedir. Atış kalitesinin belirlenmesi için tam atışın yapıldığı andaki gövde konumu (x_1, β ve α) belirleyici olmaktadır. Namlunun ilgili pozisyonu referans alınarak atış hatası Denklem 17'de verilen bağıntı ile belirlenebilir. Burada, silah sisteminin etkili atış menzilinin (L_A) 500 metre olduğu göz önüne alınmıştır. Bu bağıntı, atış hatasını namlu ucunun 500 metre karşısında, namlu eksenine dik bir x'y' düzlemine (nişan ekranına) göre hesaplar.

$$E_A = x_1 + L_A \tan(\beta)\cos(\tau) + L_A \tan(\alpha)\sin(\tau) \tag{17}$$

Dikkat edilirse x_1 teriminin hata üzerindeki etkisi milimetre seviyesini geçmemektedir. Bu tip askeri araçlardan milimetre seviyesinde nişan performansı beklenmediğinden söz konusu terim ihmal edilebilirdir.

Şekil 9'da 22 numaralı simülasyon seti için atış hataları atış numarasına göre verilmektedir. Buna göre 10 saniyede 10 adet atış yapılmıştır. En büyük hata 2. atışta -2,4 m olarak kaydedilmiştir. Sonrasında sistem -1,55 m'lik hata ile sürekli rejime girmiştir.

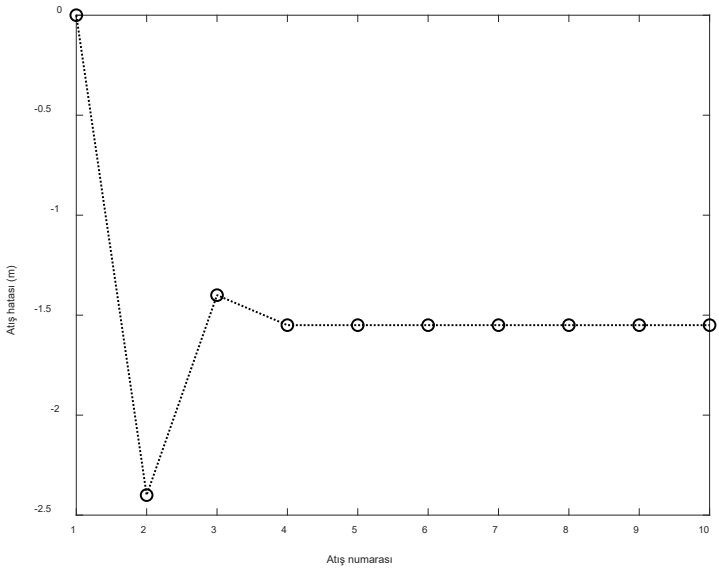

Şekil 9. 22 Numaralı Simülasyon Seti İçin Atış Hatası Grafiği

34 numaralı simülasyonda kaydedilen atış hatası grafiği Şekil 10'da verilmektedir. Bu simülasyon setinde saniyede 2 defa atış yapılmıştır. Buna göre simülasyon süresince toplam 20 adet atış yapılmıştır. En büyük hata değeri 3. atıştaki -5,55 m'dir. Sonrasında sistem -3,80 m'lik hata ile sürekli rejime girmiştir.

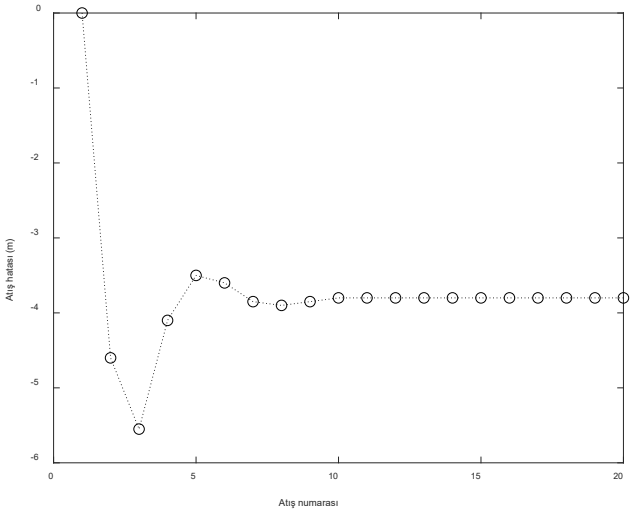

Şekil 10. 34 Numaralı Simülasyon Seti İçin Atış Hatası Grafiği

4. Sonuçlar

Bu çalışmada, üzerinde seri atış yapabilen ağır silah bulunan mobil bir platformun süspansiyon sisteminin atış kalitesine etkisi incelenmiştir ve atış dinamiği elde edilmiştir. Bu amaç için askeri taşıtın gövde titreşimleri dokuz serbestlik dereceli tam taşıt modeli üzerinden ortaya konulmuştur. Atış kalitesi süspansiyon sistemine bağlı olarak tamamen ortaya konabilir olduğu gösterilmiştir. Ayrıca ve daha önemlisi, birim zamandaki atış sayısı parametresine karşılık süspansiyon sistemi modeli üzerinden hatanın öngörülebilir olduğu ortaya konulmuştur. Bunun için nişan alma asistan sistemleri geliştirilebilir. Hali hazırdaki platformdan tam isabet kaydedebilmek için en fazla 4 saniyede bir atış yapılması gerektiği makaleden çıkan başka bir başka sonuçtur. İleriki çalışmalarda hareketli hedefleri nişanlayan sistemler çalışılabilir.

Teşekkür

Bu çalışma Hitit Defence Endüstri A.Ş. desteğiyle yapılmıştır. Verdikleri destek sebebiyle ilgili Kuruluşa teşekkür ederiz.

Kaynakça

Demir C., (2003). Altı Tahrikli (6x6) Askeri Bir Aracın Silah Atış Pozisyonlarında ve Arazide Seyir Halinde Dinamik Durumunun İncelenmesi", YTÜ, Doktora Tezi, İstanbul.

Nguyen D. N. ve Nguyen T. A. (2023). The Dynamic Model and Control Algorithm for the Active Suspension System, *Mathematical Problems in Engineering,* 2023, Article ID 2889435, pp 1-9. https://doi.org/10.1155/2023/2889435

Onat C., Kucukdemiral I. B., Sivrioglu S., ve Yuksek I. (2007). LPV Model Based Gain-Scheduling Controller for a Full Vehicle Active Suspension System, *JVC/Journal of Vibration and Control,* 13(11), pp. 1629–1666. https://doi.org/10.1177/1077546307078784

Onat C., Kucukdemiral I. B., Sivrioglu S., Yuksek I., ve Cansever G. (2009). LPV gain-scheduling controller design for a nonlinear quarter-vehicle active suspension system, *Transactions of the Institute of Measurement and Control,* 31(1), pp. 71–95. https://doi.org/10.1177/0142331208090630

Ozbek C., Ozguney O. C., Burkan R. ve Yagiz N. (2020). Design of a fuzzy robust-adaptive control law for active suspension systems, *Sadhana - Academy Proceedings in Engineering Sciences,* 45:194, pp. 1-16. https://doi.org/10.1007/s12046-020-01433-y

Ping, X.B., Wang, P. ve Zhang J.F. (2018). A Multi-step Output Feedback Robust

MPC Approach for LPV Systems with Bounded Parameter Changes and Disturbance. *Int. J. Control Autom. Syst.,* 16, pp. 2157–2168. https://doi.org/10.1007/s12555-017-0630-0

Yagiz N., (2004). Comparison and Evaluation of Different Control Strategies on A Full Vehicle Model with Passenger Seat Using Sliding Modes. *International Journal of Vehicle Design,* 34(2), pp. 168-182. https://doi.org/10.1504/IJVD.2004.003900

ARAŞTIRMA MAKALELERİ
Research Articles

ISSN 1300-3402
E-ISSN 2667-7520